

A Study on Phase Change Materials at Low Thermal Mass with
Micro-Electro-Mechanical Resonators

by

Syed Asad Manzoor Bukhari

A thesis submitted in partial fulfillment of the requirements for the degree of

Doctor of Philosophy

in

Chemical Engineering

Department of Chemical and Materials Engineering

University of Alberta

© Syed Asad Manzoor Bukhari, 2019

Abstract

Micro-electromechanical systems or MEMS is a modern technology used to create tiny, integrated devices or systems that combine mechanical and electrical components. These miniaturized devices have the ability to sense, control and actuate on the micro and nano scales, and generate observable effects on the macro scale. In modern times, one of the key aspects is to improve the geometry and incorporate functional materials to increase device performance. These devices typically require a high vacuum in order to operate with large amplitudes and sensitivity because of the damping provided by the fluid. To overcome operational issues in fluids, a suspended micro-channel cantilever resonator is proposed which can incorporate polymeric or liquid samples at the same time operating under vacuum with high quality factor. In order to achieve multi-functional device performance and control, tuning of the mechanical frequency of the resonator is required. Among many materials studied in the past, vanadium dioxide VO_2 is one of the key material which can satisfy these demands to a larger extent because of its phase changing nature. It possesses a reversible metal-insulator transition (MIT) ideally at 68°C where monoclinic (M1 phase-insulator) phase transforms to tetragonal or rutile (R phase-metal). Both of the aforementioned

devices have high sensitivity, selectivity and integrated functionalities for better performance.

Suspended microchannel resonators (SMCR) cantilevers can be used for the thermomechanical analysis of polymers. Such a device was used to detect multiple thermal transitions in picogram amounts of two well-known polymers, semicrystalline poly (L-lactide) (PLA) and amorphous poly (methylmethacrylate) (PMMA). The polymer samples, when loaded inside the cantilever and heated, affect its resonance frequency due to changes in its density and stiffness. Continuous monitoring of the resonance frequency provided information about β -transition (T_β), glass transition (T_g), crystallization (T_c), and melting (T_m) of the confined polymer samples.

Phase change materials can also be integrated with conventional semiconducting MEMS resonators to achieve frequency tuning with various external stimuli. Vanadium dioxide (VO_2) is a class of quantum materials which has a characteristic insulator to metal transition complemented by a four order of magnitude change in resistance and structural change from monoclinic to rutile phase. This transition can also be triggered via optical and electrical input power while keeping the device at room temperature. By exploiting the phase transformation, thermal, optical, electrical and electro-optic excitation were used for bi-directional mechanical frequency tuning. First, thin-film deposition process parameters were optimized in order to achieve a large magnitude change in resistance and lower onset temperature. Thin films of

VO₂ were then deposited on microstrings. Bi-directional frequency tuning was achieved with a single pump and probe optical source. Frequency tuning was also studied by scanning laser at fixed distances from the anchor to the center of the resonator. Electro-thermal excitation of AC and DC signals was used to pump the system and bi-directional frequency tuning was observed. This study has potential applications in thermal, electronic and optical switches, ultra-fast mechanical frequency tuning and gas sensing.

Preface

Chapter 4 of this thesis has been published as "Syed Asad Manzoor Bukhari, M. Faheem Khan, Ankur Goswami*, Ryan McGee, Thomas Thundat*. Thermomechanical analysis of picograms of polymers using a suspended microchannel cantilever, *RSC Adv.*, 2017, 7, 8415-8420". Syed Asad Manzoor Bukhari performed experiments on DSC, Frequency measurements with LDV. Faheem Khan fabricated the devices in Nanofab, Ankur Goswami and Thomas Thundat designed the experimental set up and helped writing the paper, Ryan McGee performed SEM of the resonators, Thomas Thundat and Ankur Goswami edited the papers and were the corresponding authors.

Chapter 5 of the thesis will be submitted for publication as "Syed A. Bukhari, Ankur Goswami*, Rosmi Abraham, Pawan Kumar, Ryan McGee, Hyun-Joong Chung, and Thomas Thundat*. Effect of oxygen flow rate on metal-insulator transition in VO₂ films deposited by pulsed laser deposition". Syed A. Bukhari performed thin films deposition and SEM measurements and wrote the paper. Ankur Goswami provided idea of the work, organized manuscript and help conducting AFM measurements. Rosmi Abraham carried electrical resistance measurements with probe station. Pawan Kumar analyzed XPS data. Ryan McGee helped with thin films deposition process and editing the manuscript. Hyun-Joong Chung co-supervised the project, helped organize data, editing and discussions about results. Thomas Thundat supervised the project.

Chapter 6 of the thesis will be submitted for publication as "Syed A. Bukhari, Ankur Goswami*, Ryan McGee, Liang Zhou, Hyun-Joong Chung, and Thomas Thundat*. Bi-directional resonance frequency modulation of

VO₂ microstrings by photo- induced metal-insulator transition". Syed A. Bukhari wrote the paper and performed thin films deposition with PLD, XRD, AFM, LDV measurements and designed the experimental set up. Ankur Goswami is corresponding author and provided the idea of the project and helped with all experiments. Ryan McGee fabricated the microstrings. Liang Zhou performed electrical resistance measurements. Hyun-Joong Chung co-supervised the project and provided valuable feedback through to the completion in designing experiments, editing and discussions. Thomas Thundat is corresponding author and supervised the project.

Chapter 7, section 7.4.1 is submitted for publication in IEEE-MEMS 2020 conference proceedings as "Syed A. Bukhari, Ankur Goswami*, Liang Zhou, Ryan McGee, Dale Hume, Hyun-Joong Chung and Thomas Thundat *. Bi-directional frequency tuning of Vanadium dioxide microstring resonator by optothermal excitation". Syed. A Bukhari conducted PLD films deposition and characterization with LDV. Ankur Goswami carried out SEM and helped organizing the data. Liang Zhou performed electrical resistivity measurements. Ryan McGee fabricated microstrings, Dale Hume provided technical support for analyzing and interpreting the data, Hyun-Joong Chung was co-supervisor of the project and helped analyzing and organizing data and writing manuscript. Thomas Thundat was the main supervisor of the project. Section 7.4.2 will be submitted as another manuscript with additional data with Raman spectroscopy of VO₂ microstrings. The author's list is not decided yet.

Chapter 8 will be submitted for publication as Ankur Goswami*, Syed A. Bukhari[†], Ryan McGee, Liang Zhou, Faheem Khan, Hyun-Joong Chung, and Thomas Thundat*. "Tuning mechanical frequency of VO₂ coated resonators with electric field". Syed A. Bukhari and Ankur Goswami have equal contribution in the paper. Syed A. Bukhari conducted all the experiments and analyzed the data. Ankur Goswami designed the experimental

platform and provided idea. Ryan McGee fabricated microstrings, Liang Zhou carried out electrical resistivity measurements with temperature and Faheem Khan helped fabricating the vacuum probe station and data acquisition. Hyun-Joong Chung was co-supervisor of the project and provided ideas and instructions to help complete the project. Thomas Thundat was the main supervisor of the project who provided valuable input throughout of the project life cycle.

Acknowledgements

This thesis is a reflection of years of hard work which could not be possible without the support of a team. I thank for the support I received from several people, including family, friends, mentors, and colleagues. I would first like to thank my Father, grandfather and my mother for being supportive during all that hard time not only in academics but since the time I was born. I am also thankful to my sisters, brothers, cousins and uncles who all supported me since I was a child. My PhD work would never be possible without the love, help and care I received from my wife Zakia. She sacrificed a lot during my studies and late stays. She would take care of my daughter Aliza and my Son Irtaza and supported me every possible way to succeed both academically and professionally. Whenever I reached home after being tired and lazy, my family made sure all my tiredness and stress goes away.

My sincerest thanks to my thesis advisor, Dr. Thomas Thundat, who always guided me throughout my degree and trained me to become an independent researcher. My discussions with him always encouraged me to push my boundaries and strive for more and think out of the box. His passion about science and creativity boosted my confidence many fold. He was so helpful and caring during all the stressful times and his cooperation was just amazing. I extend my thanks to my co-advisor, Dr. Hyun Joong Chung who supported me during the last period of my PhD. His caring nature and willingness to help gave me a lot of positive energy during the course of my degree. I would also thank to the team of researchers in Dr. Chung's lab who were always available to support.

I would like to mention one name here who worked day and night with

me by taking me in under his direct supervision, Dr. Ankur Gowami. A smart researcher, extremely hard working individual and available to help all the times and last but not least a caring and loving personality. He would guide me to summarize my whole PhD in a short time as he was equally involved in the project. There is no way I can pay back to his great help to me. Another group member and senior advisor was Dr. Faheem Khan, who would always be there to help you with any technical and scientific difficulty. He trained me on many instruments, software and he is always a motivational personality. A special thanks to Dr. Ryan McGee, a jolly person, wonderful researcher and very caring human being. He made sure that he teaches me everything he knows and what is important for me. I will always be grateful to him.

I would also like to extend my thanks to Lab members Rosmi Abraham, Dr. Priyesh Dhandharia, Dr. Naresh Miriyala, Dr. John Hawk, Dr. Jun Liu, Dr. Tinu Abraham and Dr. Karen Jiang who were always up for stimulating discussion and providing their expertise to the research at hand. Calvin Schofield, and Liang (John) Zhou, were two amazing undergraduate researchers who helped and supported me far exceeding my expectations. Shammy Raj, Sarang Gumfekar and Josh Cunningham, it was great to sit with you and had chat during our coffee breaks.

The staff in the nanofab at the University of Alberta provided countless hours of assistance and training, making my fabrication and characterization needs much easier. Such a state-of-the-art facility is an enormous advantage to have, and their push for continuous expansion in obtaining the state of the art equipment made life much easier. I would like to acknowledge Josie Nebo who has to put up with the collective needs of our entire group. Without her, our lab would not be where it is today. To everyone, words cannot express how truly appreciative I am of all the support I have received.

Contents

1	Introduction and literature review	1
1.1	Introduction and Motivation	1
1.2	Literature & background	5
1.3	Technological significance of current study	8
1.3.1	Probing phase transitions in polymeric liquids	8
1.3.2	Probing phase transitions in phase change solids	9
1.4	Thesis objective and organization	10
2	Theoretical background	18
2.1	Introduction	18
2.2	Dynamics of suspended micro-channel Cantilever	19
2.3	Dynamics of micro-string resonator	24
2.3.1	Current driven insulator to metal transition	24
2.3.2	Photo-Induced insulator to metal transition	32
2.3.3	Light-resonator interaction and heat transport	34
2.3.4	Effect of materials properties on string dynamics	35
3	Fabrication and characterization	37
3.1	Microfabrication and process flow	37
3.1.1	Fabrication process for micro-channel cantilevers	38
3.1.2	Fabrication process for microstring resonators	38
3.2	Laser Doppler Vibrometer (LDV)	41

3.2.1	Fundamentals and working mechanism	43
3.2.2	Integrated instrumentation with LDV	44
3.3	Pulsed laser deposition (PLD)	46
3.3.1	Deposition mechanism on substrate	50
3.4	X-ray diffraction	52
3.5	Probe station	54
3.6	Helium ion microscopy	55
3.7	Atomic force microscopy	55
3.8	Differential scanning calorimeter (DSC)	57
3.9	X-ray photoelectron spectroscopy (XPS)	57
4	Probing phase transitions in polymeric liquids with MEMS	59
4.1	Abstract	59
4.2	Introduction	60
4.3	Experimental	62
4.4	Results and discussion	64
4.5	Conclusion	71
5	Thin films deposition of phase change material	72
5.1	Abstract	72
5.2	Introduction	73
5.3	Experimental	75
5.3.1	Thin films deposition	75
5.3.2	Characterization	76
5.4	Results and discussion	79
5.4.1	Phase identification with X-ray analysis	79
5.4.2	Insulator to metal transition	81
5.4.3	Tapping mode AFM studies	82
5.4.4	Kelvin probe force microscopy for surface potential	83
5.4.5	Scanning helium ion microscope	85

5.4.6	XPS analysis	88
5.5	Conclusion	90
5.6	Acknowledgements	91
5.7	Supplementary data	92
5.7.1	Additional AFM Images	92
6	Photo induced insulator to metal transition in VO₂ microstrings and resonance frequency modulation	94
6.1	Abstract	94
6.2	Introduction	95
6.3	Experimental methods	99
6.4	Results and discussion	100
6.4.1	Frequency modulation with single pump and probe . .	100
6.4.2	Frequency modulation with external source	107
6.5	Conclusion	115
6.6	Acknowledgements	116
6.7	Supplementary data	116
7	Spatial frequency tuning of VO₂ resonators with opto-thermal excitation	120
7.1	Abstract	120
7.2	Introduction	121
7.3	Experimental process	123
7.4	Analysis of experimental data	126
7.4.1	Optically induced frequency modulation	126
7.4.2	Electro-optic frequency modulation	131
7.5	Resonance frequency shift caused by optical and electrical heating	133
7.6	Conclusion	134
7.7	Supplementary information	135

8	Electro-mechanical frequency tuning of VO₂ coated resonators	139
8.1	Abstract	139
8.2	Introduction	140
8.3	Experimental	143
8.3.1	Fabrication and deposition	143
8.3.2	EMIT measurements with LDV	144
8.4	Results and discussion	146
8.4.1	Frequency tuning with DC field	147
8.4.2	Frequency tuning with AC field	150
8.5	Conclusions	155
8.6	Acknowledgments	157
8.7	Supplementary data	157
9	Conclusions	160
9.1	Summary of completed work	160
9.2	Recommendation for future work	163

List of Tables

1.1	Brief summary of each chapter. This table summarizes the topics of each chapter followed by detailed findings. The objective of each chapter from 4-8 is described first. Major findings are the outcomes of the research done on that topic. Each chapter is a an independent project.	16
5.1	Deposition conditions for deposited films on <i>Si/SiO₂</i> substrate. The gas pressure (50 mTorr), target-substrate distance (31 mm), deposition temperature (600 °C) and laser fluence (2.6 J/cm ²) were consistent for all experiments.	78
5.2	Surface roughness of VO ₂ films deposited on Si. Average surface roughness values were calculated using the image of interest with Bruker's Nanoscope analysis software. The peak value of the distribution of surface roughness was selected as average roughness of the sample.	83
5.3	XPS elemental analysis of VO ₂ thin film showing the change in chemical composition of materials as function of flow rate. CasaXPS analysis software was used to determine the presence of Vanadium and oxygen in the films.	89

6.1 Optical power and density calculations. The power values were experimentally measured while the density is approximately calculated using dimensions of the resonator at the point of exposure. The values were measured by placing a Thorlabs PM 100 photo detector at the same distance from the LDV where microstring was placed. The glass cover of experimental vacuum chamber was also placed in between the LDV and the photo-detector. The power measured includes the background room light as well. 107

List of Figures

- 1.1 Two types of micro-electro-mechanical resonators (MEMS resonators) employed to characterize materials at micro scale in this dissertation. Suspended micro-channel resonator (SMCR) shown in (a) will be used to characterize two well known polymers by melt flowing the polymers in micro-channel. Cartoon shows the micro-channel opened at the tip of the cantilever. Frequency and amplitude data (d) was collected with Laser Doppler Vibrometer (LDV) model MSA 500 and thermo-mechanical response of the strings (frequency vs. temperature) would be correlated with stiffness change of the cantilever as a function of temperature (e). 15

- 2.1 Side view of a cantilever with a microfluid channel on top of it. Resonator was oscillated at its first resonance mode with a piezo actuator. Temperature was controlled via feedback circuit using a DC supply to the thermoelectric peltier element. Data aquisition was done with Laser Doppler vibrometer by measuring the FFT spectrum of resonance frequency of the device. 20

2.2	Mathematical model for suspended micro-channel resonator. Cantilever without the polymer has a stiffness k_c while k_p is the stiffness of the polymer. Total mass after loading will represent the mass of the system.	23
2.3	Schematic of mechanical detection of electric field assisted insulator to metal transition in O_2 coated micro-string resonator.	25
2.4	Surface stress on the micro-string generated by insulator to metal transition in VO_2 layer coated on Pt/SiN.	28
2.5	Schematic of mechanical detection of photo induced insulator to metal transition in O_2 coated micro-string resonator. Pump and probe using the same built in source in LDV (635 nm laser) is shown in part (a). In part (b), we set the internal power of LDV to minimum while using an external source to pump the system with three different wavelengths i.e. 635 nm, 520 nm and 450 nm respectively.	33
3.1	Process flow of microfabrication of suspended micro-channel resonators. A six step process started from $500 \mu m$ thick silicon wafer with intermediate patterning, etching and a released device shown in step (f).	39
3.2	Process flow of microfabrication of micro-string resonators for studying phase change material characteristics. The process starts with $1.5 \mu m$ thick thermal oxide wafer with various intermediate patterning and etching steps until we got release micro-string resonators for further thin films deposition to be done with Pulsed laser technique.	40

3.3 A reference beam of laser with frequency f_l interferes with a Bragg modulated beam $f_l + f_b + f_o$ on a position sensitive detector (PSD). The motion of the target object adds a Doppler shift to the beam which then combines with the reference beam to produce interference pattern on the photo detector. The output is a frequency modulated signal which then can be demodulated to extract the velocity vs. time of the vibrating object. 42

3.4 Platforms developed for carrying thermal, electrical and optical excitation and measurements in resonating systems used for probing phase transitions in liquids and solids. Ferroelectric heating stage used a peltier element attached with a big chunk of copper with thermal paste with temperature sensor Pt 1000 fixed on top of it. A piezo actuator is used to drive the resonator and whole system was put inside the vacuum chamber for detecting mechanical vibrations of both strings and cantilevers. In (b) and external optical excitation was used in conjunction with the internal LDV laser which itself can have a variable power. In (c), two contacts vacuum probe station was developed to probe electric field assisted insulator to metal transition in VO₂ strings. Function generator shown in (d), DC source shown in (e) and Micro-volt meter shown in (f) were used to provide ac signal, DC supply to peltier element and measure the resistance of Pt 1000 sensor respectively. . . . 45

3.5 Graphical representation of the PLD deposition system. The laser enters the vacuum chamber through a glass window and hits the rotating target. The plasma plume is ejected normal to the surface of the target and is directed towards the heated substrate stage. 48

3.6	There are three different interfacial energies involved in the PLD film deposition process. Depending on relative magnitude of free energy at each interface, a VW or FM growth mechanism will occur.	51
3.7	Schematic representation of Bragg diffraction. Constructive interference occurs if the path length difference between the incoming waves is equal to an integer multiple of their wavelength.	53
4.1	Figure1. (a) Experimental setup to characterize picograms of polymers. (b) SEM of the top view of the microchannel cantilever. Yellow dash line in shows from where the cantilever was cut to show Fig.(c). (c) Shows SEM of the cross-section of half-filled cantilever which depicts the unfilled and filled channel.	63
4.2	Figure2. (a) Resonance frequency and phase of empty vs PL filled cantilver.(b) resonance frequency and phase of empty and PMMA filled cantilever.	66
4.3	Figure3. (a)Temperature stability as a frequency measurement response for empty and polymer filled cantilevers.(b) Thermal characterization of empty and polymer filled cantilever.	68
4.4	Figure4. Comparison of heat flow from DSC with the stiffness changes of PLA and PMMA as a function of temperature.	70
5.1	Schematic of PLD experimental setup, including the laser path and the PLD chamber.	77

5.2	(a) XRD pattern of VO ₂ films deposited on Si substrate. FWHM of (011) monoclinic peak was found to increase with increasing flow rate up to 30 SCCM and decreased again for 50 and 90 SCCM suggesting a variation in crystallite size with changing flow rates of oxygen.	80
5.3	Resistance as a function of temperature for VO ₂ thin films grown on silicon substrates. No transition present in case of lower flow rates of oxygen. High onset temperature with sharp and large transition was seen for flow rates of 5, 50 and 90 SCCM. Least hysteresis with lowest transition temperature was observed for flow rates of 10 and 30 SCCM.	81
5.4	Roughness of thin films deposited under different oxygen flow rates. Variation of average surface roughness is plotted as a function of flow rate. The measured thickness of the film was 15-20 nm which was measured in our previous work [1]	82
5.5	Spatial scans of 500 nm × 500 nm for contact potential difference measurements with contact mode KPFM. Each scan is labeled with corresponding oxygen flow rate at which the film was deposited	84
5.6	Variations of local work function of VO ₂ films deposited on Si with and without the laser. The minimum of the work function appears for flow rates between 10 and 30 SCCM suggesting that an appropriate flow rate can effect the electronic properties of the films.	86

5.7	Scanning helium ion micrographs (S-HIM) of all seven samples deposited with PLD at constant pressure. Samples are labeled with oxygen flow rate. It is quite clear that polycrystalline VO ₂ was formed for all flow rates but the relative grain size changed for higher flow rates. S-HIM was used to probe the surface because it offers imaging on insulating surfaces without metallic coating.	87
5.8	(a) XPS survey scan of VO ₂ thin film treated at different flow rate, (b) Core-level HR-XPS spectra of VO ₂ samples in V2 _p region demonstrating various oxidation states and relative contribution, (c) HR-XPS spectra of VO ₂ samples in O1 _s region.	88
5.9	Kelvin probe force microscopy images for different flow rates with 635 nm laser ON while conducting scans.	92
5.10	Surface potential distributions for different flow rates. Both with and without 635 nm laser.	93

6.1 Schematic layout of non-contact laser based MIT measurement of VO₂ microstrings using LDV. The string has 15-20 nm VO₂ layer deposited on Pt and with 250 nm SiN as a base layer. The microstructure of VO₂ layer was taken with S-HIM at 500 nm resolution and imported into MS-Visio. Frequency and amplitude response of the VO₂ microstrings was recorded through Laser Doppler Vibrometer by exciting the string at its first resonance mode with forced actuation via a piezo. Scanning helium micrographs were taken at a resolution of 2 μm and at a working distance of 9 mm without any gold coating. The zoomed portion of the string was taken at 500 nm resolution and polycrystalline VO₂ structure can be seen. A structural transition with incident optical power above 38 μW will change the material from semiconducting monoclinic to metallic rutile phase [2]. It is assumed the focused laser beam can excite the IMT mechanism at a localized spot and that will change the dynamics of the microstrings. That is the reason for showing the rutile phase existing only where the laser is focused.101

6.2 (a) FFT spectrum of VO₂ coated Pt strings on SiN in comparison with Pt/SiN strings. The decrease in resonance frequency corresponds to the added mass on the string. (b) VO₂ deposited string was heated to 80 °C and FFT spectrum was recorded. There is an increase in frequency by 13 kHz which is likely because of the top layer transitioned to metallic phase accompanied by a change in crystal structure leading to in plane tensile stress which would increase the stiffness and overall increase in frequency. (c) Shows comparison of electrical resistance and resonance frequency change of the string as a function of temperature. There is more than 3 orders of magnitude change in electrical resistance near 55 °C and $\Delta f/f \sim 6\%$ change in resonance frequency of the string. The resonance frequency changed in three different regions i.e. at temperatures slightly above room temperature, around the IMT transition and above IMT can be correlated with softening of the string at low thermal powers, triggering of IMT and causing a huge stress on top layer and hence increase in frequency and decrease in frequency upon further heating beyond 60 °C. The latter is most likely softening of the rutile phase after all VO₂ crystallites were transformed to rutile phase and further heating would only soften the material as expected. Frequency and amplitude variations as a function of optical power. (d) Here LDV laser was used for pumping and probing the system. A slight decrease in frequency and amplitude at very low optical excitation with a sharp increase near 50 μW and a further decrease above 75 μW can be correlated with decreased Young's modulus with heating, triggering of insulator to metal transition and further decrease in modulus of the rutile crystal phase of VO₂ respectively. 103

- 6.3 (a) FFT spectrum of resonance frequency of VO₂ coated microstrings for lowest pump and probe laser power P_0 , P_1 and P_2 levels. (b) FFT spectrum for powers $P_3 - P_5$ showed a huge increase in frequency with relatively small increase in amplitude suggesting that localized heating of VO₂ layer can trigger the crystal structure change from monoclinic to rutile phase which is likely cause additional stress leading to increased frequency of the string. (c) FFT spectrum for higher optical powers. Stability of resonator at a particular power was observed for 180 seconds for both frequency (d) and amplitude (e) drift as a function of time and at all optical power levels. (f) Shows a comparison between frequency and amplitude variation of uncoated and VO₂ coated strings as a function of laser power. 108
- 6.4 (a) Effect of pressure on magnitude of frequency/amplitude variations as a function of incident optical power. All pressures were measured for air flow into the vacuum chamber with a needle valve and standby ON mode of turbo pump at 300 rpm speed. The magnitude of increase in frequency and amplitude decreases with increasing air pressure. The decrease in frequency might be due to more heat been taken away by the gas molecules while decrease in amplitude could be because of additional damping introduced in the system. (b) and (c) represent the zoomed portions of (a) to visualize the optical power range up to 52 μ W. 109

- 6.5 (a) Frequency response of VO₂ string with external optical power of 635 nm laser keeping the LDV laser at minimum P_0 . External power was regulated with an electronic controller. Total optical power includes the ambient and the minimum power of LDV laser which is 22 μW . Response within 32-67 μW is zoomed in part (c) while response for optical power of 97 μW is shown in (b). (d) Shows vertically offset frequency response by keeping the external power constant at 97 μW and increasing the LDV power from $P_0 - P_7$ 111
- 6.6 Frequency response with 520 nm external laser. (a) Response for a 97 μW power. Here we saw decrease in frequency as the power was turned ON. Upon switching internal power to level P_1 , a large increase in frequency was observed with high frequency state representing the ON and lower state representing the OFF status of laser (b). However we could only see observable change in frequency up to internal power level P_3 as the difference between ON and OFF state is practically the same for level $P_3 - P_7$ 112
- 6.7 Frequency response for 450 nm (blue) external laser. We saw same trend for all internal LDV power values from $P_1 - P_7$ while keeping the external power to a maximum value of 97 μW (a). When the system was subjected to the constant maximum external power and internal power level P_0 for longer times (b), a transition from decreasing frequency with power happened and system responded opposite way above that transition (c). The system response reversed instantly around 390 seconds and an increase in frequency with laser being in ON state was observed (d). 113

6.8	Process flow for fabrication of VO ₂ coated microstring resonators. Mechanical response of released devices was recorded using LDV before and after depositing VO ₂	117
6.9	Optical response of a doubly clamped string coated with VO ₂ /TiO ₂ shown in (a) and only TiO ₂ coated on Pt.	118
6.10	Using the external light as a pump while probing the mechanical response with LDV laser.	119
7.1	(a) Microstring resonator with frequency being measured as a function of spatially distributed scanning points along the lateral direction (b) Polytec MSA 500 vibration measurements, (c) optical image of doubly clamped strings with electrical contact probes (d) Scanning-HIM image of VO ₂ coated resonator close to its one anchor point, (e) high resolution image taken at the center of the resonator showing VO ₂ crystallite with cartoon showing red label for tetragonal (rutile) phase and blue region corresponding to insulating monoclinic phase of VO ₂ film deposited on the string.	125
7.2	(a) XRD analysis polycrystalline VO ₂ deposited on Pt/Si/SiN strings with optimized oxygen flow rate of 5 SCCM and chamber pressure of 100 mTorr (b) Tapping mode AFM image of 250 nm × 500 nm area showing island type formation of VO ₂ and a smooth film of average surface roughness of 0.7 nm.	126
7.3	(a) FFT spectrum of uncoated microstring resonator in first mode, VO ₂ coated resonator in first mode at room temperature and at 66 °C. (b) Temperature dependence of frequency variations during thermal cycling of resonator from room temperature to 92 °C with control heating/cooling.	127

7.4	(a) Frequency variation of VO ₂ coated resonator when at different spatial positions along the string as a function of incident laser power ($P_0 - P_3$). Two extreme points are close to the anchors of the beam. (b) Amplitude of vibration measured at fifteen equidistant points along the string ($P_0 - P_3$). (c) Frequency variation at fifteen equidistant points along the strings for laser power levels $P_4 - P_7$ and (d) amplitude variation for same power levels.	130
7.5	(a) Schematic of VO ₂ coated resonator with 15 equidistant points along the lateral direction and electrical contacts. (b) Variation of mechanical resonance frequency at different locations as a function of ac signal of 200 mV applied across it. (c) Frequency response of resonator for 300 mV signal, (d) frequency response for a 400 mV signal.	132
7.6	Process flow for microfabrication of doubly clamped beam resonators. Thermal oxide wafers were coated with 250 nm SiN using LPCVD and 80 nm Pt in step (a). Patterning a lift off, etch, steps were done until the device was released. VO ₂ films were deposited on released devices using an optimized deposition condition	136
7.7	3D plot of frequency and amplitude variation of the resonator at fifteen different locations in the suspended part in between the anchor points at different power levels.	137
7.8	3D plot of dynamic response of the resonators for higher optical powers.	138

8.1	(a) SEM image of 200 μm long VO ₂ /TiO ₂ coated string resonator with contact pads. (b) Microstring contact pads with probes. (c) schematic of electrical current applied to the string with Pt-1000 sensor for temperature measurements and piezo for applying acoustic vibrations to oscillate the resonator at its fundamental mode. (d) Scanning helium ion images of resonator without using any gold coating. Large VO ₂ grains are visible at 200 nm resolution (e).	145
8.2	(a) FFT of first mode resonance frequency of uncoated and coated VO ₂ strings. (b) Normalized resistance change of the film as function of temperature and (c) tapping mode AFM scan for 500 nm \times 250 nm area with calculated average surface roughness of 0.69 nm.	147
8.3	(a) Mechanical frequency of resonator when the resonator was subjected to an ON/OFF cycle of an electric field of 63 kV/cm and 100 kV/cm (b). Frequency and amplitude variation for electric fields from 125-175 kV/cm in (c) and (d) respectively. .	149
8.4	(a) Mechanical frequency response for a voltage ramp of 0-0.7 V for both heating and cooling cycles with electro-thermal energy. (b) Voltage ramp of 0-1 V leading to confirm the upper critical field for EMIT transition with slightly different behavior during the cooling and heating cycles. (c) confirmation of upper critical field with ON/OFF cycles of 0.8, 0.9 and 1 V. . .	151
8.5	(a) Dynamic response of 200 μm long resonator as a function of ac electric field with input voltage of 150 mV. (b) mechanical response for an ac signal of peak voltage of 200 mV, 260 mV (c) and 270 mV (d).	153
8.6	Mechanical frequency response vs ac field applied for input amplitude of 290 mV (a), 320 mV (b), 330 mV (c) and 400 mV (d).154	

8.7	(a) Mechanical frequency variation as a function of step function of peak amplitudes of ± 400 mV. (b) Zoomed in selected portion of (a) to visualize the frequency changes after the first voltage step.	156
8.8	(a) Mechanical frequency variation as a function of step function of peak amplitudes of ± 400 mV at 500μ Hz, (b) 1 mHz, (c) 10 mHz and (d) 20 mHz.	158
8.9	(a) Mechanical frequency variation as a function of step function of peak amplitudes of ± 400 mV at 100 mHz, (b) 1 Hz, (c) 100 Hz and (d) 1 kHz.	159

List of Abbreviations

AFM	Atomic force microscopy
BOE	Buffered oxide etch
CVD	Chemical vapour deposition
DSC	Differential scanning calorimeter
DOE	Design of experiments
EDX	Energy dispersive X-ray spectroscopy
FFT	Fast Fourier transform
GLAD	Glancing angle deposition
<i>hcp</i>	Hexagonal close packed
S-HIM	Scanning Helium ion microscopy
IR	Infrared
KPFM	Kalvin probe force microscopy
LDV	Laser Doppler Vibrometry
LPCVD	Low pressured chemical vapour deposition
MBE	Molecular beam epitaxy
MEMS	Micro-Electro-Mechanical Systems
MIT	Metal-insulator Transition
MOEMS	Micro-Opto-Electro-Mechanical Systems
PECVD	Plasma enhanced chemical vapour deposition
PLA	Poly-L-Lactide
PL	Photoluminescence
PLD	Pulsed laser deposition
PVD	Physical vapour deposition
PMMA	Poly (methyl methacrylate)
QCL	Quantum cascade laser
RF	Radio frequency
RIE	Reactive ion etching

SEM	Scanning electron microscopy
SMCR	Suspended micro-channel resonator
TCR	Temperature coefficient of resistance
TEM	Transmission electron microscopy
UPS	Ultraviolet photoelectron spectroscopy
UV	Ultraviolet
VHF	Vapour hydrofluoric acid
XPS	X-ray photoelectron spectroscopy
XRD	X-ray diffraction

List of Symbols

α	angle between b and c axes
α	Optical absorption coefficient
α	glass transition
β	angle between a and c axes
β	beta transition
γ	angle between a and b axes
γ	Interfacial free energy
θ	diffraction angle
λ	Wavelength
ρ	density
τ	Laser pulse width
ϕ	XRD sample stage angle
ϕ	Plasma altitude angle
ψ	XRD detector angle
A	Atomic mass
A	resonator cross sectional area
a_f, a_s	Film, substrate lattice constants
d, d_0	final and initial grain size
d	Interplanar spacing
E	Young's modulus
E	Laser energy
E_0	Accelerating voltage
f_i	Resonance frequency
f_m	Lattice misfit parameter
h	Film thickness
h, k, l	Miller indices
I	Area moment of inertia

\mathbf{k}, \mathbf{k}'	Initial and final wavevector
k_b	Boltzmann constant
l	Resonator length
l_a	Laser spot size
M	Grain boundary mobility
$\hat{\mathbf{n}}, \hat{\mathbf{n}}'$	Initial and final x-ray direction
P_0	Background gas pressure
Q	Activation energy
\mathbf{R}	Bravais lattice vector
R	Plasma range
R_{KO}	Electron penetration depth
r, r^*	Grain and critical grain size
S	Tensile force
T_c	Critical temperature
t	Resonator thickness
V_i	Initial volume of the ablated species
Z	Atomic number

Chapter 1

Introduction and literature review

1.1 Introduction and Motivation

Nanotechnology is a rapidly growing field because of its potential applications in many sectors of global economy, namely healthcare, cosmetics, energy, and agriculture. The technology is revolutionizing every industry, while tremendously attracting worldwide attention. Owing to its wide range of uses, the global nanotechnology market is expected to grow around 17-21% during the forecast period of 2018-2024 [3]. There has been never more demand for small, fast and reliable products in the society which will push the field of nanotechnology to grow rapidly. The projected investment in this area is reaching over USD 3 Trillion [4] in coming years. This spending on nanotechnology products will significantly increase the funding to research and product development agencies. There are multiple processes involved in development of the products. Those are nanoparticles synthesis, smart fabrication and designs, lithographic techniques, and coatings.

Designing a device having multi-functionality, robustness, repeat-ability, and reliability has been a challenge so far. Among many devices, micro-resonators e.g. singly and doubly clamped beams are the mechanically vibrating structures with largest amplitude of vibration at resonance frequency.

Clamped beams have been used for attogram level mass sensing [5] in vacuum where the mechanism of sensing was change in frequency of resonator with adhesion of a mass on the surface of the resonating device. These resonators however damped heavily when immersed into a liquid environment because of viscous force. Scott Manalis group in MIT came up with an idea in 2003 where they developed a cantilever with a microchannel embedded into it [6]. They were able to characterize different liquids without compromising the quality factor of the resonator as the liquid was inside the channel and resonator itself could vibrate in vacuum. Using this sensor, they detected a molecule in a subnanoliter fluid volume using shifts in resonance frequency of a suspended microfluidic channel upon accumulation of molecules on the inside walls of the device. This work motivated researchers to dig more into this technology specifically for bio sensing and polymer characterization. We designed, fabricated and tested a microfluidic device with microchannel fabricated on top of a beam cantilever for characterizing the liquids which have phase transitions. The polymer samples, when loaded inside the cantilever, affect its resonance frequency due to changes in its total mass and stiffness. When taken through a thermal cycle, the resonance response of the cantilever further changes due to multiple thermal transitions of the samples. Continuous monitoring of the resonance frequency provides information about phase transitions in the polymers. Because of sensitivity of the device, we were able to pick up some of the transitions which were not observed with conventional differential scanning calorimetry.

Certain materials can change their phase above a critical temperature. We will consider VO₂ as one prototype material to see how the change in its phase with temperature, incident light and electric field helps tuning the resonance frequency of doubly clamped beams. A doubly clamped beam is mechanically more stable, which in particular results in a higher fabrication yield compared to cantilevers, and intrinsic energy loss mechanisms are

very small [7] leading to a quality factor over a million in vacuum. VO₂ is a correlated transition metal oxide (TMO) that has an insulator-metal phase transition (IMT) [8]. This phase transition can either be triggered by thermal heating beyond $T_c \geq 340$ K at normal pressure or with electric field $E \geq 105$ Vcm⁻¹ [9]. It has also been proven that the transition can be excited optically [10] and using terahertz pulses [11]. The phase transition is reversible with a hysteresis and material can be restored to its insulating phase upon removal of external stimuli.

Depositing high quality vanadium dioxide thin films is a challenge by itself as this material exhibits strong correlation effects which further depend on the oxidation state of Vanadium. Both thin films and bulk phase formation of different oxides i.e. VO, V₂O₃, VO₂, and V₂O₅ can form because of existence of half d shell electrons of Vanadium [12]. Among these oxides, VO₂ exhibits ultra-fast insulator to metal transition from monoclinic (VO₂-M) to rutile (VO₂-R) phase with 3-5 order of magnitude change in electrical resistance and strong transmission change near the infrared spectrum of light [13]. These two characteristics make this material a useful candidate for electronic switches [14], ultrathin coating for smart window applications [15], uncloaked microbolometers [16] and memory devices [17]- [18].

Micro-string resonators are very sensitive platform for detection as very small external excitation can change the resonance frequency to a large extent. VO₂ becomes very interesting material to be integrated with micro-string resonators because its transition can be triggered optically, electrically and thermally and that too in the range of femto-seconds [11]. This ultrafast change in properties can offer frequency modulation in THz regime [19]. In our first research project on VO₂, we reported a blue shift in mechanical frequency of a micro-string resonator coated with 20 nm of polycrystalline VO₂ (when $< 1 \mu\text{m}^2$ area of the resonator was illuminated with a 635 nm laser. In the first part of the study, built in laser in Laser Doppler Vibrometer

(LDV) was used) to excite IMT within the exposed area and detected the mechanical response of the string with the same light as part of it reflects back and adds a Doppler shift in the measurement beam which then would interfere with the reference beam creating a pattern on the position sensitive photo detector (PSD). IMT not only changes the crystal structure of the top layer but also reduces the refractive index considerably. This change in refractive index allows us to even tune the resonators frequency by changing the wavelength of incident light. We used blue, green and red external diode lasers with wavelength of 450, 520 and 635 nm respectively and found out that the frequency response is totally different for all three wavelengths. The response also varies for different powers demonstrating photo-detector behavior. Since the total dielectric function ($\epsilon = \epsilon_1 + i\epsilon_2$) is strongly dependent on wavelength of light in both insulation (M) and conducting (R) phase, the optical absorption is dependent on frequency of incident light in both states of the material [20].

Another way to transform the insulating phase to metallic phase in VO_2 is by applying electric field. Conduction electrons are produced by quantum mechanical tunneling in insulating phase across the band gap [21]. This transition can either be because of joule heating or injection of charge using so called quantum mechanical tunneling mechanism [22]. Here we deposited ultrathin VO_2 films on a suspended micro-string resonator with contact pads for sourcing current or measuring resistance. We applied electric field across the string and measured the mechanical response of the micro-resonator as a function of electric field. We observed a blue shift in mechanical frequency for a critical DC and AC voltages applied to the contacts. The resonant behavior of the strings was different below, at and above that voltage. We also studied electro-optic effect while applying constant voltage and varying the input optical power and vice a versa.

1.2 Literature & background

Micro-electro-mechanical resonators (MEMS) offer a sensitive, miniaturized and robust platform for characterizing materials at very small scale. We need tiny devices to see the effects at small scale. These devices are distinctly different from molecular nanotechnology or molecular electronics and usually fabricated with micromachining with device size ranging from less than one micrometer up to one millimeter. The design and fabrication of these systems represent major breakthroughs in miniaturization technology, leading to a paradigm shift in engineering and opening up a wide range of applications [23]. Their applications are enormous from accelerometers and gyroscopes in automobiles, to inject printer cartridges, physical, chemical and biological sensing, micro engines, micro transmissions, optical switches for data communication and list goes on. Fabrication of these devices includes silicon fabrication technology, with molding, plating, wet and dry etching etc [23].

MEMS devices with embedded microfluidic channels have gained tremendous attention from scientific community because of their ability to characterize liquids with extremely small amount in pico liter volumes. Characterizing small volumes made this technology potentially very useful to understand the biological systems. These devices have been demonstrated as micro pumps and micro needles [24], mass spectrometers for weighing single particle in fluids [25], measuring the growth of single cells inside the cantilever [26], density of single cells in microchannel cantilevers [27] and label free bio marker sensing and undiluted serum [28]. These observations proved this device as very sensitive tool to characterize polymeric samples with high sensitivity, selectivity and resolution.

Polymers and polymer like liquids go through phase transitions during heating. Typical characterization techniques used to measure these transitions are

DSC, DMA, DES etc. Out of these, DSC is used very often as it can accurately find the glass transition, re-crystallization and melting in polymers using a simple heat flow and temperature curve. However some of the transitions are out of the sensitivity limit of DSC and it also requires samples in milligrams. Some polymeric samples, specifically biological samples are sometime very expensive and available in minute volumes. Suspended micro-channel resonators provide a useful platform to study samples as small as in pico-liter volumes [29].

Phase transitions of nano-gram level liquid samples have been demonstrated using suspended channel micro-resonators using PEO-PPOPEO triblock copolymer (for micellization) and n-heptadecane (for freezing) as test materials [30]. Density changes in the samples were measured using resonance frequency shift as a function of temperature. The increased frequency corresponded to micellization in copolymer and freezing in n-heptadecane because of increased stiffness of the cantilever.

These resonators were also used to measure the temperature dependent density and volume contractions of ethanol-water binary mixtures for pico-liter volume samples at different temperatures [31]. The changes in the elastic modulus of the SMR and the mass density of the liquid caused the resonance frequency of the SMR device go through a minimum at a certain temperature which shifted to low temperatures with increase concentration ethanol fraction. This platform was suggested to study temperature dependence of binary mixtures at micro-scale.

Thermoplastic and Thermoset Polymers are versatile materials with well-established applications in the pharmaceutical [32], manufacturing, [33], chemical, [34], microelectronics [35] and food industries [36].

Polymers have recently been shown to be promising candidate for applications in non-volatile memory [37], energy storage [38], and biomimetics [39] because of their various properties at nanoscale. These measurements at

such a small scale required to be very precise in order to accurately measure stability, durability and purity of the polymer. Most of these characteristics can be investigated using thermal properties of polymers such as glass transition (T_g), crystallization (T_c), enthalpy relaxation, and melting (T_m) [40]. In addition to these well-known transitions, certain polymers may also exhibit a β -relaxation/transition, which is due to localized movements in the main chain or the movement of a very large side chain [41]. For large scale applications, most of these transitions can be probed with conventional techniques such as differential scanning calorimetry (DSC), [42], [43], [44], dynamic mechanical analysis (DMA), [45] thermomechanical analysis (dilatometry), [46] and dielectric spectroscopy (DES) [47]. Undoubtedly, these techniques provide robust and well established platform for polymer characterization but are limited with sample size (5-10 mg) and dimensions. This dictates to develop new tools which can probe nano-scale properties of polymers with samples in sub-micro-grams. Micro-electro-mechanical resonators (MEMS) offer advantages over these techniques as they offer polymer characterization with high sensitivity, small sample size, shape independence, faster operation and wide dynamic range of measurements [48], [49], [50].

Two solids made of the same elements but with different geometries of atoms or crystal phases can produced different properties. The transformation from one solid phase to another solid phase is called solid-solid transition. This structural transition usually depends on external factors like temperature and pressure. Transition metal oxides are considered one of the most interesting classes of solids which exhibit fascinating macroscopic quantum properties including superconductivity, magnetism, and insulator to metal transition. The nature of metal-oxygen bond defines these properties depending on its strength variation from ionic to highly covalent or even metallic [51]. Out of many strongly correlated oxides, V–O system is one of

the most attractive materials because of its ability to form diverse variety of oxides e.g. VO, V₂O₃, V₃O₅, V₄O₇, V₅O₉, V₆O₁₁, V₇O₁₃, V₈O₁₅, VO₂, V₂O₅ etc. [52]. Vanadium dioxide (VO₂) is the most interesting compound because of its insulator to metal transition near room temperature. The nature of phase transition in VO₂ is still controversial but modification and modulation mechanisms of this phase transitions make it very important material for future switching and sensing applications [53], [54], [55].

1.3 Technological significance of current study

1.3.1 Probing phase transitions in polymeric liquids

Micro resonators, such as microstrings and microcantilevers, have been previously employed for thermal analysis (of small masses) of polymers [48], [49], [56], [57]. Both of these techniques require special spray coating or ink jet printing to deposit nanograms of sample [58]. Another challenge (when using microstrings or microcantilevers) is sublimation of the sample during heating. In order to overcome these difficulties, we have developed a microchannel cantilever consisting of microfluidic channel integrated on top of the cantilever. With the volume of the microchannel ~ 50 pL, the resonance frequency of the cantilever is ~ 150 kHz while its quality factor lies in the order of six to eight thousand. These values ensure high resolution in detecting any changes in the resonance frequency. Previously, this principle and the device have been successfully employed to detect sub attogram mass, and the density and viscosity of picoliters of confined liquids and thermal analysis for binary liquid mixture [59], [60], [61], [62]. Without any complicated protocols or equipment, the polymer samples can be loaded into the microchannel using melt infiltration. In order to detect thermal transitions,

the polymer-filled cantilever is heated under high vacuum. Although the cantilever is operated at low pressure ($\sim 5 \times 10^{-6}$ mbar), the polymer is enclosed within the microchannel which keeps the sample at atmospheric pressure. The incorporation of this microchannel enables the measurement of all thermal transitions up to (and including) the melting point. As a result, multiple heating cycles can be used to probe the transitions of the material in order to study its reversibility/hysteresis. To test the cantilever systematically (as a platform for thermal analysis), two different polymers were chosen as a case study such as biodegradable, semi-crystalline poly (L-lactide) (PLA), and amorphous poly(methylmethacrylate) (PMMA). The aim of this study was to use a miniature, robust, and sensitive platform to obtain accurate information about the thermal events occurring in the polymers. Thermal characteristics such as T_g , T_c , T_m and T_β are investigated and the results are compared to those obtained from conventional DSC.

1.3.2 Probing phase transitions in phase change solids

Phase transitions in solids can be observed at macro-scale using thermodynamic parameters by observing pressure vs. temperature phase diagram. Depending on the nature of the transition (first or second order), thermodynamic parameters would have either step or gradual change with each phase existing at the minimum energy state. We will use Vanadium dioxide thin films deposited on miro-resonating strings and will study the mechanical parameters change because of the phase transition in VO_2 .

Microelectromechanical (MEMS) resonators have demonstrated many attributes in terms signal processing, communication, frequency mixing, modulation and filtering purposes which have potential applications in sensing, detection (temperature, mass and humidity) and energy harvesting [63]. Among all the applications tuning or modulating frequency is the fundamental requirement of a resonator on which device performance depends by and

large. Among many materials studied in the past vanadium dioxide (VO_2) is one of the key material which can satisfy these demands to a larger extent because of its phase changing nature [64]. It possesses a reversible metal insulator transition (MIT) ideally at 68°C where monoclinic (M1 phase-insulator) phase transforms to tetragonal or rutile (R phase-metal). This phase transition results in a change to the electrical resistance by more than three orders of magnitude and significant change in the visible light transmittance. Although this transformation depends predominately on externally applied conductive heat, but recently radiative heat, electric field, pressure and optical excitation have been used . Recently it has been observed that VO_2 also changes its structure from M1 to R phase due to an externally applied DC electric field ($> 1 \text{ kV/m}$) at room temperature, known as the electric field induced MIT (EMIT) [55]. Here we will show that these transition can be also activated by a broad spectrum of optical wavelength operating at low power ($<100 \mu\text{W}$) as well as very low AC electric field. By fabricating suspended VO_2 microstring MEMS resonator we demonstrated the tuning of resonance frequency (both positive and negative direction) of the device can be achieved 3 to 4% by applying different wavelength of the light of very low power. Further, we will also show by changing the frequency of the applied AC electric field, the resonant frequency of the resonator can be tuned. These experiments may provide a new platform for MEMS based frequency modulation applications.

1.4 Thesis objective and organization

This thesis is organized in a way that it first introduces micro-electro-mechanical resonators with various geometries focusing on advantages they possess over the conventional materials characterization techniques. Chapter 1 and Chapter 2 will introduce important aspects pertaining to the thesis as a whole, including motivation towards the research. Subsequent chapters will follow

the experimental work in a chronological fashion. The content of each study will be presented in a journal article format because either the work has been submitted for publication or the manuscript is ready to be submitted. Each chapter will be started by giving the important aspects of the study with experimental outline, highlighted results and procedures and important analytical or simulation work in subsequent order. We would deeply discuss our results with a potential impact towards technological important of the the study. Results will be concluded in line with the objectives of the study and all the the parties involved will be acknowledged. References for all chapters will be presented at the conclusion of the entire thesis.

Chapter 1 provides an introduction to micro-electro-mechanical systems with focus on suspended microchannel resonators and clamped-clamped beam resonators. The chapter will start with introducing microchannel resonating system and how it can be used to probe phase transitions in liquids. A brief comparison between this technique and current state of the art thermo-mechanical analysis techniques will also be discussed. Later, the main characterization technique which is Laser Doppler Vibrometry (LDV) will be discussed in details. After completing the polymer characterization part, a brief introduction to microstrings resonators along with pulsed laser deposition process (PLD), nucleation and growth mechanism in thin films and finally deposition of VO_2 thin films on microstrings resonators will be discussed.

In Chapter 2 , Theory of micro-electro-mechanical systems used in this study, is discussed. Dynamics of both microchannel resonators and micro-string resonators is explained mathematically. Different models are proposed for research done in this thesis.

In Chapter 3 , relevant characterization or fabrication techniques employed during the work will be described. The focus will be on major tech-

niques involved in both characterization of liquid samples with suspended-micro-channel resonators (SMCR) and integration of thin films with micro-string resonators.

Chapter 4 will present thermo-mechanical analysis of polymeric liquids with SMCR. As a case study, two well known polymers will be considered and mechanical response of the resonator at its resonance frequency will be studied with the empty channel and after filling the channel with PLA and PMMA. Results will be compared with standard differential scanning calorimeter (DSC) and a mathematical model of the system will be developed and analyzed for both empty and polymer filled resonators as a function of temperature. Phase transitions in both polymers obtained with SMCR will be compared with conventional DSC technique. A comparison table between current state of the art techniques will also be shown which would help understanding the important technological aspects of current study.

Chapter 5 is a thorough investigation of pulsed laser deposited VO₂ thin films process optimization. In this section we first investigate the role of oxygen flow rate on the quality of polycrystalline VO₂ thin films deposited on Si substrate. The phase of thin films will be confirmed with XRD for each oxygen flow rate. The quality of the films will be confirmed with two probe resistivity measurements with the probe station showing the width and order of magnitude of change in electrical resistance as a function of temperature. Surface potential studies will be done with Kelvin-probe force microscopy (KPFM) and surface roughness of the films will be measured with tapping mode AFM. It has been known that insulator to metal transition (IMT) and formation of VO₂ strongly depends on oxygen pressure but no study in literature was found which shows how the quality of the thin films changes with flow rate of oxygen. After confirming the structural change, KPFM, tapping mode AFM, electric field assisted insulator to metal transition (EIMT) and resistance vs. temperature studies will be carried out to see surface potential,

roughness, onset electric field for insulator to metal transition as a function of temperature and order of magnitude change in resistance within and across the thin film respectively. After developing thorough understanding of optimized growth and quality of VO₂ films on amorphous (SiO₂, a series of processes and materials will be investigated as potential candidates for a VO₂ microstring fabrication process. A microstring (doubly clamped cantilever) will be chosen a model platform as the resonance frequency of such a device is much higher than a single clamped beam, and therefore we believe a more sensitive device could be realized. Using a starting substrate of Si/SiO₂ (1.5 μm)/Si₃N₄ (200 nm) a fabrication process consisting of photolithography, sputtering, RIE, VHF, and ICP-RIE will be discussed. The resulting string showed a mechanical resonance frequency increase of over 5 % across the phase transition when cycled through control heating with peltier element while measuring its resonance frequency continuously. we will then conduct electrical, thermo-mechanical, opto-mechanical and electro-mechanical response of these resonators.

In chapter 6, thin films deposited on pre-released microstrings with various length sizes of 400 μm to 50 μm in length. Dynamic mechanical response (resonance frequency, quality factor, amplitude of vibration) will be conducted with LDV. The main objective in this chapter will be to understand the string response as a function of input optical power, optical wavelength and dynamics change while scanning the dynamic mechanical response by irradiating the laser at the center of the resonator. All supporting results like XRD, and EIMT will also be discussed.

Chapter 7 is extension of Chap 6 where a different mechanism of frequency tuning of VO₂ coated resonator is discussed. The objective of this chapter is to understand the opto-thermal effects and heat transport mechanism and their implications on mechanical resonance frequency of the resonator.

Chapter 8 will be focused on electric field assisted insulator to metal

transition in VO_2 resonators. We have developed a two contacts vacuum probe station with micro-manipulators to control the lateral and vertical motion of the probes. Male-female connectors were soldered with the probe wires and connected to external power supply via BNC connectors. Both ac and dc voltages will be applied across the strings via Ti/Au contact pads and mechanical response of the strings will be recorded as a function of input voltage and frequency. We will then move on and summarize our findings in chapter 9 with recommendations for future study in this field. Chapter 4-8 are summarized in following table.

MEMS systems used for studying phase transitions along with thermo-mechanical and electro-mechanical characterization are schematized in Figure 1.1

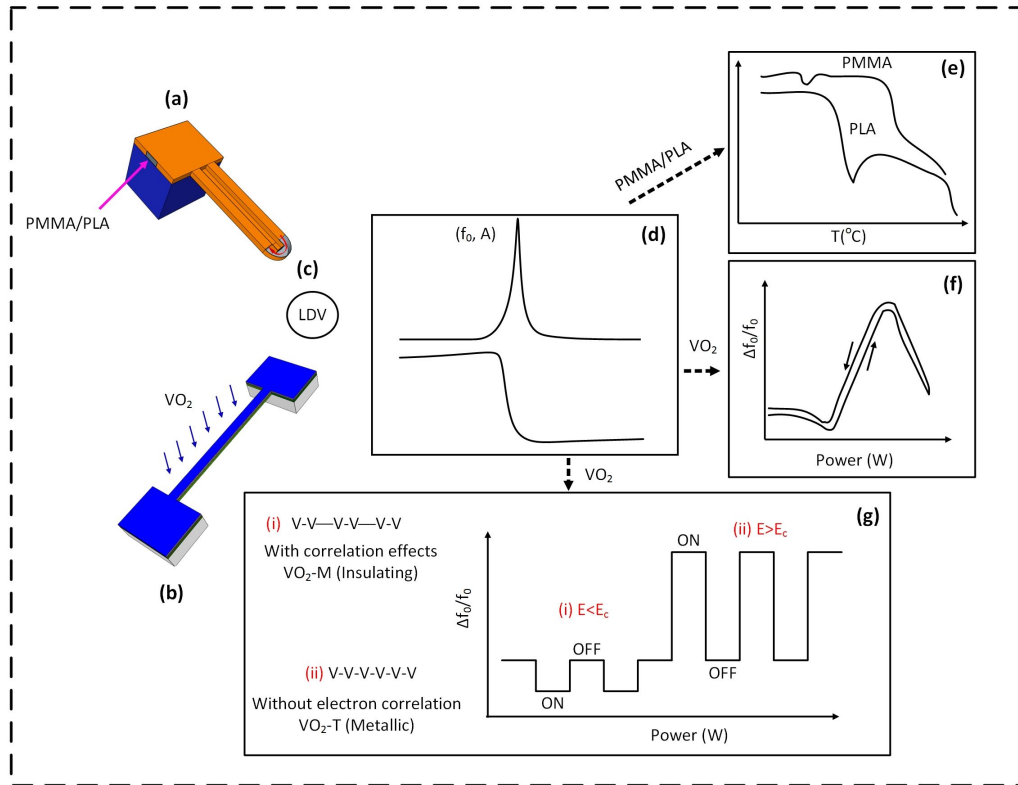


Figure 1.1: Two types of micro-electro-mechanical resonators (MEMS resonators) employed to characterize materials at micro scale in this dissertation. Suspended micro-channel resonator (SMCR) shown in (a) will be used to characterize two well known polymers by melt flowing the polymers in micro-channel. Cartoon shows the micro-channel opened at the tip of the cantilever. Frequency and amplitude data (d) was collected with Laser Doppler Vibrometer (LDV) model MSA 500 and thermo-mechanical response of the strings (frequency vs. temperature) would be correlated with stiffness change of the cantilever as a function of temperature (e).

Table 1.1: Brief summary of each chapter. This table summarizes the topics of each chapter followed by detailed findings. The objective of each chapter from 4-8 is described first. Major findings are the outcomes of the research done on that topic. Each chapter is a an independent project.

Chapter 4

Title	Probing phase transitions in polymeric liquids
Objective	Take two well known polymers and detect their phase transition behavior with suspended microchannel resonators
Major findings	Successfully melt flow the polymers inside the microchannel. Frequency variations as a function of temperature were studied and characteristic thermodynamic parameters (glass transition, melting, crystallization and beta transition were obtained and compared with standard DSC results.

Chapter 5

Title	Probing phase transitions in solids: VO ₂ thin films
Objective	Optimization of thin films deposition process with PLD
Major findings	Deposited thin films on various substrates with control parameters. Studied the effect of flow rate on insulator to metal transition in thin films. Deposited thin films on MEMS with optimized conditions. High temperature XRD studies confirmed the structural transformation of VO ₂ films from monoclinic to rutile phase.

Chapter 6

Title	Optically induced phase transitions in VO ₂ micro-resonators
Objective	Modulation of mechanical response of micro-resonators with optical power
Major findings	Demonstrated the strings modulation for various light intensities and wavelengths.

Chapter 7

Title	Spatial frequency tuning of VO ₂ resonators with opto-thermal excitation.
Objective	Mechanically detect the dynamics of string with varying the optical power source laterally
Major findings	Mechanical response of resonator was characterized as a function of optical power and distance from the center of the resonator. Both frequency and amplitude dependence were studied

Chapter 8

Title	Electric field induced phase transition in VO ₂ deposited micro-resonators
Objective	Mechanically detect the dynamics of string with applied electric field
Major findings	Mechanical response of resonator was characterized for both AC and DC fields. Both frequency and amplitude dependence were studied.

Chapter 2

Theoretical background

2.1 Introduction

Euler-Bernoulli beam theory is widely used to successfully predict the dynamics of micro- and nano-cantilever beams. This theory can accurately predict the resonance frequencies in linear regime of resonator. The linear effects are valid with some errors ($\pm 2\%$) as long as the length to width ratio of the resonator is greater than 2 [65]. The non-linearity is found to be dependent on aspect ratio and resonators with aspect ratio > 2 in first resonance mode have demonstrated validation of Euler-Bernoulli's beam theory. Since the devices we will be studying here have the aspect ratio more than 10 so we will be within the linear regime and will not consider non-linearity. In first part of theory, we will discuss cantilever resonators with microfluidic embedded channel. We will develop a mathematical model and will predict how measuring frequency shift can be correlated to the stiffness of the material inside the channel.

In second part of theory, we will consider doubly clamped beam resonators (micro-string resonators) and will see how their dynamics change with surface stress, temperature, electric field and optical power. In both cases we will restrict to the fundamental first mode of vibration of these devices.

2.2 Dynamics of suspended micro-channel Cantilever

A beam cantilever incorporating a fluidic microchannel is called suspended microchannel resonator (SMCR). Beam cantilevers provide precise measurement of structural, physical and chemical properties of gases and thin films deposited on cantilever surface by measuring the resonant behavior of the cantilever. The same task gets difficult and challenging in case of high viscosity liquids which cause severe damping lowering the cantilever quality factor and resonance to a near zero level. A research group in Massachusetts Institute of Technology (MIT) came up with an idea of placing the solution inside a microchannel embedded in a resonator and surrounded by vacuum [6]. Since liquids do not degrade the mechanical resonance properties of the resonator, it is possible to measure the changes related to the density and viscosity of the liquids with high resolution. A schematic for experimental set up is shown in Figure. 2.1.

The resonance frequency of a simple resonator with a mass m , is given by,

$$f = \frac{1}{2\pi} \sqrt{\frac{k}{m}} \quad (2.1)$$

where, k (N/m) is the spring constant and m (kg) is the total mass of the resonator. The value of spring constant is related with Young's modulus E , and geometry of the cantilever by the equation [57],

$$k = \frac{Ewt^3}{4l^3} \quad (2.2)$$

In case of a channel embedded on top of this beam resonator, geometrical factors will change the stiffness of the cantilever. Very small changes in both mass and spring constant will cause changes in resonance frequency which will determine the sensitivity of the device. If the channel is filled with a liquid with certain density, the relation is now of the form,

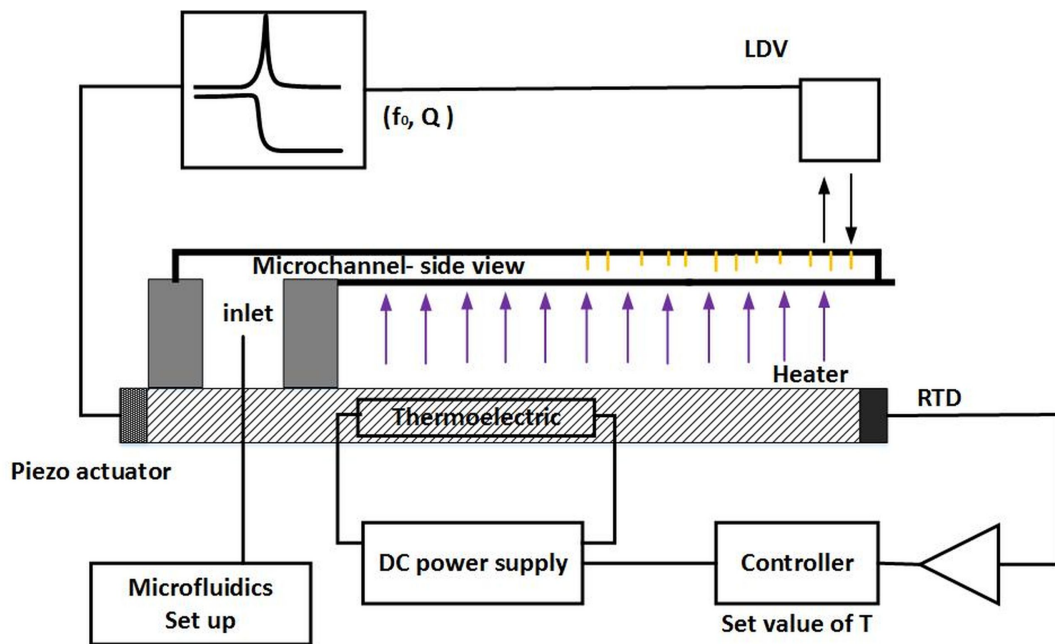


Figure 2.1: Side view of a cantilever with a microfluid channel on top of it. Resonator was oscillated at its first resonance mode with a piezo actuator. Temperature was controlled via feedback circuit using a DC supply to the thermoelectric peltier element. Data acquisition was done with Laser Doppler vibrometer by measuring the FFT spectrum of resonance frequency of the device.

$$f = \frac{1}{2\pi} \sqrt{\frac{k_{eff}}{m^*}} \quad (2.3)$$

where k_{eff} is the spring constant of the coupled system of the channel and the material inside it. This becomes more significant factor when the liquids inside are of high viscosity and or the liquid is subjected to temperature fluctuations. The change in k_{eff} will correspond to a change in the Young's modulus of the material, and a change in the mass will correspond to the density of the liquid. Effective spring constant k_{eff} depends on the cantilevers material stiffness, geometry and the viscosity of the liquid inside the channel. Any change in k_{eff} can be attributed as a change in mechanical behavior of the material.

Since the frequency of resonator is a function of modulus, temperature and mass, we will now see how these parameters can effect the resonance. The resonance frequency of the cantilever at room temperature T_0 is given by the eq. 2.1 which can be re-written as

$$f_c(T) |_{T=T_0} = \frac{1}{2\pi} \sqrt{\frac{k_c}{m_c}} \quad (2.4)$$

where,

$$k_c = \frac{E_c w t^3}{4l^3} \quad (2.5)$$

$f_c(T) |_{T=T_0}$ is the frequency of the cantilever at temperature ($T_0=25^\circ \text{C}$), and k_c, m_c are stiffness and mass, of the cantilever respectively. Since E_c is a strong function of temperature so considering silicon nitride as a linearly elastic material, its elastic modulus can be written as

$$E_c(T) = a(T)E_c |_{T=T_0} \quad (2.6)$$

Where $a(T)$ is the coefficient of elastic modulus change with temperature for silicon nitride. Since the material would expand on increasing temperature so

geometrical factors are also expected to change. If α is the thermal expansion coefficient of silicon nitride then the change in dimensional parameters as a function of temperature T can be written as

$$w(T) = w(1 + \alpha T), t(T) = t(1 + \alpha T), l(T) = l(1 + \alpha T) \quad (2.7)$$

set $b = 1 + \alpha T$ and substitute these values in eq. 2.5 \Rightarrow

$$k_c(T) = \frac{(E_a(T))(bw)(bt)^3}{(bl)^3} = a(T)b \frac{Ewt^3}{l^3} = [a(T)b]k_c \quad (2.8)$$

This temperature dependent value of k_c will change the eq. 2.4 as:

$$f_c(T) = [a(T)b]^{\frac{1}{2}} f_c(T) |_{T=T_0} \quad (2.9)$$

Changes in thermal expansion coefficient of silicon nitride (α) are very small for the temperature range we are working with, therefore we can neglect changes in b and only effective parameter will be $a(T)$. After loading polymer into the channel, we can model the system as two parallel springs connected to the cantilever and polymer mass as shown in Figure. 2.2

Resonance frequency of the coupled system shown in Figure. 2.2 can be written as;

$$f_{c+p}(T) |_{T=T_0} = \frac{1}{2\pi} \sqrt{\frac{k_c + k_p}{m_c + m_p}} \quad (2.10)$$

Where m_p and k_p represent mass and stiffness of loaded polymer into the micro-channel. Eq. 2.10 can also be expressed as;

$$f_{c+p}(T) |_{T=T_0} = f_c(T) |_{T=T_0} \left(1 + \frac{k_p}{k_c}\right)^{\frac{1}{2}} \left(1 + \frac{m_p}{m_c}\right)^{-\frac{1}{2}} \quad (2.11)$$

Since we assume that k_c is almost independent of temperature in the temperature window we will be doing our experiments, we can assume it to be constant and consider only the stiffness of polymer changes with temperature.

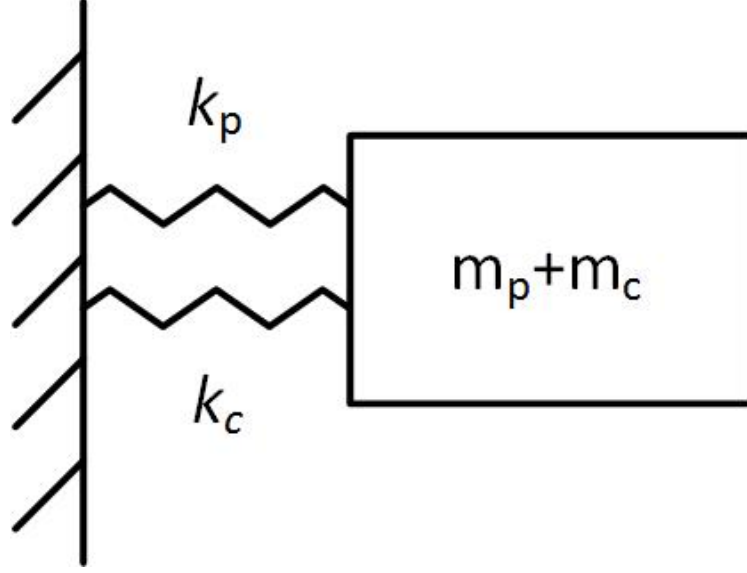


Figure 2.2: Mathematical model for suspended micro-channel resonator. Cantilever without the polymer has a stiffness k_c while k_p is the stiffness of the polymer. Total mass after loading will represent the mass of the system.

\Rightarrow

$$f_{c+p}(T) |_{T=T_0} = f_c(T) |_{T=T_0} \left(1 + \frac{k_p(T)}{k_c}\right)^{\frac{1}{2}} \left(1 + \frac{m_p}{m_c}\right)^{-\frac{1}{2}} \quad (2.12)$$

where $k_p(T)$ is the temperature dependent stiffness of the polymer. Considering the fact that the change in $f_c(T)$ is very small as compare to $f_p(T)$ (ppm), we can say that the only change in the frequency of the cantilever $f(T)$ would be because of the change in the stiffness $k_p(T)$ of the polymer. By setting

$C = \left(1 + \frac{m_p}{m_c}\right)^{-\frac{1}{2}}$, one can extract $k_p(T)$ from eq. 2.12 which is;

$$k_p(T) = k_c \left[\left(\frac{f_{c+p}(T)}{f_c(T) |_{T=T_0}} \right)^2 C^2 - 1 \right] \quad (2.13)$$

Using this equation, we can study the stiffness change in polymer as a function of frequency of empty and polymer filled silicon nitride cantilever. We saw sharp changes in $k_p(T)$ at the temperatures where glass transition, crystallization and melting of the polymer took place with extremely high sensitivity. This section demonstrated the use of these devices to probe phase transitions

in polymeric liquids using suspended micro-channel resonators.

2.3 Dynamics of micro-string resonator

Using a doubly clamped beam (micro-string) resonating system, we will explore the phase transitions in solid materials. Vanadium dioxide has reversible insulator to metal transition which not only transforms the physical structure but also changes its electrical, optical and thermal properties. A small thermal mass can be obtained in the form of thin films on the resonating system using pulsed laser deposition process. We used PLD because it can stoichiometrically transform the target material onto the resonator and form high quality films. In this section, theoretical understanding of insulator to metal transition in resonating system will be described for electric field and optical power as external stimuli. We will briefly discuss the effect of change of crystal structure of thin film on the resonator and how geometrical and modulus changes can contribute to create surface stress on micro-strings.

2.3.1 Current driven insulator to metal transition

VO₂ coated microstring resonators were subjected to electric field via contact pads at two ends with indigenously built vacuum probe station. Electric field was applied across the string and mechanical parameters of the string were recorded as a function of voltage applied. The system is schematically shown in Figure 2.3.

The nature of the electronic behavior of phase transition in VO₂ still poses many open questions. Several attempts have been made on understanding the nature of insulating to metallic state transition. The transition could be related to a Mott-Hubbard scenario where including nearest neighbor Coulomb interactions of electrons causes a d band split into two sub-bands and opens up a charge gap. This gap transitions the material to an insulating

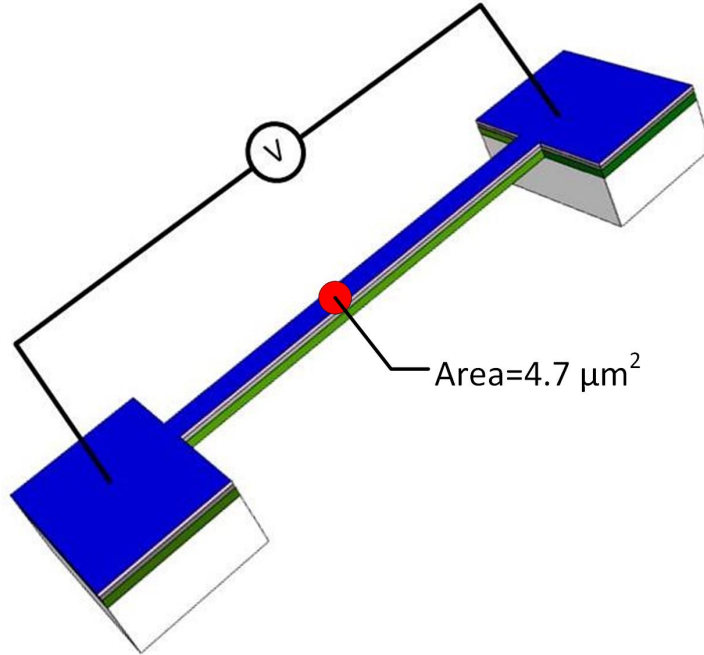


Figure 2.3: Schematic of mechanical detection of electric field assisted insulator to metal transition in O_2 coated micro-string resonator.

state [66]. While numerous studies relate the nature of the transition to Peirels distortion which states that a one dimensional equally spaced chain of atoms each with one electron is unstable which results as a crystal structure change in VO_2 and hence the electronic properties at a critical temperature [67], [52]. We will briefly describe how joule heating or avalanche breakdown/electric field breakdown can cause an abrupt change in resonance frequency of the micro-strings above a critical field. Recently, electric field breakdown without joule heating has been studied using AFM and electrostatic force microscopy (EFM) where it was concluded that IMT can be triggered with a critical field applied through AFM tip on thin films of VO_2 [68].

When voltage is applied across two terminals of the VO_2 microstring, IMT can be triggered if the local temperature could reach above the critical temperature of VO_2 thin film. The heat supplied to the string will be a balance between heat dissipated during the joule heating and heat lost to the environment by the string. Assuming the heat supplied to the string passes only through the

top layer which is VO₂, we can write down the joule heating of the system as;

$$\frac{dQ}{dt} = \frac{V^2}{R} - \kappa(T_{VO_2} - T_0) \quad (2.14)$$

where Q is the net heat going into the VO₂ film, V is the applied voltage and κ is the effective thermal conductivity T_{VO_2} is the temperature of top layer in the string, and T_0 is room temperature. This equation valid once steady state conditions are achieved. Realistically the localized variations in temperature are expected to be a function of time which means the process can be modeled as time dependent joule heating which can be written as;

$$\frac{dQ}{dt} = C_p \left(\frac{dT_{VO_2}}{dt} \right) \quad (2.15)$$

where C_p is specific heat at constant pressure. Eq. 2.15 can be solved for time dependent temperature of the top layer which is;

$$T_{VO_2}(t) = T_0 + \frac{1}{\kappa} \left(\frac{V^2}{R} \right) (1 - \exp(-\frac{\kappa}{C_p} t)) \quad (2.16)$$

In our studies, mechanical frequency change was studied as a function of applied voltage with LDV using a minimum possible acquisition time. The response of the resonator within that time scale (0.5 seconds) was much faster than the acquisition time upon application of step voltage. Mechanical response of microstrings as a function of low frequency AC signals will be discussed in chapter 8.

Another phenomena, in addition to joule heating effect could be Poole-Frenkel effect [69] which can create additional charge carriers caused by the lowering of Coulomb barrier because of high electric fields. The transition in VO₂ can either be due to structural change i.e. Peirels transition, Mott-transition where correlation energy between electrons become very significant when VO₂ is in insulating state. It is believed that the transition could be a combination

of both effects where not only crystal structure changes but also the charge carriers are weakly correlated in metallic phase leading to higher electrical conductivity.

VO₂ transition mechanism can also be explained by considering the electron-electron interaction and the difference between the insulating and metallic states charge carrier concentration (n_c) which can be achieved either by attaining a thermal equilibrium ($T = T_c$) or injecting charge carriers into the system via other excitation mechanisms e.g. electric field, light, Terahertz pulse, etc. Mott criterion states that the critical carrier concentration for a Mott insulator should follow the relation [70];

$$a_H n_c^{\frac{1}{3}} \approx 0.25 \quad (2.17)$$

where $a_H = \frac{\epsilon \hbar^2}{m^* e^2}$, with ϵ be the dielectric constant (~ 100 for VO₂, [69]), and m^* be the effective mass of electron having charge e ($\sim 3m_e$ [70]). The relation depends on dopant/impurity concentrations and this equation may be validated if the transition is considered to be dependent on carrier concentrations i.e. electronically driven. On the other hand, Hubbard-Mott transition occurs in another system V₂O₃ for which the transition is accompanied by a structural transformation at $T_c=150$ K [22]. Temperature and electric field dependent concentration of electrons which is induced due to Poole-Frenkel effect is given by;

$$n = N_0 \exp\left(-\frac{W - \beta \sqrt{E}}{k_B T}\right) \quad (2.18)$$

where N_0 is a constant independent of the field and only slightly dependent on temperature, W is the activation energy and $\beta = (e^3 / \pi \epsilon \epsilon_0)^{\frac{1}{2}}$ is the Poole-Frenkel constant. Also temperature dependent electrical conductivity of VO₂ is given by [71];

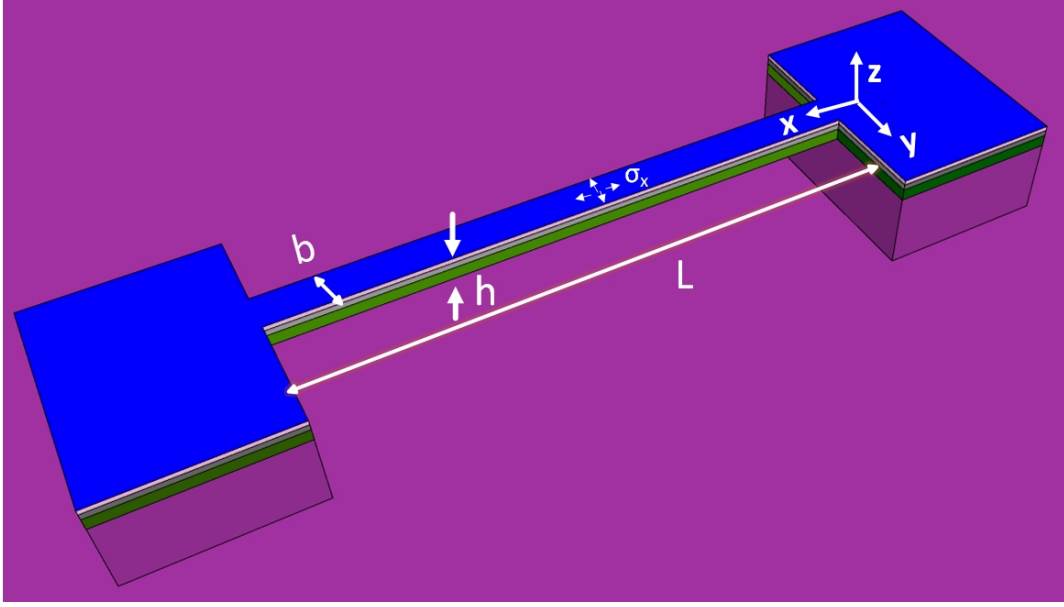


Figure 2.4: Surface stress on the micro-string generated by insulator to metal transition in VO₂ layer coated on Pt/SiN.

$$\sigma \sim \frac{1}{T^{3/2}} \exp(-E_a/k_B T + k_B T/\epsilon) \quad (2.19)$$

where E_a is the activation energy of conductivity and ϵ is a hopping constant which accounts the influence of thermal lattice vibrations.

Now that we discussed how the temperature and electric field can effect the physical properties of VO₂, we now jump into the real system of doubly clamped beams (micro-string resonators) and try to understand how the dynamics of the strings can change with electric field or thermal effects. We assume that the phase transition in VO₂ would cause a change in crystal structure of the top layer of the string at a critical applied electric field or temperature which will change the overall surface stress on the string resulting an increase in resonance frequency because of increased stiffness of the resonator. Consider L being the length of the micro-string, b as width and h as thickness of the string as shown in Figure. 2.4.

Resonance frequency of uncoated beam resonator is given by [72];

$$f_0 = 1.029 \frac{h}{L^2} \sqrt{\frac{E}{\rho}} \quad (2.20)$$

where ρ is the density of the material, E is Young's modulus, h is the thickness of the resonator and L is the length of the beam. Deposition of VO₂ on surface of Pt caused first surface stress because of film formation in a preferable way where lattice mismatch and defects created an average stress induced on the beam. For the sake of simplicity, we will not consider the effect of first stress on the resonance frequency but we will consider the component which comes because of changes happened in the VO₂ in presence of external electric field, and thermal power. First, consider the beam is unrestrained under application of a net surface stress induced by external excitation. The displacement field will be dependent on x and y coordinates and can be written as;

$$(u_x, v_x) = -\frac{(1-\nu)\sigma_s^T}{Eh}(x, y) \quad (2.21)$$

where u_x and v_y are displacements in the x and y directions, respectively; ν is Poisson's ratio, E is Young's modulus and σ_s^T is the total applied surface stress. If the beam is clamped, a displacement load must be applied in the x -direction. Displacements in the y -direction can be ignored as the length of the beam is much larger than its width. so set $y = 0$ and $x = L$ in eq. 2.21, the axial displacement would be;

$$u = -\frac{(1-\nu)\sigma_s^T}{Eh} \quad (2.22)$$

corresponding tensile load will be;

$$F_{axial} = (1-\nu)\sigma_s^T b, \quad (2.23)$$

where b is the length of the beam. This axial force will cause a change in the stiffness of the beam due to the change in crystal structure of the top layer and

hence a change in resonance frequency. We now can use Euler-Bernoulli beam theory to see how much change in resonance frequency will appear because of this tensile force. The governing equation for the deflection function w , for a beam of linear mass density μ and moment of inertia I , is:

$$EI \frac{\partial^4 w}{\partial x^4} - F_{axial} \frac{\partial^2 w}{\partial x^2} + \mu \frac{\partial^2 w}{\partial t^2} = 0, \quad (2.24)$$

with the clamped boundary conditions, i.e. $w = \frac{\partial w}{\partial t} = 0$, because beam does not move at boundaries, solving the equation with a solution $w(x, t) = W(x)exp(-i\omega t)$, we get following equation [73];

$$\frac{\Delta f}{f_0} = 0.1475 \frac{(1 - \nu)\sigma_s^T}{Eh} \left(\frac{L}{h} \right)^2 \quad (2.25)$$

Since the transition from insulating (monoclinic) to metallic (Rutile) VO₂ causes geometrical change in the top layer so we must also consider this effect in overall frequency change of the beam. Components of a strain tensor for an isotropic in-plane stress for a clamped beam can be written as;

$$\varepsilon_{xx} = 0; \varepsilon_{yy} = (1 + \nu) \frac{(1 - \nu)\sigma_s^T}{Eh}; \varepsilon_{zz} = \nu \frac{(1 + \nu)(1 - \nu)\sigma_s^T}{(1 - \nu)Eh} \quad (2.26)$$

Assuming Young's modulus of VO₂ thin films does not change with external electric field or temperature as a result of IMT in VO₂ [74], we have to incorporate that effect in the governing equation of frequency change of the beam.

$$\frac{\Delta f^G}{f_0^G} = -\frac{1}{2} \frac{\Delta \rho}{\rho} + \frac{\Delta t}{t} - 2 \frac{\Delta l}{l} = \frac{1}{2} \frac{\Delta V}{V} + \frac{\Delta t}{t} - 2 \frac{\Delta l}{l} \approx -\frac{3}{2} \varepsilon_{xx} + \frac{1}{2} \varepsilon_{yy} + \frac{3}{2} \varepsilon_{zz} \quad (2.27)$$

By comparing eq. 2.27 and 2.26, we obtained

$$\frac{\Delta f^G}{f_0^G} \approx \frac{(1 + \nu)(1 + 2\nu)(1 - \nu)\sigma_s^T}{(1 - \nu)Eh} \quad (2.28)$$

In case of VO₂, the top layer assumed to be changing its crystal structure at IMT resulting a change in Young's modulus E , we have to incorporate that effect in order to explain the results we obtained based on this assumption. In case of multi-layered MEMS structures, the Young's modulus E will be replaced by an effective Young's modulus \bar{E} [75] given by the equation

$$\bar{E} = \frac{E_i}{1 - \nu_i^2} \quad (2.29)$$

Resonance frequency of the first mode of the doubly clamped beam can also be expressed in terms of average bending stiffness \overline{EI} and linear density $\overline{\rho A}$ which is [76].

$$f_1 = \frac{\pi}{2l^2} \sqrt{\frac{\overline{EI}}{\overline{\rho A}}} \quad (2.30)$$

where

$$\overline{EI} = \frac{b \left[E_1^2 h_1^4 + E_2^2 h_2^4 + E_1 E_2 h_1 h_2 \left(4h_1^2 + 6h_1 h_2 + 4h_2^2 \right) \right]}{12 (E_1 h_1 + E_2 + E_2 h_2)} \quad (2.31)$$

and

$$\overline{\rho A} = \rho_1 A_1 + \rho_2 A_2 \quad (2.32)$$

here we considered two layers of the doubly clamped device with bottom layer having modulus, density, and thickness to be E_1, ρ_1, h_1 and top layer which is VO₂ having modulus, density, and thickness to be E_2, ρ_2, h_2 respectively.

2.3.2 Photo-Induced insulator to metal transition

In this section, we will describe another mechanism which can trigger the insulator to metallic transition in VO₂ thin films deposited on micro-string resonators. A focused beam of laser is directed on to the top layer of the beam and its dynamic response is recorded as a function of incident power of the laser. In the second part, we used external LED lasers with power while keeping the probe laser at a minimum power. Three wavelengths (635 nm, 520 nm and 450 nm) were used to pump the system while 635 nm built in laser in LDV with maximum power of 200 μW was used to probe the dynamics of the string by keeping its power at minimum which is measured as 22 μW . Experimental set up to carry out these measurements is shown in Figure. 2.5.

In case (a), where system was pumped and probed with the same optical source, we observed a decrease in frequency of the resonator when laser heating turned on for low power regime and an a sudden shift of frequency for intermediate powers and back to normal regime at high optical power. When we used external optical source to probe the system(case (b)), we observed a step increase in frequency when the probe laser was at its minimum power while the external laser with fixed optical power was used to excite the system. This was only true for 635 nm laser. With same optical power of the other two external sources i.e. 520 nm (green) and 450 nm (blue), we saw a step decrease in frequency at minimum probe laser (which is always 635 nm). In case of green laser, the trend transformed to step increase in frequency when the probe power was increased. This was not the case for blue laser (450 nm) for which we saw a decrease in frequency in ON state for all the power levels of the probe laser (keeping the pump laser at a constant value). In order to further investigate, we set the internal power to level 3 and let the system running for a longer time. We saw a shift in resonant behavior of resonator after few minutes i.e. the increase in frequency when

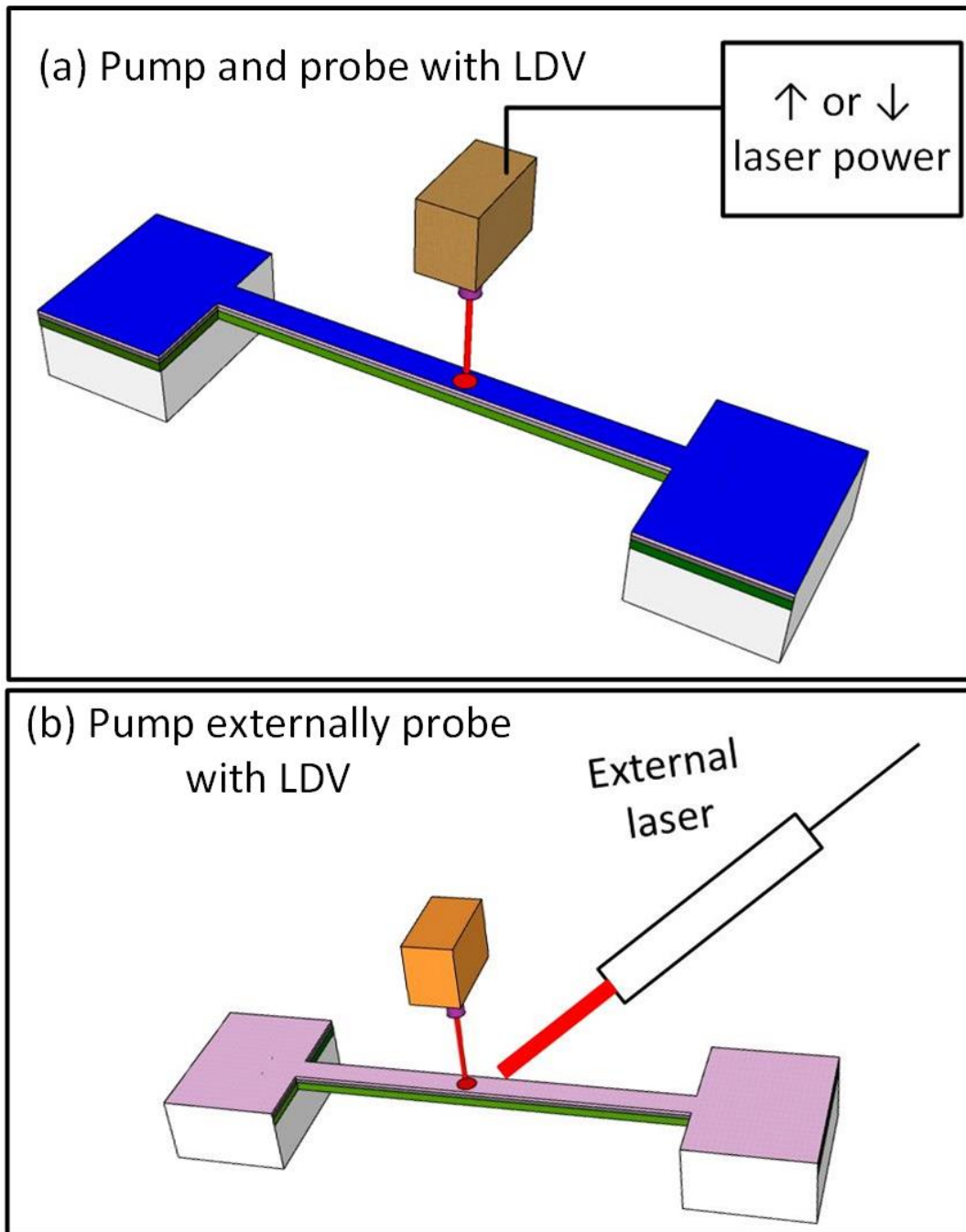


Figure 2.5: Schematic of mechanical detection of photo induced insulator to metal transition in O_2 coated micro-string resonator. Pump and probe using the same built in source in LDV (635 nm laser) is shown in part (a). In part (b), we set the internal power of LDV to minimum while using an external source to pump the system with three different wavelengths i.e. 635 nm, 520 nm and 450 nm respectively.

the laser is ON. The shift in the resonant frequency can be attributed to the temperature-dependent variations of material properties, e.g. the coefficient of thermal expansion (CTE, α) and Young's modulus (E).

2.3.3 Light-resonator interaction and heat transport

Interaction of light with the resonator is through thermal and mechanical processes. Part of the input optical power P_{in} will be reflected ($P_{ref} = rP_{in}$) where r is the reflection coefficient of the top layer of the resonator. The absorbed light portion can be described by [77];

$$P(z) = (1 - r)P_{in}e^{-\gamma z} \quad (2.33)$$

where γ is absorption coefficient. The absorbed power raises the local temperature $T(x, y, z, t)$ until the steady state equilibrium is achieved when the radiated thermal power and heat power conducted towards the anchors of the string is balanced. Temperature distribution can be calculated using heat equation;

$$\rho C_p = \frac{\partial T(x, y, z, t)}{\partial t} = \kappa \nabla^2 T(x, y, z, t) + P(x, y, z, t) \quad (2.34)$$

where ρ is density of the material, C_p is heat capacity at constant pressure, κ is the thermal conductivity and

$$P(x, y, z, t) = I(x, y, z, t)(1 - r)\left(\frac{\partial}{\partial z}\right)e^{-\gamma z} \quad (2.35)$$

is power density of the absorbed portion of the light. $I(x, y, z, t)$ is the time dependent intensity distribution of the light falling on the string. Since we are doing these experiments under high vacuum environment so we will only consider the heat loss because of radiation. Heat gained by the system

and heat lost by the system will compete to achieve a stable temperature at a uniformly heated spot on the string. We will set the boundary conditions by considering the increase or decrease in temperature is caused by the input power. Using Stefan-Boltzmann Law;

$$\hat{n} \cdot (-\kappa \nabla T) = e\sigma(T^4 - T_0^4) \quad (2.36)$$

where $\sigma = 5.67 \times 10^{-8} \text{Wm}^{-2}\text{K}^{-4}$ and \hat{n} is a unit vector normal to the string and e is the emissivity of the material. Solving equation 2.34 will provide temperature profile as a function of incident power of light.

2.3.4 Effect of materials properties on string dynamics

Vibration of a clamped-clamped beam can be described by Euler–Bernoulli beam theory, with the resonance frequencies given by

$$f_0 = 1.029 \frac{h}{L^2} \sqrt{\frac{E}{\rho}} \quad (2.37)$$

If temperature is raised, both geometrical changes because of thermal expansion of materials and temperature dependence of Young’s modulus will effect the resonance frequency. Dimensional changes with temperature will cause its length and thickness increase by a factor of $(1 + \alpha\Delta T)$ while its density will decrease by a factor of $(1 + \alpha\Delta T)^3$ which will result the frequency to increase by a factor of $(1 + \alpha\Delta T)^{\frac{1}{2}}$. Young’s modulus also depends on temperature given by the equation [78]

$$E(T) = E(T_0) \left[\frac{1}{(1 + \sum_{n \geq 1} \beta \Delta T^n)} \right] \quad (2.38)$$

where β is thermal coefficient of the elastic compliance constant (S) which is $3.16 \times 10^{-6} \text{K}^{-1}$ for Si_3N_4 [79]. Higher order β are very small and can be ignored. The resonance frequency of the device will be proportional to these

changes which is;

$$f(T) \propto \sqrt{\frac{1 + \alpha\Delta T}{1 + \beta\Delta T}} \quad (2.39)$$

For a bi-material string resonator, mathematical treatment as shown in eq. 2.30, 2.31 and 2.32 will be used for optical excitation of the system as well.

Chapter 3

Fabrication and characterization

Several different techniques were used in the fabrication and characterization of micro-resonators. Details about the fabrication process of suspended micro-channel resonators are given elsewhere [80]. We will discuss the detailed fabrication process for micro-string resonators in the forthcoming chapters. Fabrication process was done at Nano-fab at University of Alberta involving all clean room processes for device fabrication. Laser Doppler Vibrometer (LDV) was used to probe the mechanical response of these devices at their respective resonance frequencies in first modes. Pulsed laser deposition (PLD) was used to deposit thin films on micro-string resonators and various spectroscopic and microscopic techniques were used for materials characterization as well as visualization of devices. We will discuss major techniques and processes involved in device fabrication, deposition and characterization in this chapter.

3.1 Microfabrication and process flow

We used two different devices for thermomechanical characterization of materials. Clamped and suspended micro-channel resonator was fabricated for studying polymers and liquids while doubly clamped micro-string resonator

was fabricated to study phase change materials in this case VO₂.

3.1.1 Fabrication process for micro-channel cantilevers

In order to do fabrication of the hollow cantilevers, standard micromachining techniques were used at micro/nano fabrication facilities at University of Alberta. The process is schematically shown in Figure 3.1

The process started with 500 μm thick Si wafer, piranha cleaned and oxide layer removed with RIE on top of bare Si, a 750 nm thick layer of SiN was deposited using Low pressure chemical vapor deposition (LPCVD) as shown in part (a) of Figure 3.1. The layer of SiN will be the base layer of the cantilever. In step (b), 3.2 μm thick layer of polycrystalline silicon (Poly Si) was grown after patterning on SiN layer with LPCVD. The wafer was patterned again using photo-resist with subsequent etching of Poly-Si with reactive ion etch (RIE) as shown in (c). In step (d), a 750 m thick layer of SiN was deposited again using LPCVD. Patterning and etching was done from top and bottom of the wafer to create fill channels and geometrical shape for the the cantilever to be released as shown in (e). RIE was done from the backside of the wafer to remove Si layer so that we have a suspended structure. KOH etch was used to remove the leftover Poly-Si in the channel in the final step of fabrication. Details about the parameters used for different processes are explained elsewhere [80]. The released devices were diced and then tested by flowing liquids through a microfluidic set up with LDV and by observing their fundamental frequencies. The devices were also heated in a vacuum oven at 300 °C in order to release the residual stress.

3.1.2 Fabrication process for microstring resonators

Doubly clamped beam resonators were fabricated in different sizes from 50 μm to 500 μm . Fabrication process is explained in Figure 3.2

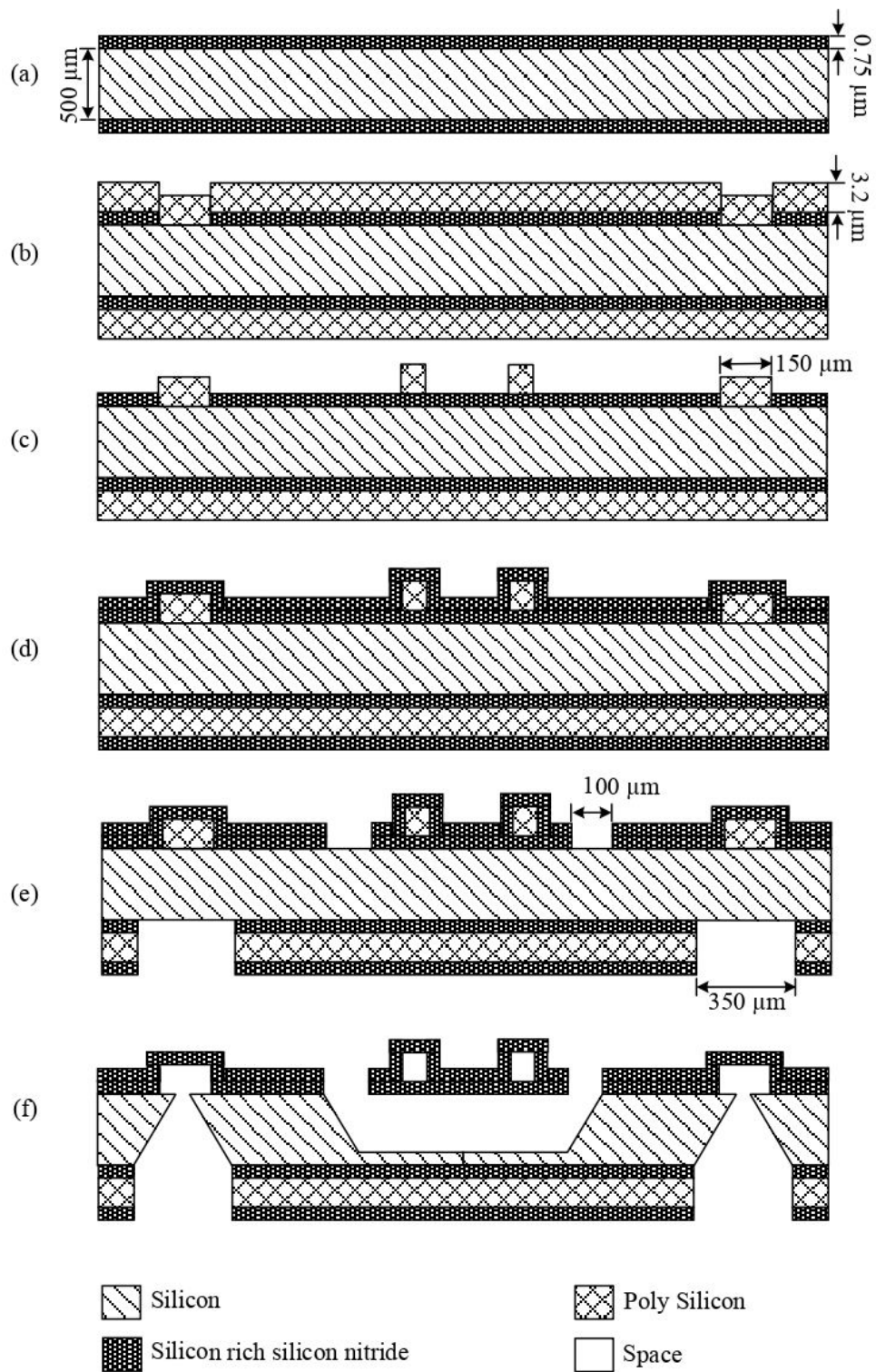


Figure 3.1: Process flow of microfabrication of suspended micro-channel resonators. A six step process started from 500 μm thick silicon wafer with intermediate patterning, etching and a released device shown in step (f).

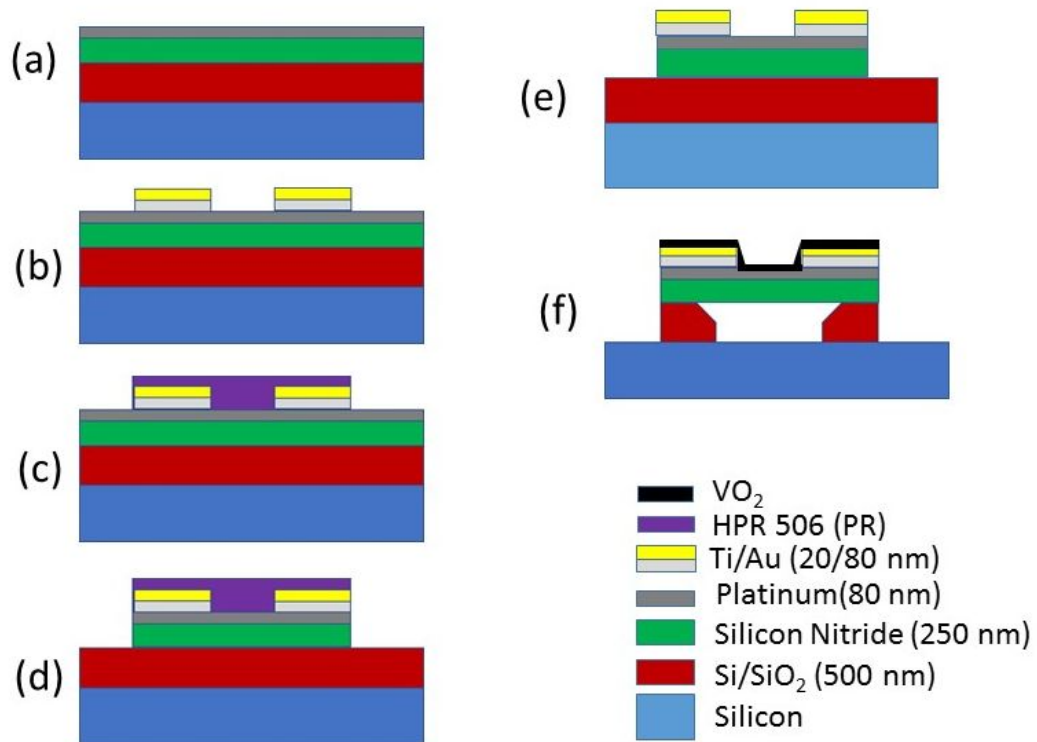


Figure 3.2: Process flow of microfabrication of micro-string resonators for studying phase change material characteristics. The process starts with 1.5 μm thick thermal oxide wafer with various intermediate patterning and etching steps until we get release micro-string resonators for further thin films deposition to be done with Pulsed laser technique.

Fabrication process for micro-string resonators is schematically shown in Figure 3.2. Thermal oxide wafer of thickness $1.5\mu\text{m}$ was piranha cleaned and deposited with 250 nm SiN with LPCVD and 80 nm platinum with sputtering as shown in part (a). T/Au contacts were made with e-beam evaporation technique after patterning with shadow mask. Photo-resist HPR 504 was used to protect the contacts and both Pt and SiN were etched away using RIE (step c-d). Photo-resist was lift off in solution of acetone in step (e). The structure was protected again with photo-resist and Si/SiO₂ top and undercut etch was done with RIE in order to release the strings. Mechanical response of the un-coated strings was measured with LDV. Thin films of VO₂ were deposited and strings were made ready to study the insulator to metallic transition in VO₂ using temperature, electric field and optical power as external excitation.

3.2 Laser Doppler Vibrometer (LDV)

A Laser Doppler Vibrometer (LDV) is a non-contact vibration measurement technique capable of measuring vibrations in pm resolution. The laser beam from the LDV is directed at the surface of interest, and the vibration amplitude and frequency are extracted from the Doppler shift of the reflected laser beam frequency due to the motion of the surface. The output is in the form of voltage generated by movement of reflected light onto the position sensitive diode which is proportional to the intensity of the light and the motion of the target object. This technique is made with two laser beam interferometers which measure the frequency or the phase difference between a reference beam and a test beam. The laser we used was helium-neon with a wavelength of 635 nm and maximum output power of < 1 mW. This Interferometric set up is shown in schematic 3.3.

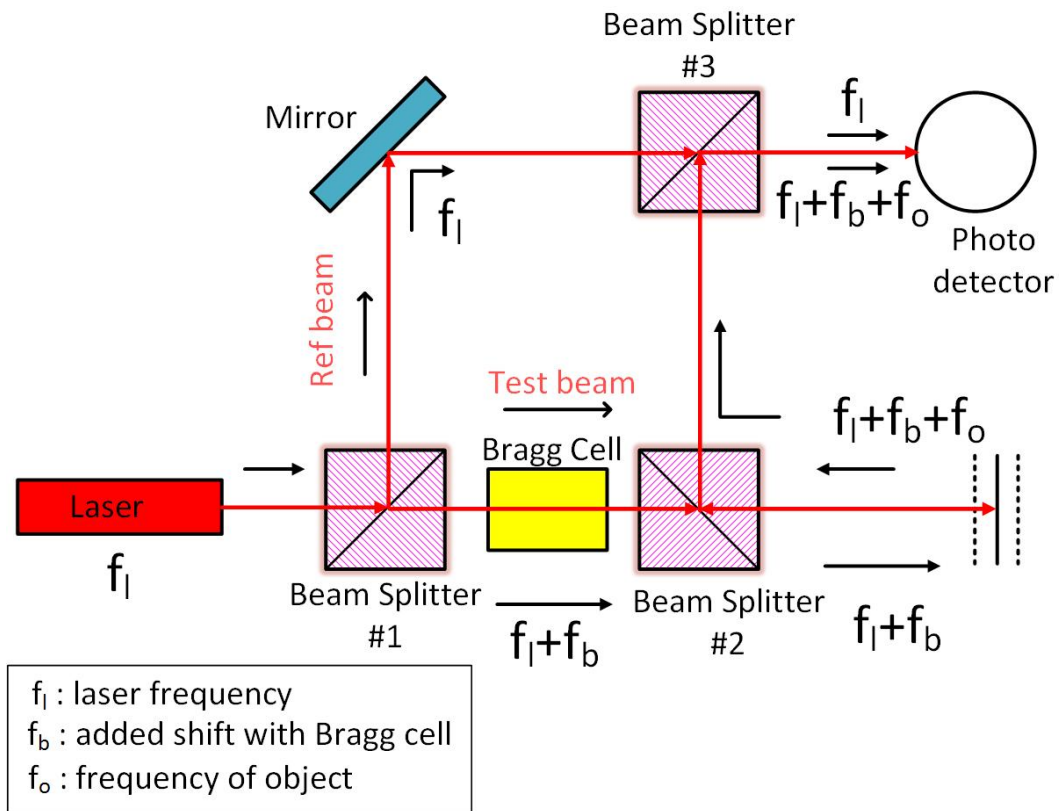


Figure 3.3: A reference beam of laser with frequency f_l interferes with a Bragg modulated beam $f_l + f_b + f_o$ on a position sensitive detector (PSD). The motion of the target object adds a Doppler shift to the beam which then combines with the reference beam to produce interference pattern on the photo detector. The output is a frequency modulated signal which then can be demodulated to extract the velocity vs. time of the vibrating object.

3.2.1 Fundamentals and working mechanism

Doppler effect states that the movement of the source alters the wavelength and the received frequency of wave even though the source frequency and the wave velocity are unchanged. The observed frequency of the wave depends on whether the source is moving away from the observer or moving towards an observer. In case of LDV, light with a known frequency and wavelength is reflected back from a moving object. The rate of change of frequency of the test beam is proportional to the rate of change of position which is the velocity $v(t)$ of the vibrating surface. This relationship is commonly expressed as a formula for the Doppler frequency f_o as;

$$f_o = 2\frac{v}{\lambda} \quad (3.1)$$

where v is the object's velocity and λ is the wavelength of the emitted wave. In order to find out the velocity of the object, the shift in frequency f_o has to be measured at a known value of wavelength. This is measured in LDV by using laser interferometer. If the intensities of the reference and the modulated reflected beam from the the object are I_R and I_M respectively then the total intensity because of optical interference would be;

$$I_T = I_R + I_M + 2\sqrt{I_R I_M} \cos[(2\pi(x_R - x_M)/\lambda)] \quad (3.2)$$

where $x_R - x_M$ is the path difference between two intensities which interfere at photo detector. The total optical intensity is not just the sum of two intensities but an additional interference term is there which makes the total intensity as 4 times higher if the the path difference is integer multiple of the light wavelength. This corresponds to a bright fringe in the interference pattern on photo detector. Working mechanism of LDV is explained in Figure 3.3. The beam of laser with frequency f_l is split by a beam splitter 1

into a reference and a test beam. The test beam passes through a Bragg cell which typically shifts the frequency by 40 MHz. After adding this modulation in the frequency, a second beam splitter allows the part of the light to fall on the moving object and the reflected beam from the object has an additional component in the light frequency which is because of Doppler shift (motion of the object causes a change in frequency). Since the optical path length of the reference beam (x_R) is constant, a movement of the object causes a change in optical path length x_M which will generate bright/dark pattern on the photo detector. This beam combines with reference beam with frequency f_l at a third beam splitter and creates an interference on to the photo-detector. The signal on photo-detector is in the form of voltage which is de-convoluted to get the frequency and amplitude of vibration of the moving body. One complete light / dark cycle on the detector corresponds to an object displacement of exactly half of the wavelength of the light used.

The change in optical path length per unit time because of the motion of the object under investigation correlates with the Doppler's shift of the beam. This leads to modulation frequency of interference pattern on photo diode being related to the velocity of the object. Since the object moving away from the laser beam generates the same interference pattern as object moving towards the beam, the direction of motion of the object can be determined by using a Bragg cell which will add a constant frequency in the test beam which is around 40 MHz. The modulation frequency will increase if the object moves towards the interferometer and decreases if the object moves away from it. This makes it possible to not only measure the magnitude of the velocity but also the direction of motion of the vibrating object.

3.2.2 Integrated instrumentation with LDV

In order to investigate the phase transitions in both liquids and solids with various external excitation mechanisms like electric field, temperature and

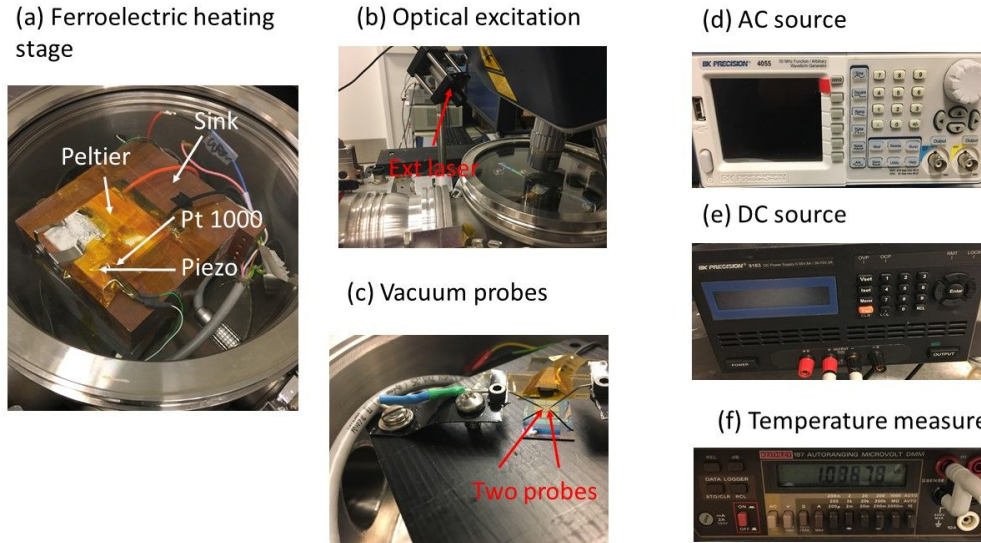


Figure 3.4: Platforms developed for carrying thermal, electrical and optical excitation and measurements in resonating systems used for probing phase transitions in liquids and solids. Ferroelectric heating stage used a peltier element attached with a big chunk of copper with thermal paste with temperature sensor Pt 1000 fixed on top of it. A piezo actuator is used to drive the resonator and whole system was put inside the vacuum chamber for detecting mechanical vibrations of both strings and cantilevers. In (b) and external optical excitation was used in conjunction with the internal LDV laser which itself can have a variable power. In (c), two contacts vacuum probe station was developed to probe electric field assisted insulator to metal transition in VO_2 strings. Function generator shown in (d), DC source shown in (e) and Micro-volt meter shown in (f) were used to provide ac signal, DC supply to peltier element and measure the resistance of Pt 1000 sensor respectively.

optical power, we developed some auxiliary instrumentation which was integrated with LDV to carry out the excite-response measurements. Three main platforms were developed which are shown in Figure 3.4. Ferroelectric heating stage was developed to provide controlled heating to the resonators while accurately measuring temperature with Pt 100 sensor mounted on top of the plate. The plate was thermally anchored to a big piece of copper which would act as a thermal sink. Two small brackets made bent and made firmly contacted with the surface of peltier were used to hold the micro-chips containing devices. A piezo actuator was mounted firmly very close to the

resonator in order to effectively transfer acoustic energy into the resonating structure. Temperature was measured using Keithley 197 micro-voltmeter shown in (f).

In order to measure the optical response of the VO₂ coated resonator, we used an external diode laser placed in laser holder with laser falling at 45° on the sample. The effective power of the external laser was also measured using the same conditions by putting ThorLabs PM100A photo detector. The laser spot was very large as compare to the width of the resonator so we centered the laser spot first and then fixed the laser holder. Three different types of external lasers were used in order to see the effect of wavelength on the behavior of resonator. The input power of LDV was also measured using the same photo-detector for all seven different power levels of the laser.

Part (c) is a custom built vacuum probe station. Two probes were connected with pieces by making a groove on the metal pieces and firmly affixing one side of the probes by using screws. The end of the probes was connected to a male-female connector assembly from where it was connected with the function generator outside of the vacuum chamber. The measuring ends were bent and controlled via a micro-manipulator to move laterally and vertically. The sample was placed under these probes and finite resistance measurement was done in order to make sure the contacts are made. Both AC and DC signals were supplied via these probes and mechanical response was measured with LDV as a function of the electric field.

3.3 Pulsed laser deposition (PLD)

Pulsed laser deposition (PLD) is a versatile physical vapor deposition method which can deposit high quality thin films of most of the materials. The technique uses a pulsed laser to ablate the target material and stoichiometrically deposits the target material onto the substrate either using an inert or re-

active environment. Each laser pulse evaporates a small amount of target material and creates a plasma (gas of ions and electrons) and the amount of plasma or ablated material depends on material and energy of the laser. This plasma which often forms in a cone like shape, can be directed towards a substrate which is placed perpendicular to the direction of the motion of the plasma. This plume is dependent on vacuum level and nature of gas in the chamber. The substrate is often tightly clamped on a heating stage connected to a temperature controller enabling a control on deposition temperature of the substrate. Once the target material has reached the substrate, film growth is dictated by not only the ablation parameters, but additionally by the properties of the substrate, the process parameters, and the interaction between the deposited material and substrate. A schematic of the process is shown below in Figure 3.5

Historically, this techniques has been explored for thin films deposition by evaporation since 1960's but it became considerably noticed in late 1980's when Dijkkamp et al. demonstrated direct deposition of superconducting YBCO thin films onto SrTiO₃ and Al₂O₃ substrates [81]. This demonstration of stoichiometrically transferring of complex oxides directly from target to substrate, without sacrificing any of the target materials properties gained widespread notice from the scientific community. One of the key benefit of this technique is its ability to transfer complex oxides directly from target to substrate without compromising the integrity of the material. A nanoseconds pulse of UV laser is focused on a small spot at the target material in order to increase the energy density and absorption of the pulse into the material [82]. It is important that the target material must have a high optical absorption coefficient for a specific wavelength of the laser without which the laser may penetrate deep into the material with reduced chances of vapourization and hence a bad quality of resultant plasma and hence a bad quality of deposited film. With the right choice of conditions, the resultant plasma is directed

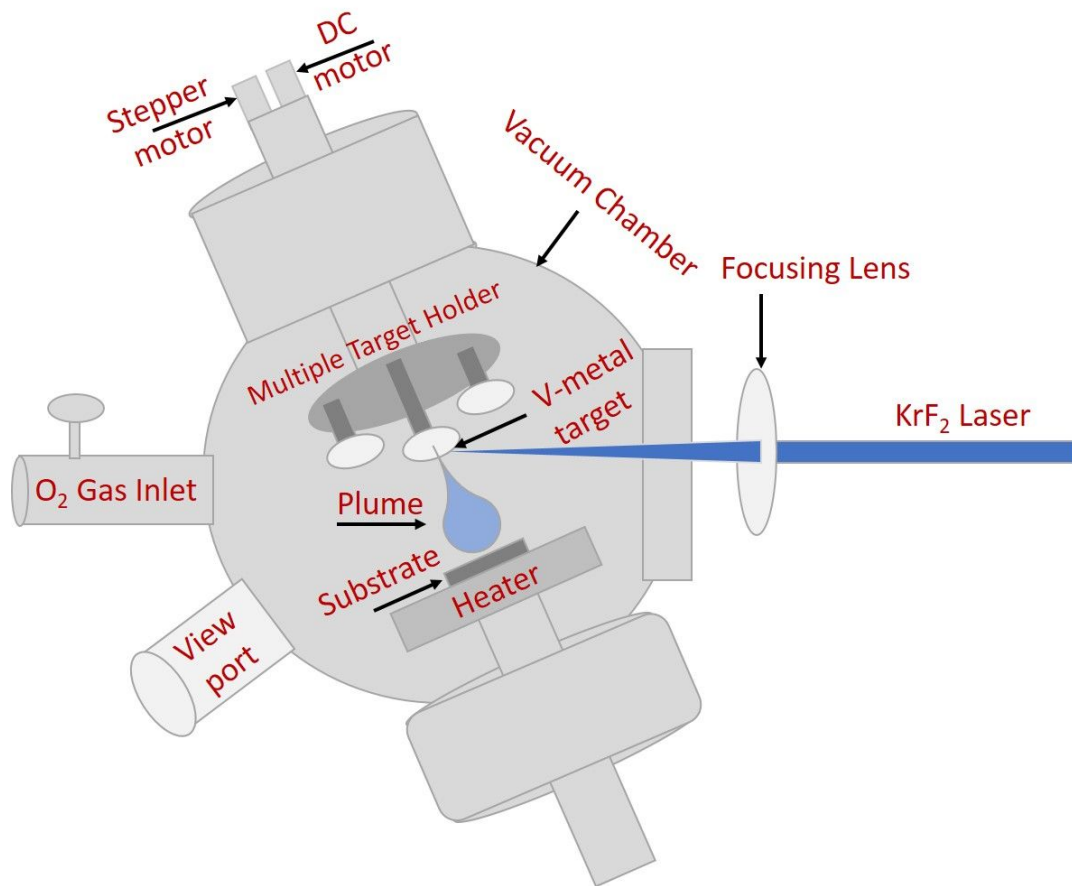


Figure 3.5: Graphical representation of the PLD deposition system. The laser enters the vacuum chamber through a glass window and hits the rotating target. The plasma plume is ejected normal to the surface of the target and is directed towards the heated substrate stage.

towards the substrate where it condenses and forms as solid film.

Excimer laser are the most popular laser for PLD systems. The name excimer is a combination of the words "excited" and "dimer" which refers to the operation of the laser itself. These "dimers" are in a dissociative ground state, and only when ionized into an excited state do they form any bonds. Lasing in an excimer molecule occurs because of bound (associative) excitation with a repulsive (dissociative) ground state. Noble gases such as xenon and krypton are highly inert and do not often form chemical compounds. However, they can be excited (with electrical discharge or high-energy electron beams), which can cause them to form temporary bound molecules with themselves (excimer) or with halogens (exciplex) such as fluorine and chlorine. The excited compound can release its excess energy by undergoing spontaneous or stimulated emission, resulting in a strongly repulsive ground state molecule which very quickly (on the order of a picosecond) dissociates back into two unbound atoms. This process forms the population inversion which is a pre-condition for lasing. In our system we use a krypton fluoride excimer laser (KrF) where the molecule KrF absorbs energy from a source and causes krypton gas to react with fluorine gas producing the exciplex krypton fluoride which temporarily gets into excited state. This excited state again goes into spontaneous or stimulated emission which will reduce its energy to a metastable state which is a highly repulsive ground state. This ground state quickly dissociates into unbound atoms again. The process results into an exciplex laser with its wavelength near in the UV portion of the spectrum [83]. Our PLD system has a deposition chamber manufactured by Excel Instruments, Mumbai, India with laser source of a KrF ($\lambda=248$ nm) excimer (Coherent, GmbH). The pulse duration can be as small as 20 ns and maximum laser energy and repetition rate could be as high as 700 mJ and 50 Hz respectively. There are six targets which can hold six samples inside the deposition chamber. The substrate temperature can be accurately set and measured up

to 850 °C. Turbo and rotary pumps are attached to the chamber in order to achieve high vacuum. The pressure is measured with a high vacuum pirani gauge and an ultra high vacuum cold cathode gauge which are mounted with the chamber. The rotation of the targets inside the chamber is done with a motorized interlock controlled by an electronic module. Gas flow rate is measured with a mass flow controller.

3.3.1 Deposition mechanism on substrate

Film growth process starts with condensation of ablated products on to the sample mounted with heating stage. The mechanism of growth of film is dependent on various factors including but not limited to temperature, gas pressure, base vacuum, substrate and target materials, laser energy and frequency of pulses and distance of substrate from the target material. The shape and structure of the film is governed by two major mechanisms which are the mode of growth and grain structure geometry. Depending on many parameters involving some degrees of probabilities, one path the deposition can choose is layer by layer structural formation which is called Frank-van der Merwe (FM) type. Another possibility is island formation which is known as Volmer-Weber (VW) type of growth. There is a strong probability of formation of films via a hybrid route where a mixture of island and layer by layer mechanism of growth will occur. This combined formation scheme is called Stranski-Krastanov growth (SK) [84]. The growth mechanism is usually governed by thermodynamics of ad atoms and the substrate. If the ad atoms like to interact with each other than the surface of the sample then we can expect some island formation which is VW type as explained before. If the atoms like the surface more than each other, then the probability of formation of layer by layer structure is high. This growth mechanism also favors the monolayer formation. In SK growth scheme, initially the growth resembles to FM type but after a few monolayers it can switch to VW growth.

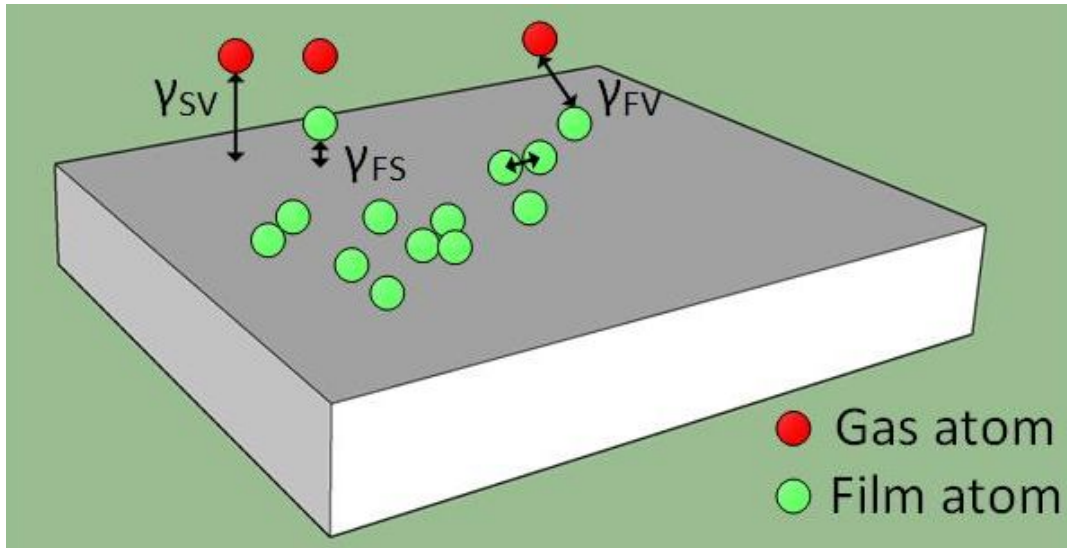


Figure 3.6: There are three different interfacial energies involved in the PLD film deposition process. Depending on relative magnitude of free energy at each interface, a VW or FM growth mechanism will occur.

The deposition of any thin film process is controlled by free energies of the interacting interfaces. If the free energy of interface is denoted by γ , the interface between substrate and add atoms by γ_{SV} , film to substrate by γ_{FS} , and film to vapor (add atoms to be deposited) by γ_{FV} , then depending on arrangement of these energies, VW growth or FM growth mechanisms are possible. Energies and atoms are depicted in Figure 3.6. If

$$\gamma_{SV} < \gamma_{FV} + \gamma_{FS} \quad (3.3)$$

then it is likely that VW growth will occur as the surface energy is minimized by maintaining as little contact as possible between the film and substrate. If the add layer has a lower surface energy than the substrate then FM growth will occur as shown in eq. 3.4

$$\gamma_{SV} \geq \gamma_{FV} + \gamma_{FS} \quad (3.4)$$

Depending which route the grain growth takes, the film deposited will effect electronic, optical and thermal properties which we will discuss in details chapters 5, 6, 7 and 8.

In future chapters we will see the influence of pressure and flow rate on quality of VO₂ thin films on SiO₂ substrates and use an optimize condition to do deposition on SiN micro-strings.

3.4 X-ray diffraction

XRD is a technique used to determine the atomic (or molecular) structure of a crystalline material by measuring the intensity of diffracted X-rays. It is one of the most employed technique in materials which can accurately provide properties such as structure, plane spacing, crystal orientation, and interfacial stress/strain formed in the crystals as result of deposition. The sample is placed on a stage with a source which produces x-ray photons and sends them to the surface which exchange energy and momentum with the lattice and a detector which can move at various speeds and angles and scans the diffracted beam of photons. Depending on the crystallinity of the sample and orientation of crystals, valuable information about the crystals is obtained with Bragg's diffraction peaks. It is a powerful technique because the wavelength of X-rays is comparable to the atomic spacing.

The Bragg equation, shown in eq. 3.5, gives the condition for constructive interference as described above.

$$n\lambda = 2d\sin(\theta) \quad (3.5)$$

Here, n is an integer, λ in the X-ray wavelength (Å), d is the spacing between lattice planes (Å), and θ is the angle which results in maximum intensity of the diffracted beam.

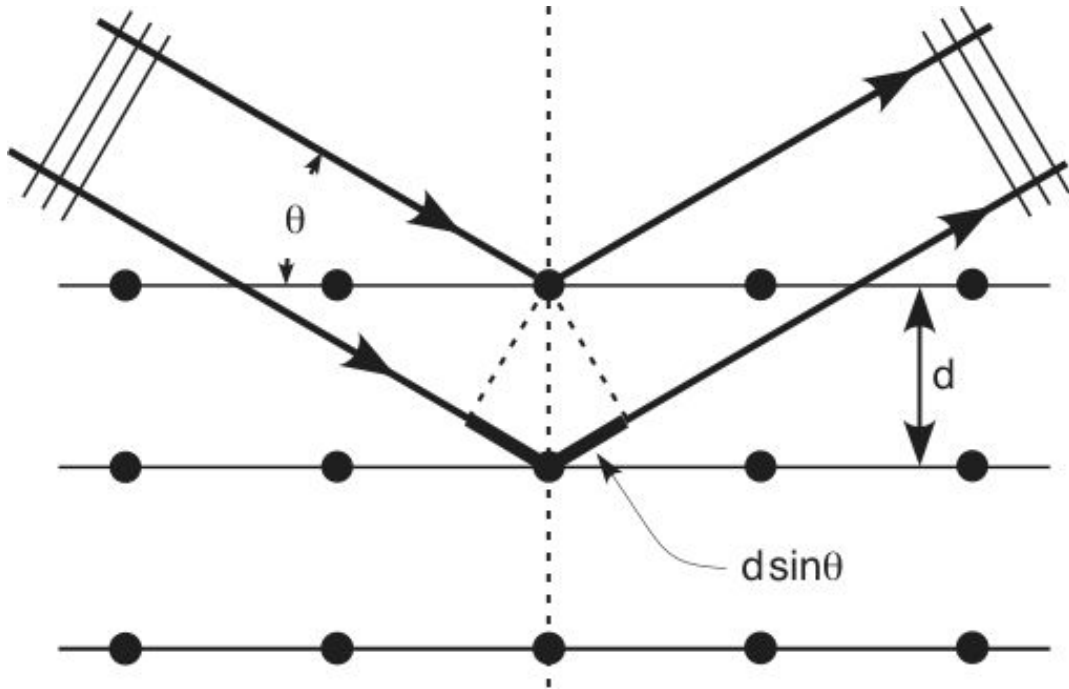


Figure 3.7: Schematic representation of Bragg diffraction. Constructive interference occurs if the path length difference between the incoming waves is equal to an integer multiple of their wavelength.

Before depositing the VO_2 thin film onto the micro-resonators, we optimized the deposition conditions with respect to oxygen flow rate in the PLD. We performed XRD studies in order to see the phase formation and quality of the films dependent on flow rate. Using the optimized conditions, thin films were deposited onto the resonators, SiO_2 , TiO_2 and sapphire.

For our studies, XRD was performed using a Rigaku Ultima IV diffractometer using a $\text{Cu K}\alpha$ X-ray source and a scintillation counter detector. We used two different scanning geometries, the conventional Bragg-Brentano (θ - 2θ) and a grazing angle mode. Thin films deposited via PLD technique will be characterized with the grazing angle mode of detection as it eliminates the appearance of substrate reflections. In this mode the incident X-rays are fixed at a constant angle (mostly at 0.5° for our work unless otherwise specified) and the detector is scanned to collect the diffracted beam from the crystal. Such a small grazing angle will make the incident beam almost parallel to

the thin film deposited onto the substrate, a larger amount of reflection will be coming from the film itself.

In some cases, simply scanning 2θ was not sufficient, and additional scan configurations were needed. For VO_2 , several reflections in the monoclinic phases have multiple planes at the same 2θ value, which need to be distinguished. In this case an off-axis ψ scan is performed, where the detector is fixed at a reference 2θ value and rotated out of plane to a ψ value corresponding to the angle between the plane under question and reference plane and the stage is then rotated the desired amount. If the plane under question is in fact the correct plane, reflections indicative of the symmetry of said plane will appear on the ϕ scan. If it is not the correct plane, no reflections should appear.

3.5 Probe station

We used Signatone S-1160 probe station for carrying out electrical resistivity and IV measurements. Four probe contacts were used to measure the sheet resistance in case of thin films and two probes were used to measure resistance of micro-string resonators. The sample stage was connected with a Thermo Scientific ThermoChill 2 chiller for controlling the temperature of the stage. For measurement system, two channel Keithley source meter 2602B was used to source current and measure voltage or vice a versa. Many software packages were used for interfacing with the hardware including Lab-view, visual basic and Keithley kickstart software.

The S-1160 accommodates both stereo zoom and high magnification microscopes and CCD camera mounting. A very smooth X-Y-Z stage and microscope movement with four micropositioners made this system very accurate for handling samples while making contacts and looking under microscope. The system was equipped with coaxial and triaxial cables which could easy

allow pA and fA current ranges.

3.6 Helium ion microscopy

Scanning helium ion microscopy (S-HIM) was used to analyze the insulating samples without metal coating. The operation of this microscope is similar to that of SEM but it uses positively charge helium ions instead of electrons for its beam directed towards the surface to be analyzed. This is a very powerful technique which offers many advantages over the conventional SEM. It is possible to take high resolution images of insulating surfaces without depositing any conductive layer on the sample. The depth of field is very high because of doubly charge massive helium ions as compare to electrons. Because of large momentum it is easy for He^+ ions to avoid deflection from electromagnetic coils leading to a more focused beam. A secondary electron gun is used sometime in order to neutralize the positive charge carriers build up on the surfaces of highly insulating materials. Secondary electron gun will bombard electrons on the surface and will provide a better pathway for helium ions to image it. Focused ion beam milling can also be used for insitu sample preparation and image the interface at high resolution. We used this technique for imaging VO_2 thin films and VO_2 coated micro-resonators.

3.7 Atomic force microscopy

Atomic force microscopy (AFM) is a powerful characterization tool used to understand many properties of materials. The basic principle is a micro-cantilever with an ultra thin tip which can approach the surface of interest or gets in contact with it. Depending on the nature of the forces involved between the tip and the surface, the cantilever's dynamic or static response changes which is related to the features of the surface. There are three different

modes of operation which can be useful in analyzing materials properties. The contact mode, tapping mode and non contact mode. In the contact mode, the cantilever is in contact with the surface and dragged across a well focused and sized region of interest providing information about the surface topography. Features like surface roughness, film thickness etc. will be measured using this mode. A laser falling at the tip of the cantilever will measure the bending of the cantilever which can be associated with the topographic features of the surface.

In non contact mode, the cantilever is set to oscillate very close to the surface but not touching it. In contrast to making a physical contact, here the tip and the sample interaction is measured by mechanical behavior change because of van der-Waals interactions between the tip and the surface of interest. A variant of this mode is kelvin probe force microscopy where the work function of the surface can be observed at atomic or molecular scale. We will use this technique to map out the work function of VO₂ coated substrates. The details about KPFM mode utilization for VO₂ films will be discussed in later chapters.

The third mode offers a a combination of first and second mode. In tapping mode, a sample is imaged while the cantilever is brought in contact with the surface and lifted back to a certain height from the surface. This contact and lift can be tuned by changing the tapping frequency. The cantilever is lifted to a height of roughly ~50 nm before it is brought back to touch the surface. The oscillating frequency of the cantilever is set near to its first resonance frequency. The energy of the cantilever gets dissipated during the tapping and interaction process and that lost in energy is related to the interaction forces between tip and surface.

3.8 Differential scanning calorimeter (DSC)

Q 2000 DSC system by TA instruments was used to perform thermal analysis of the polymers. DSC is a thermal analysis technique in which the heat flow to the sample is monitored against time or temperature while the temperature of the sample is controlled in an inert environment. In practice, a reference which is identical in size and materials characteristics to the test pan is placed very close to the sample or test pan. The reference sample should have a well-defined heat capacity over the range of temperatures to be scanned. The technique was developed by E. S. Watson and M. J. O'Neill in 1962 [85]. The principle of operation of this technique is heat flow for endothermic or exothermic reactions which will decide the type of phase transition in the material. We would use PMMA and PLA samples for studying the glass transition, crystallization and melting phenomena for comparing our results with the ones we obtained using suspended micro-channel resonators.

3.9 X-ray photoelectron spectroscopy (XPS)

X-ray photoelectron spectroscopy (XPS) is a spectroscopic technique which is useful in quantitative analysis of elemental composition at the parts per thousand range, chemical state and electronic state of the elements that exist within a material. The instrument can probe up to 20 nm depth to find out what elements are present in the film and how are those bounded to others meaning in a metal oxide film whether the metal is in +1 or +2 valance state. The principle of operation is based on measuring the kinetic energy and density of electrons which come out of the surface being bombarded with high energy X-rays. This measurement needs ultra high vacuum $< 10^{-9}$ mbar. Knowing the energy of incident photons, kinetic energy of electrons and the work function of the material, the binding energy of electron can be calculated

with the equation [86];

$$E_{binding} = E_{photon} - (E_{kinetic} + \phi) \quad (3.6)$$

XPS Spectrometer (Kratos AXIS Ultra) at Nano fab facility at University of Alberta was utilized to perform the spectral studies on optimization of thin films deposition process. Several VO₂ films were deposited under same pressure and temperature conditions and only changing the oxygen flow rate. The shift in the peak positions of XPS spectra of oxygen rich and oxygen poor samples was studied as a function of oxygen flow rate. The detailed analysis about XPS on VO₂ will be discussed in later chapters. It is worth mentioning that the author did not used the instrument himself instead samples were submitted for analysis at the nano-fab facility.

Chapter 4

Probing phase transitions in polymeric liquids with MEMS

4.1 Abstract

Microchannel cantilevers are an emerging platform for physical characterization of materials at the picogram level. Here we report on detecting multiple thermal transitions in picogram amounts of two well-known polymers, semicrystalline poly(L-lactide) (PLA) and amorphous poly(methylmethacrylate) (PMMA), using this platform. The polymer samples, when loaded inside the cantilever, affect its resonance frequency due to changes in its total mass and stiffness. When taken through a thermal cycle, the resonance response of the cantilever further changes due to multiple thermal transitions of the samples. Continuous monitoring of the resonance frequency provides information about β -transition (T_β), glass transition (T_g), crystallization (T_c), and melting (T_m) of the confined polymer samples. The measured T_g , T_c for PLA were $\sim 60, 78$, and 154°C , respectively, while the T_g and T_β for PMMA were 48 and 100°C , respectively. These results are in an agreement with the data obtained from differential scanning calorimetry (DSC). Because of its high sensitivity, this technique is capable of detecting the weaker β -transitions that cannot be

observed with conventional DSC.

4.2 Introduction

Polymers are versatile materials with well-established applications in the pharmaceutical [32], manufacturing [33], chemical [34], microelectronics [87] and food industries [36].

Recently, various researchers have reported the use of nanoscale amounts of polymers for applications such as non-volatile memory [37], energy storage [38], and biomimetics [39]. Such applications require highly precise measurements of stability, durability, and purity of a polymer. Most of these characteristics can be investigated using thermal properties of polymers such as glass transition (T_g), crystallization (T_c), enthalpy relaxation, and melting (T_m) [38]-[40]. In addition to these well-known transitions, certain polymers may also exhibit a β -relaxation/transition, which is due to localized movements in the main chain or the movement of a very large side chain[41]. For large scale applications, most of these transitions can be probed with conventional techniques such as differential scanning calorimetry (DSC)[42],[43],[44], dynamic mechanical analysis (DMA) [45], thermomechanical analysis (dilatometry) [46], and dielectric spectroscopy (DES) [47]. Although well established, these techniques are unsuitable for characterization of sub microgram levels of polymers due to the restrictions on the sample size (~ 5 – 10 mg) and dimensions. Therefore, there is an emerging need to develop techniques capable of characterizing materials at the nanoscale. In order to fulfill this requirement, various sensors have been proposed to measure the thermal and mechanical properties of polymers at sub microgram levels. Microscale resonators is one such platform, which offers advantages such as; no shape dependence, high sensitivity, very small sample mass (nano to microgram), wide dynamic range of measurement, and faster operation [48],[49],[50],[88]. Micro resonators,

such as microstrings and microcantilevers, have been previously employed for thermal analysis (of small masses) of polymers [48],[49],[56],[57]. Both of these techniques require special spray coating or ink jet printing to deposit nanograms of sample [58]. Another challenge (when using microstrings or microcantilevers) is sublimation of the sample during heating. In order to overcome these difficulties, we have developed a microchannel cantilever consisting of microfluidic channel integrated on top of the cantilever. With the volume of the microchannel ~ 50 pL, the resonance frequency of the cantilever is ~ 150 kHz while its quality factor lies in the order of six to eight thousand. These values ensure high resolution in detecting any changes in the resonance frequency. Previously, this principle and the device have been successfully employed to detect sub attogram mass, and the density and viscosity of picoliters of confined liquids and thermal sensor for binary liquid mixture [59],[62],[61]. Without any complicated protocols or equipment, the polymer samples can be loaded into the microchannel using melt infiltration. In order to detect thermal transitions, the polymer-filled cantilever is heated under high vacuum. Although the cantilever is operated at low pressure ($\sim 5 \times 10^{-6}$ mbar), the polymer is enclosed within the microchannel which keeps the sample at atmospheric pressure. The incorporation of this microchannel enables the measurement of all thermal transitions up to (and including) the melting point. As a result, multiple heating cycles can be used to probe the transitions of the material in order to study its reversibility/hysteresis. To test the cantilever systematically (as a platform for thermal analysis), two different polymers were chosen as a case study such as biodegradable, semi-crystalline poly (l-lactide) (PLA), and amorphous poly(methylmethacrylate) (PMMA). The aim of this study was to use a miniature, robust, and sensitive platform to obtain accurate information about the thermal events occurring in the polymers. Thermal characteristics such as T_g , T_c , T_m and T_β are investigated and the results are compared to those obtained from conventional

DSC.

4.3 Experimental

Poly(L-lactide) or PLA ($M_n = 50,000$, unknown polydispersity) and poly(methylmethacrylate) or PMMA ($M_w = 120,000$) were used as test materials due to their well-known thermal transitions. The densities of the PLA and the PMMA samples used in all experiments are 1.3 g cm^{-3} and 1.2 g cm^{-3} respectively [89]. The microchannel cantilevers were fabricated using conventional top-down microfabrication techniques, as described in our previous chapter in fabrication process. The dimensions of the cantilevers were $200 \mu\text{m}$ (length) \times $20 \mu\text{m}$ (width) \times $3 \mu\text{m}$ (microchannel height) as shown in Fig. 4.1.

The calculated mass of the cantilevers were 14.6 pg (considering ρ of $\text{Si}_3\text{N}_4 = 3.44 \text{ g cm}^{-3}$). Prior to loading the polymer samples, each cantilever was cleaned with piranha (in order to remove organic contaminants) and heated on a hot plate at $200 \text{ }^\circ\text{C}$ for two hours to drive out any residual moisture. The cantilevers were filled with the polymer samples through a melt infiltration technique, where a small amount of the samples was placed on inlets (located on backside on the chip). The chips were heated on a hot plate to $150\text{--}170 \text{ }^\circ\text{C}$. At the melting temperature, due to strong capillary forces, the polymer is able to flow inside the microchannel.

Fig. 4.1a shows a schematic of the microchannel cantilever based thermal analysis platform used in this study. In order to apply a controlled thermal cycle, the cantilever was firmly placed on top of a Peltier element, and the temperature was continuously monitored by a Pt-1000 resistance temperature detector (RTD) mounted on top of the chip. Temperature was logged in real time by monitoring the RTD's resistance using a Keithley 197 multimeter interfaced with LabView software. The cantilever was heated from room temperature to $180 \text{ }^\circ\text{C}$ at a heating rate of $4 \text{ }^\circ\text{C min}^{-1}$. In order to enhance

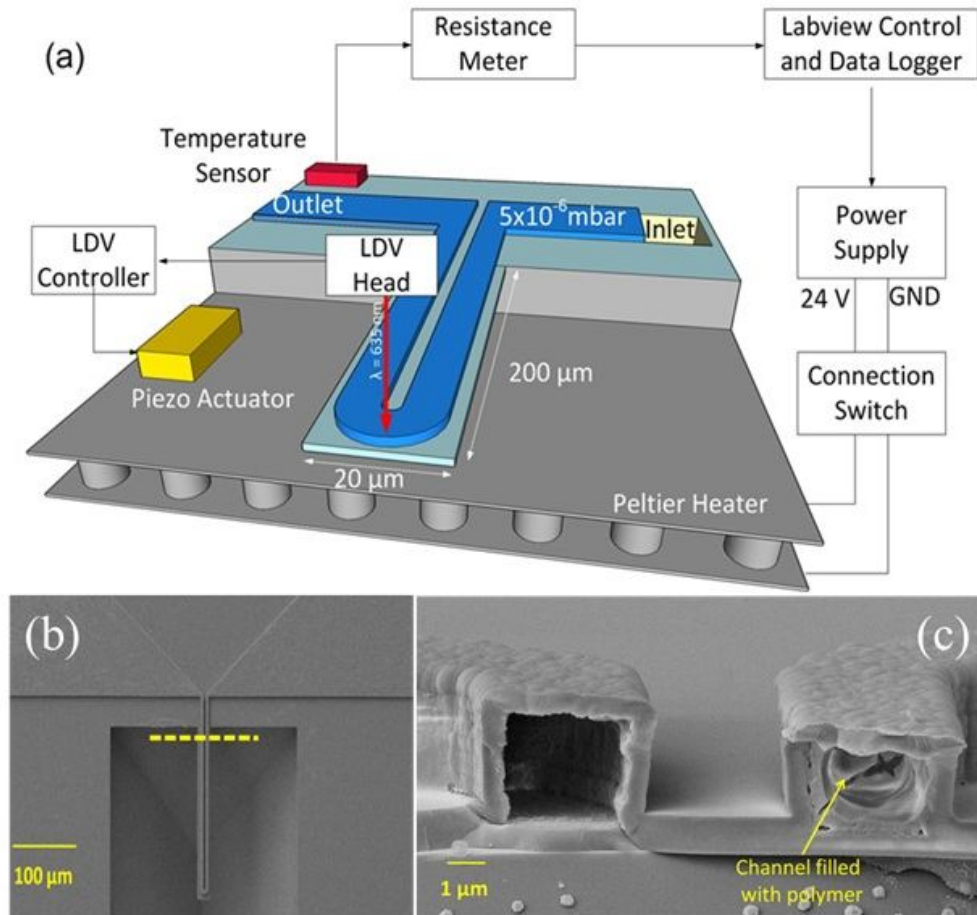


Figure 4.1: Figure1. (a) Experimental setup to characterize picograms of polymers. (b) SEM of the top view of the microchannel cantilever. Yellow dash line in shows from where the cantilever was cut to show Fig.(c). (c) Shows SEM of the cross-section of half-filled cantilever which depicts the unfilled and filled channel.

the signal to noise ratio (SNR), the cantilever was mechanically excited by an external piezo actuator. The resonance frequency was measured optically using a laser Doppler vibrometer (LDV, Polytec, USA) and was monitored continuously during the experiments. As the polymer samples are viscous, a cantilever cannot be effectively flushed and be used for another sample. Therefore, to avoid cross contamination, two similar cantilevers were used to characterize the two polymer samples. Prior to loading each sample, the empty cantilevers were characterized to determine their resonance frequency and phase. In an effort to enhance the quality factor (and thus the sensitivity) of the cantilevers, all the experiments were carried out at a vacuum level of $\sim 10^{-6}$ mbar. SEM of the top view of the cantilever is shown in Fig. 4.1b. A cross sectional SEM view of the channel (showing a filled and an empty channel) is shown in Fig. 4.1c. For reference measurements, the polymers were characterized using DSC (TAQ100) with 5–7 mg of sample, with a heating rate of $10\text{ }^{\circ}\text{C min}^{-1}$.

4.4 Results and discussion

Though the cantilever has a microchannel fabricated on the top, it follows the same dynamics of vibration as a plain cantilever. The fundamental resonance frequency, $f_c(T_0)$, of the cantilever at temperature, T_0 , is given by eq. 4.1, where k_c and m_c are the cantilever's stiffness and mass respectively [90].

$$f_c(T) |_{T=T_0} = \frac{1}{2\pi} \sqrt{\frac{k_c}{m_c}} \quad (4.1)$$

Filling the cantilever with a polymer changes the stiffness and the mass of the cantilever, causing a shift in its resonance frequency. If the polymer stiffness and mass are indicated as k_p and m_p , respectively then by assuming a parallel spring-mass model, the effective resonance frequency $f_{c+p}(T_0)$ of

the polymer-filled cantilever would follow eq. 4.2.

$$f_{c+p}(T) |_{T=T_0} = \frac{1}{2\pi} \sqrt{\frac{k_c + k_p}{m_c + m_p}} \quad (4.2)$$

Since $\frac{k_c}{m_c} > \frac{k_c + k_p}{m_c + m_p}$, it is quite clear that $f_c(T_0) > f_{c+p}(T_0)$. As compared to the structural material (silicon nitride) of the cantilever, the polymer exhibits a higher change in its stiffness due to heating. Therefore, as the temperature increases, the change in k_p dominates over k_c , due to significant changes in the elastic modulus of the polymer. Hence, by monitoring $f_{c+p}(T)$, the transitions of the polymer can be determined. From eqn. 4.3, it is evident that k_p can be determined by monitoring the resonance frequency of a cantilever before and after loading the polymer

$$k_p(T) = k_c \left[\left(\frac{f_{c+p}(T)}{f_c(T) |_{T=T_0}} \right)^2 C^2 - 1 \right] \quad (4.3)$$

where $C = \left(1 + \frac{m_p}{m_c} \right)^{-\frac{1}{2}}$. In this case m_c , m_{PLA} , and m_{PMMA} are calculated as 14.6, 6.24, and 2.8 pg respectively. Since the samples are confined inside the microchannel, there is no mass loss due to sublimation. Cantilevers with similar mechanical properties were used in order to perform the thermal analyses of the polymers. Prior to loading the polymers, resonance frequency and phase response of the empty cantilevers were recorded (shown in Fig. 4.2a and b). The quality factor of the empty cantilevers was found to be ~ 6000 . However, after loading the polymers into the microchannel, the resonance frequency of the cantilevers decreased by 14–16 kHz and the quality factor reduced to $\sim 20\%$ of their original values. These changes ensure that the polymer successfully entered the cantilever. Unlike a cantilever (placed inside a liquid), which experiences a large viscous damping, a microchannel cantilever loaded with a viscous polymer maintains a quality factor well

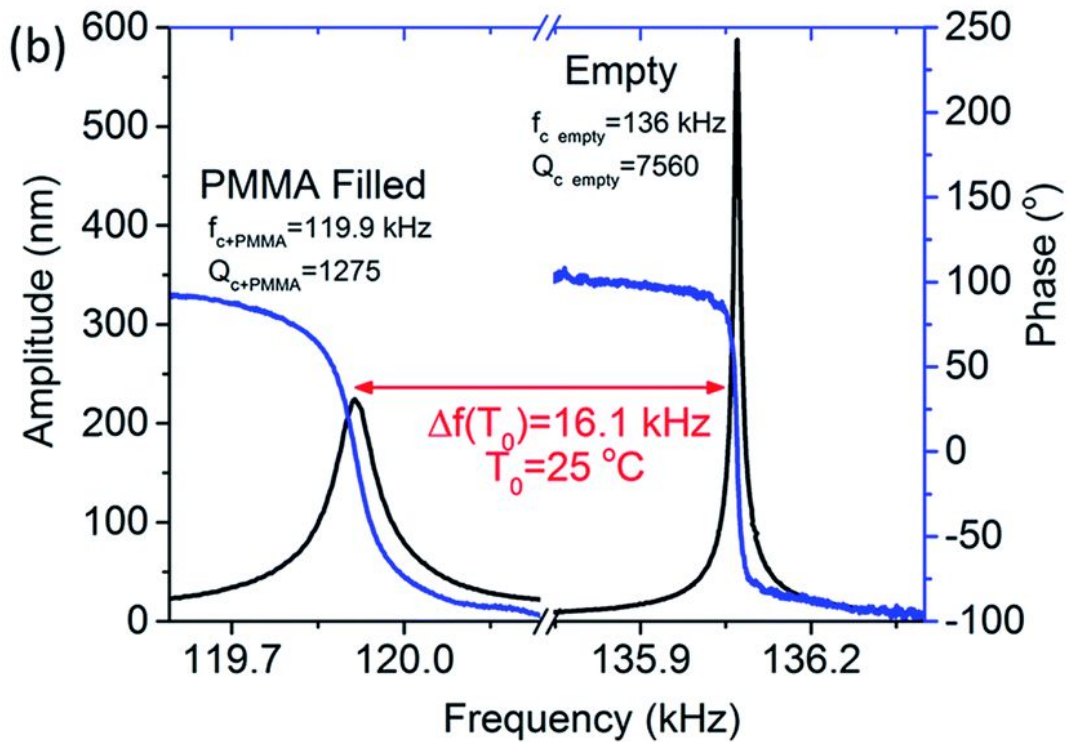
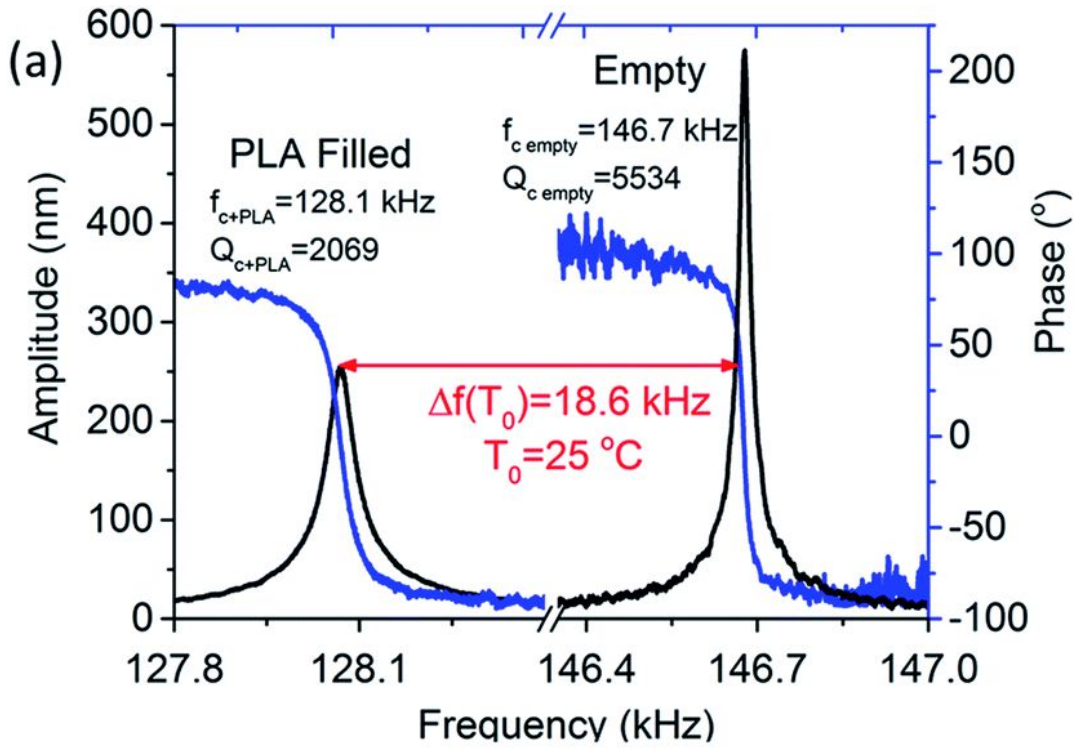


Figure 4.2: Figure2. (a) Resonance frequency and phase of empty vs PL filled cantilever.(b) resonance frequency and phase of empty and PMMA filled cantilever.

above 1000.

In order to accurately perform experiments, stability of the device temperature and its effect on the resonance frequency were first quantified by heating the cantilever in a step-wise manner while simultaneously recording the temperature and frequency response. A 4 °C step was applied to each cantilever and their corresponding temperature and frequency responses were recorded as shown in Fig. 4.3. Temperature stability was achieved after ~ 60 s. However, as shown in 4.3a, the resonance frequency of the cantilever is material dependent and show stabilization times of 100, 150, and 270 s for the empty (τ_{empty}), PLA (τ_{c+PLA}), and PMMA (τ_{c+PMMA}) filled cantilevers, respectively. Therefore, for subsequent measurements we have used 100, 180 and 300 s as stabilization times for the empty, PLA, and PMMA filled cantilevers respectively. The variation in time constant is directly related to the specific heat capacities of the cantilever material (SiN) and the polymers (PMMA and PLA) stored within. The trend in the observed time constants, $\tau_{empty} < \tau_{c+PLA} < \tau_{c+PMMA}$, follows the samples' specific heat capacity as c_p of SiN $< c_p$ of SiN+PLA $< c_p$ of SiN+PMMA [40], [91].

The stabilization time for the resonance frequency of the cantilever (filled with PLA or PMMA) is much longer than 60 s. If a measurement is performed by achieving full stabilization (3τ) in the resonance frequency, each measurement would take multiple hours. In order to reduce the measurement time and maintain the detection of small transitions (such as T_β), the cantilever was heated at the rate of 4 °C min⁻¹. This heating rate and stabilization time enabled rapid measurement with sufficient sensitivity and resolution.

Temperature dependent resonance spectra of the empty and polymer-filled cantilevers were measured and plotted as shown in Fig. 4.3b. In the case of the empty cantilevers, the resonance frequency initially increases with temperature, but no significant changes occur at higher temperatures. This is in stark contrast to the results from the polymer-filled cantilevers, which show

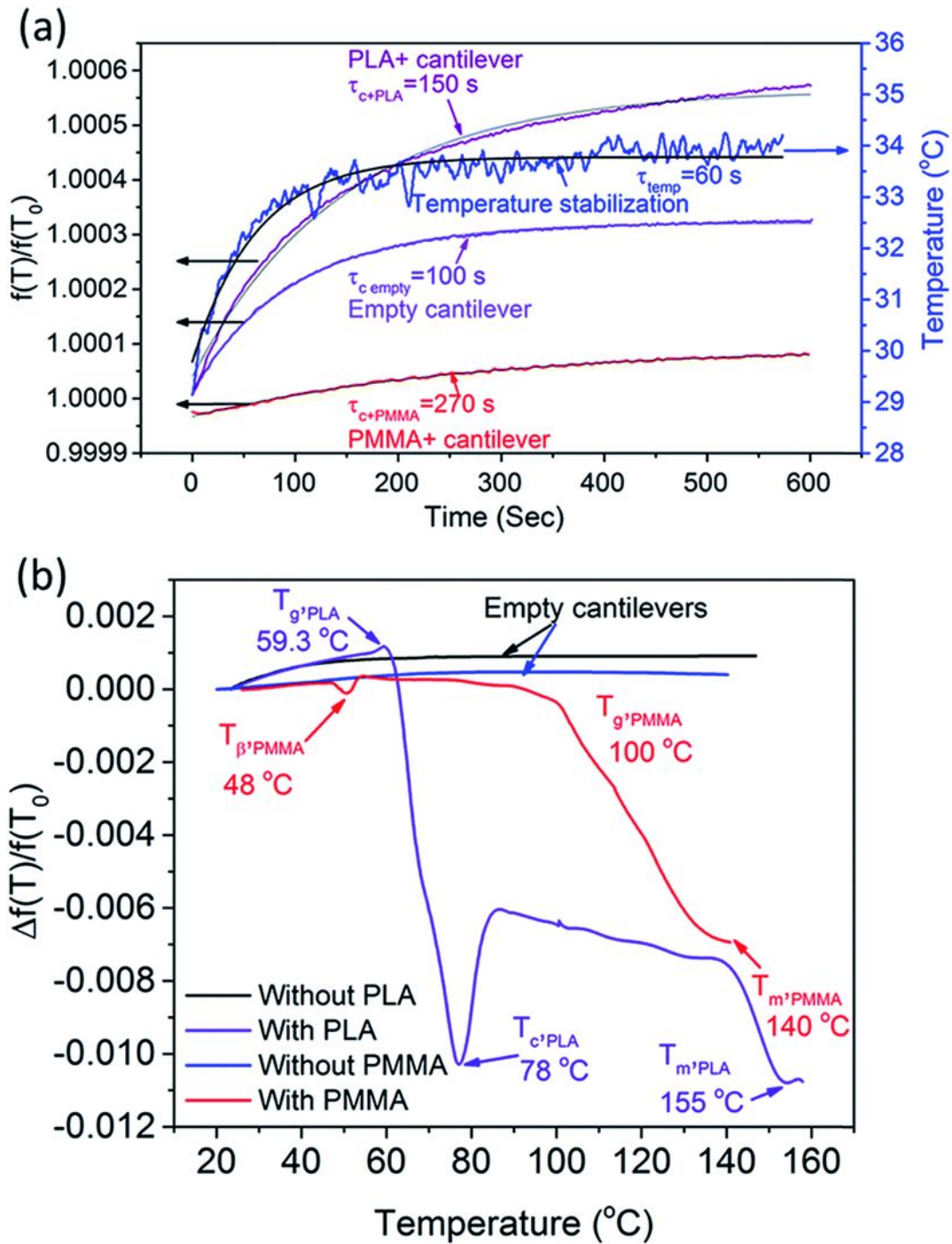


Figure 4.3: Figure3. (a)Temperature stability as a frequency measurement response for empty and polymer filled cantilevers.(b) Thermal characterization of empty and polymer filled cantilever.

a significant reduction in the resonance frequency at specific temperatures, corresponding to various thermal transitions. It is evident that the polymers undergo thermal transitions with increasing temperature, which reduces the effective stiffness of the filled cantilever, resulting in a reduction in the resonance frequency of the cantilever. Further, the stiffness of the polymer inside the cantilever was determined using eqn (4.3) and plotted in Fig. 4.4a and b.

Considering that the total mass ($m_p + m_c$) and the stiffness (k_c) of the cantilever material (SiN) are constant, the stiffness of the polymer follows the same trend as that of the resonance frequency of the cantilever. For a comparison, Fig. 4.4a shows the stiffness of the PLA sample (extracted from the results of the cantilever), as well as the measurements carried out with DSC. The overall stiffness of the PLA-filled cantilever initially increases (up to 60 °C), which is most likely due to a release of stress (in the silicon nitride). At ~ 60 °C, the stiffness of the cantilever decreases sharply which is the onset of T_g of PLA. Here the resonance frequency of the cantilever decreases by 60 Hz. The results from DSC indicate that the T_g of the sample lies within the same region. As the temperature is increased further, k_{PLA} starts to increase at 78 °C, which indicates the onset of crystallization (T_c) of PLA. This can be explained as due to an increase in the elastic modulus of PLA during crystallization, which in turn increases the stiffness of the polymer. The T_c of the sample is also evident at ~ 87 °C according to the data obtained from DSC. Melting point of the sample is determined by increasing the temperature in a continuous fashion. The onset of melting appears at ~ 154 °C (compared to 160 °C obtained from DSC) as seen by a sharp decrease in k_{PLA} . Upon melting, the viscosity of the sample decreases which explains the reduction in its stiffness.

Fig. 4.4b shows the thermal transitions of PMMA, measured by the cantilever as well as DSC. As the cantilever is heated, the sample goes through a small

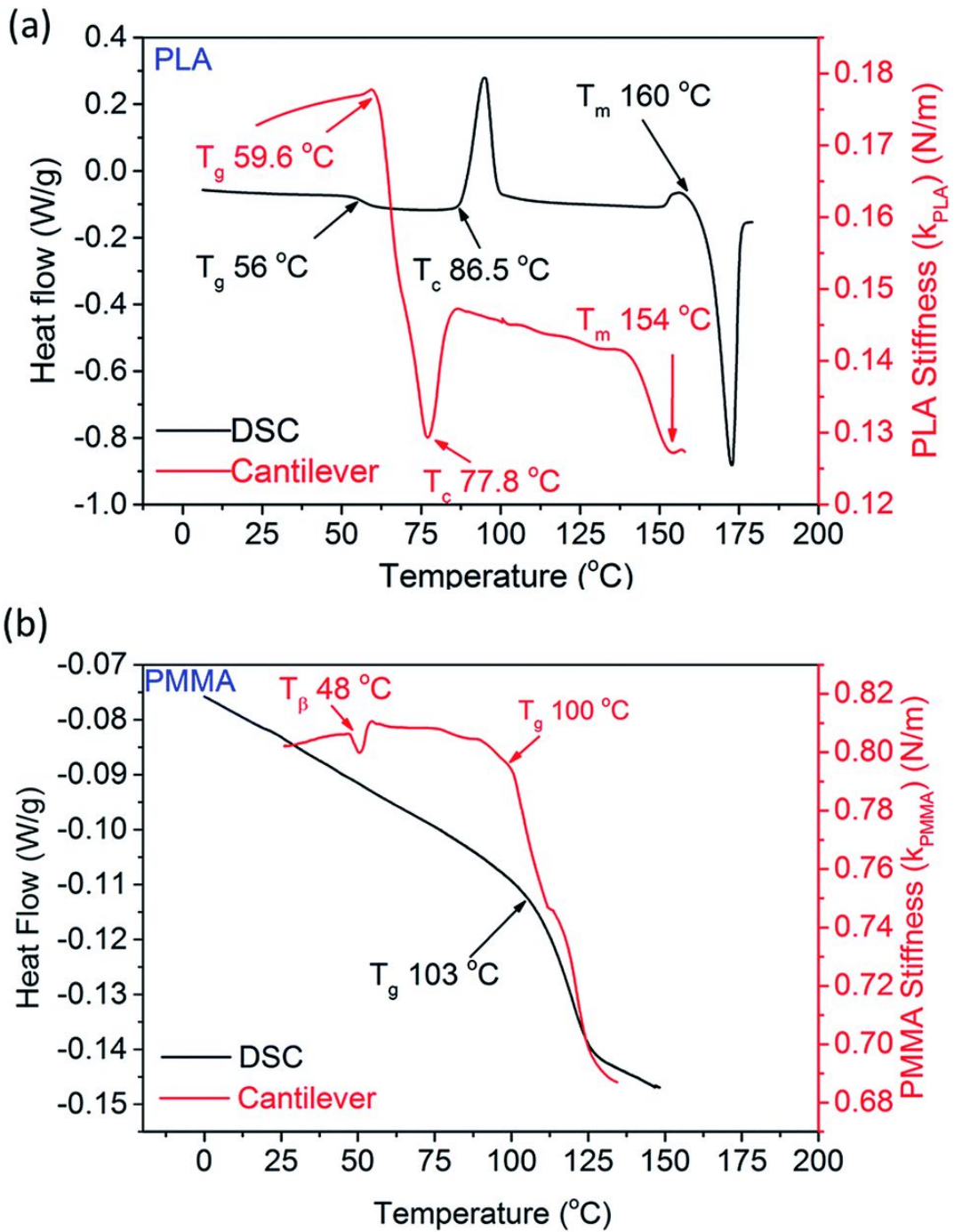


Figure 4.4: Figure4. Comparison of heat flow from DSC with the stiffness changes of PLA and PMMA as a function of temperature.

but recoverable change in its stiffness (k_{PMMA}) at 48 °C. Such a change is not visible in the data obtained using the DSC. This can be attributed to the β -transition of PMMA and can be explained as due to hindrance of the molecular motion of the $-COOCH_3$ group (attached to the main chain C–C bond) [92]. Though this transition cannot be probed using DSC, it can be measured by DMA and DEA, as reported in literature [93], [94]. As the PMMA filled cantilever is further heated to ~ 100 °C, a sharp reduction in k_{PMMA} occurs, which is identified as the T_g of PMMA. Such a change is also observed in the DSC data at 103 °C. Any small discrepancies between the temperatures reported between these two techniques may be due to the method used to determine the temperature within the microchannel.

Overall, the thermal transitions of these two polymers measured by suspended microchannel cantilever are in excellent agreement with established techniques such as dilatometry, DMA, and DES as reported in literature as shown in Table 1 in our published paper [29].

4.5 Conclusion

A suspended microchannel cantilever has been developed to use as a thermal analyzer of picogram amount of sample. Thermal transitions (T_β , T_g , T_c and T_m) of picogram amounts of polymer samples were determined by monitoring the resonance response of the microchannel cantilever. The results show an excellent agreement with the data recorded by DSC and other established techniques reported in literature. With further optimization, the microchannel cantilever has the potential to be a precise and convenient tool for thermomechanical characterization of a plethora of different expensive sample types at nano to picoscale.

Chapter 5

Thin films deposition of phase change material

5.1 Abstract

Vanadium oxide (VO_x) thin films were fabricated on SiO₂ substrates using pulsed laser deposition. Oxygen flow rate was varied by keeping the chamber pressure constant at 50 mTorr. The effect of O₂ flow rate on the crystal structure, microstructural morphology and phase transition of thin films was studied. X-ray diffraction studies showed that the VO₂ films formed polycrystalline structure and intensity of VO₂ peak was prominent for flow rate of 10-30 SCCM and decreased for flow rates < 10 SCCM and > 30 SCCM. The transition temperature shifted towards lower temperature for intermediate flow rates but the magnitude of transition was highest for flow rate of 50 SCCM. Tapping mode AFM showed the average surface roughness was minimum for optimized flow rates. Kelvin probe force microscopy (KPFM) studies showed lower work function of VO₂ for very low gas flow rates and work function of 5.6 eV at a flow rate of 30 SCCM. Upon exposing the film with 635 nm laser, the work function decreased by ~ 0.15 eV. The variation in XRD, IMT and KPFM data shows that the flow rate variation

effected the grain growth and stoichiometry of VO₂ thin films. XPS analysis showed variation in vanadium oxygen state with change of oxygen flow rate. In intermediate flow rate regime, the amplitude of phase transition was found to decrease but the onset of transition shifted to lower temperatures. The width of the hysteresis was found to increase as O₂ flow rate increased. The change in the transition width, onset temperature and total resistance change is dependent on VO₂ content in the film. This shows that flow rate of reaction gas in pulsed laser deposition is important optimization parameter for controlled growth of mixed phase vanadium oxide thin films.

5.2 Introduction

In this chapter we will discuss pulsed laser deposition (PLD) process for depositing thin films on SiO₂ substrates. The chapter is written in a paper format which will be submitted in near future, The specific title of the study is "Oxygen flow rate dependence of insulator to metal transition (IMT) of VO₂ thin films ". Experimental conditions will be optimized in order to deposit high quality films which show largest amplitude of insulator to metallic transition, highest content of VO₂ and stability. There have been tremendous efforts studying the effect of oxygen pressure on phase and quality of VO₂ thin films but practically no research study was found on how oxygen flow rate during the film deposition may also can effect the microstructure, stoichiometry, and electrical properties of the films. The optimized conditions obtained from these studies will be utilized to deposit high quality thin films on micro-string resonators. After the deposition under optimized conditions, resonators will be studied for their dynamic mechanical response under optical, electrical and thermal excitation, which will be discussed in later chapters.

O₂ undergoes a first order phase transition from a monoclinic (M1) insu-

lating phase (space group $P2_1/c$) at a temperature close to room temperature (at T_c) to a rutile (R) metallic phase (space group $P4_2/mnm$) above T_c [95–97]. The change in crystal structure causes a dimerization of alternating V atoms resulting in two different V-V bond lengths and tilting of these dimers with respect to the c-axis. The low temperature phase exhibits an indirect bandgap of 0.6 eV and a significantly large negative temperature coefficient of resistance (TCR) [98, 99]. For temperatures above T_c , the electronic concentration also increases leading to a remarkable increase in electrical conductivity.

The unique change in electronic, optical, structural and thermal properties attracted scientists to develop novel applications of thin films of this material. The properties have been explored for applications in uncooled microbolometers [100, 101], non-volatile memory [102, 103], thermal, optical and electronic switching [104–106], smart windows [107–109], memristors [110], gas sensors [55], and strain sensors [111]. However, the deposition of pure phase VO_2 thin films is difficult due to a narrow thermodynamic stability range and a large number of stable and metastable oxide phases such as VO, V_2O_3 , V_2O_5 , V_nO_{2n-1} , and V_nO_{2n+1} [112]. Most of these metallic phases have insulator to metal transition but not closer to room temperature. Several attempts have been made to optimize the deposition process by studying deposition temperature and choice of substrate effects on grain size, interfacial strain, and film thickness [1, 113–120]

Pulsed laser deposition (PLD) has a ability to stoichiometrically transfer target material directly to the substrate which offers an excellent platform to study the process parameters and optimized conditions to obtain high quality thin films. The magnitude of insulator to metal transition, the width of the transition and its shape, electrical and photo-driven insulator to metal transition are all dependent on choice of substrate, deposition parameters, and controllability of microstructure [121]. The choice of substrate can significantly effect the magnitude of both the hysteresis width and resistance

change of the temperature-driven MIT of VO₂ thin films deposited on different substrates and deposition conditions [1, 115, 118]. Despite numerous efforts made to optimize the deposition process for enhancing the properties, no study was reported (to our knowledge) which studies the effect of flow rate of oxygen on the quality of VO₂ thin films deposited with PLD process. Oxygen flow rate during the PLD deposition process using a Vanadium target plays an important role in the phase transition characteristics of VO₂ thin films. Higher flow rates of oxygen during the deposition tend to form films with higher electrical resistance at room temperature while less flow rates of oxygen tend to decrease the electrical resistance of the thin films in monoclinic phase. We will also investigate how the flow rate causes formation of either oxygen rich or oxygen deficient films and what percentage of total phase formed belongs to other metallic phases.

Here we investigate the effect of oxygen flow rate on phase transition, shape of transition, microstructure, surface potential and morphology of VO₂ thin films deposited on SiO₂ substrate. By keeping the oxygen pressure in the deposition chamber as constant, we varied the flow rate using a mass flow controller (MFC) and keep the deposition temperature, substrate, laser energy and repetition rate, and target to substrate distance as constant. We will study the effect of flow rate on transition temperature, nature of transition, oxidation state of vanadium and oxygen and surface potential variations for a range of flow rate employed.

5.3 Experimental

5.3.1 Thin films deposition

VO₂ films were deposited with PLD in an oxygen atmosphere (99.993% purity, Praxair) using a vanadium metal (99.9% purity, American Elements) circular

disc target. The deposition chamber (Excel Instruments, Mumbai, India) is schematically shown in Figure. 5.1. Vanadium target was mounted on a metallic circular disc which was further attached with a stepper motor in order to provide rotation and oscillation motion so that the laser ablates the material from all area of the target material. The target-substrate distance was set to 31 mm. Laser pulses with a 20 ns pulse width from a krypton fluoride (KrF, $\lambda=248$ nm) excimer laser (Coherent, GmbH) were directed at the target with a repetition rate of 10 Hz. Laser spot size of $1 \text{ mm} \times 3$ was maintained at the target with a constant energy density of 2.6 J/cm^2 . The deposition time was 15 minutes for all depositions on thermal oxide. Prior to deposition, the substrates were cleaned with piranha, followed by sonication in milli-Q water, rinsing in ethanol, and drying with nitrogen before putting the samples inside the chamber. The chamber was evacuated to 1.5×10^{-6} mbar and it remained under pumping for at least 3 hours. The substrate heating turned on when the vacuum level dropped below 10^{-5} mbar. After that, oxygen was introduced into the system with a fine tuned flow rate to keep the pressure in the chamber constant and we kept it flowing for one hour. A total of 7 films were deposited with seven different flow rates of oxygen. The pressure in the chamber was maintained to 50 mTorr for seven samples. We expect a maximum film thickness of 20 nm for which was calculated for samples with same deposition conditions in previous work from our group. [121], [1]. Electrical contacts were made on samples with e-beam evaporation using Ti (20 nm) and Au (80 nm) thickness.

5.3.2 Characterization

X-ray Diffraction

Thin film samples were characterized by XRD (Rigaku XRD Ultima IV) diffractometer. As deposited thin films before the Ti/Au coating were subjected to

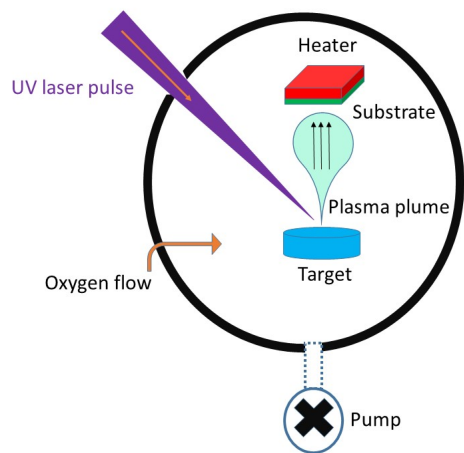


Figure 5.1: Schematic of PLD experimental setup, including the laser path and the PLD chamber.

X-rays using glancing angle mode and setting incident angle to 0.5° with Bragg-Brentano geometries. The low incident angle was required because the thickness of VO_2 films is very small and small incident angle would reduce the possibility of obtaining a background signal in the spectrum because of the substrate. Conventional 2θ scan identified the monoclinic (M1) polycrystalline peak (011) for all deposited samples with varying intensity of peak for each flow rate.

Metal-Insulator Transition Measurement

In order to investigate the magnitude, shape and width of insulator to metal transition, Keithley 2602B source meter unit was used while controlling the current and voltage with inbuilt kickstart software for two probe configuration. Fully integrated Signatone 1160 series probe station was used to provide controlled heating and current to the sample. Thermo-Scientific chiller was used to extract out the extra heat from the sample stage. Resistance vs. temperature data was acquired and plotted from 15 to 100°C for both heating and cooling cycles. The samples were heated at a controlled rate of 2°C per minute with equilibrium time of 3 minutes at each temperature before taking

Table 5.1: Deposition conditions for deposited films on *Si/SiO₂* substrate. The gas pressure (50 mTorr), target-substrate distance (31 mm), deposition temperature (600 °C) and laser fluence (2.6 J/cm²) were consistent for all experiments.

Sample ID	O ₂ flow rate (SCCM)
V-SO-31	0.5
V-SO-27	1
V-SO-28	5
V-SO-32	10
V-SO-33	30
V-SO-26	50
V-SO-30	90

a measurement. Each measurement is an average of 10 measurements taken at a constant temperature.

Surface analysis by AFM

Dimension Fast Scan Atomic Force Microscope (Bruker Nanoscience division, Santa Barbara, CA, USA) was used to measure the surface topography of the films using tapping mode. Cantilevers with the tips coated with Pt-Ir (SCM-PIT) with a spring constant of 3.6 N/m and resonant frequency of 69 kHz were used for obtaining surface morphology. Obtained images were processed using NanoScope analysis software for determining average surface roughness of the scanned area.

Kelvin probe force microscopy (KPFM) for surface potential

Kelvin probe force microscopy (KPFM) studies were carried out to obtain the work function of VO₂ for very low gas flow rates. Thermal tuning of Pt-Ir (SCM-PIT) was done before using those for obtaining surface potential image. NanoScope analysis software was used to determine the tip-surface potential

distribution and data was exported to origin for further analysis. Effect of light absorption for 635 nm red laser on surface potential were also studied by using a focused beam of external laser onto the sample while obtaining the surface analysis.

X-ray photoelectron spectroscopy

XPS Spectrometer (Kratos AXIS Ultra) at Nano fab facility at University of Alberta was utilized to perform the spectral studies on optimization of thin films deposition process. A total of seven VO₂ films were deposited under same pressure and temperature conditions and only changing the oxygen flow rate. The shift in the peak positions of XPS spectra of oxygen rich and oxygen poor samples was studied as a function of oxygen flow rate. The surface/sub-surface (~ 10 nm) chemical composition and oxidation state was determined using X-ray photoelectron spectroscopy (XPS) acquired on Axis-Ultra, Kratos Analytical instrument equipped with monochromatic Al-K α source (15 kV, 50 W) and photon energy of 1486.7 eV under ultrahigh vacuum, UHV (~ 10⁻⁸ Torr). The binding energy of C1s carbons (~284.8 eV) of adventitious hydrocarbons was used as standard and binding energy of other elements are assigned relative to C1s peak (carbon correction). The raw XPS files in .vms format was deconvoluted into various peak components using CasaXPS and the exported files was plotted in Origin 8.5

5.4 Results and discussion

5.4.1 Phase identification with X-ray analysis

Polycrystalline thin films were grown on Si substrate with pulsed laser deposition and XRD of VO₂ films was carried out at room temperature. Thin films are insulating at room temperature and exhibit monoclinic crystal structure

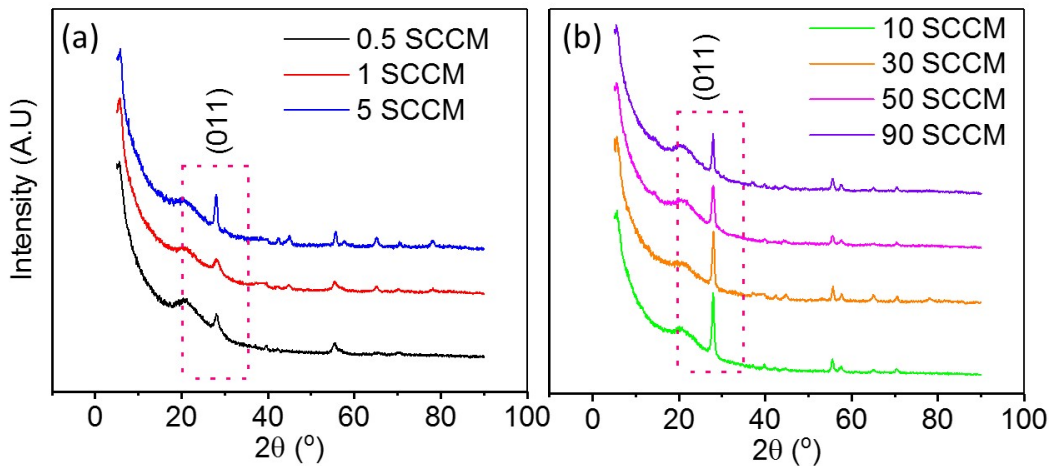


Figure 5.2: (a) XRD pattern of VO₂ films deposited on Si substrate. FWHM of (011) monoclinic peak was found to increase with increasing flow rate up to 30 SCCM and decreased again for 50 and 90 SCCM suggesting a variation in crystallite size with changing flow rates of oxygen.

which transforms to a high temperature rutile phase upon heating the films above 68 °C. We performed XRD analysis of all seven samples by comparing the data with standard JCPDS (PCPDFWIN V 2.4) file for (011) peak. The intensity of the peak varied as a flow rate of oxygen was changed. XRD pattern of all seven samples is shown in fig. 5.2.

The variation in intensity of XRD peak can be related with the growth and orientation of grains which is possibly getting effect with different flow rates. Only a tiny peak appears at 27.88° for a flow rate of 0.5 SCCM which increases only slightly when flow rate is increase to 5 SCCM. This means that the sample has only crystallized slightly with flow rates lower than 5 SCCM. Upon increasing the flow rate to 10 SCCM, we saw a large increase in peak intensity suggesting increased crystallinity of the film with increased flow rate of oxygen. Further increase in flow rate of oxygen resulted decrease in intensity of peak beyond 30 SCCM. Oxygen partial pressure inside the chamber has been demonstrated to be crucial in formation of either pure

VO₂ or other polymorphs [122]. However variation in peak intensity with changing flow rate of reactive gas is not reported before (to the best of our knowledge).

5.4.2 Insulator to metal transition

Insulator to metal transition was confirmed with two probe resistance measurement as a function of temperature. The magnitude, shape and width of the transition was studied as a function of oxygen flow rate. Normalized resistance vs. temperature data for all flow rates is shown in Figure. 5.3.

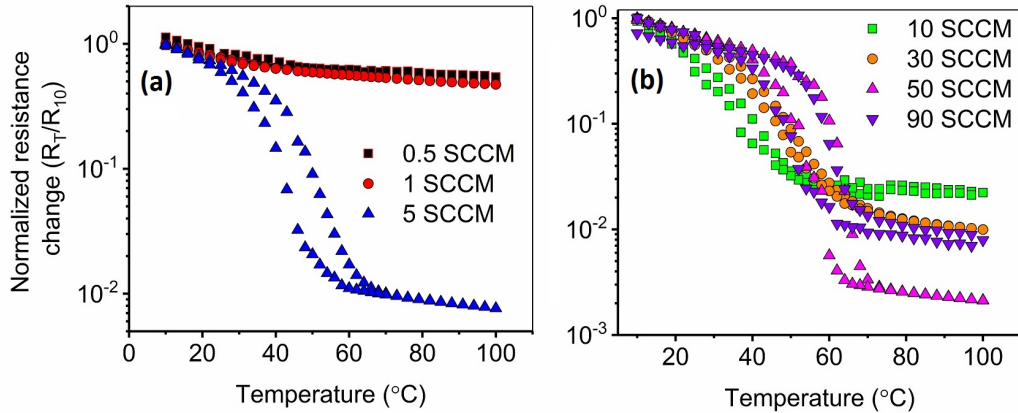


Figure 5.3: Resistance as a function of temperature for VO₂ thin films grown on silicon substrates. No transition present in case of lower flow rates of oxygen. High onset temperature with sharp and large transition was seen for flow rates of 5, 50 and 90 SCCM. Least hysteresis with lowest transition temperature was observed for flow rates of 10 and 30 SCCM.

No insulating to metallic state transition was seen for flow rates of 0.5 and 1 SCCM. However the transition appeared at 50 $^{\circ}\text{C}$ for 5 SCCM flow rate with large hysteresis in resistance. The amplitude of transition decreased for intermediate flow rates of 10 and 30 SCCM but the transition shifted to lower temperatures i.e. 42 $^{\circ}\text{C}$ and 45 $^{\circ}\text{C}$ for flow rates of 10 and 30 SCCM respectively. The largest amplitude of transition was observed for flow rate of 50 SCCM but again it appeared at high temperature with large hysteresis. The

amplitude of the transition again decreased when the flow rate was increased to 90 SCCM with quite a similar hysteresis as that of 50 SCCM sample. The shape of the transition curve reflects the content, crystal structure and grain size of VO₂ present in the film.

5.4.3 Tapping mode AFM studies

Tapping mode AFM was used to study the surface morphology of VO₂ thin films. Average surface roughness was obtained for all seven samples and found to be dependent on oxygen flow rate. Surface roughness calculations are shown in Table 5.2. Topographic scans of 1 μm × 0.5 μm for each flow rate are shown in Figure. 5.4.

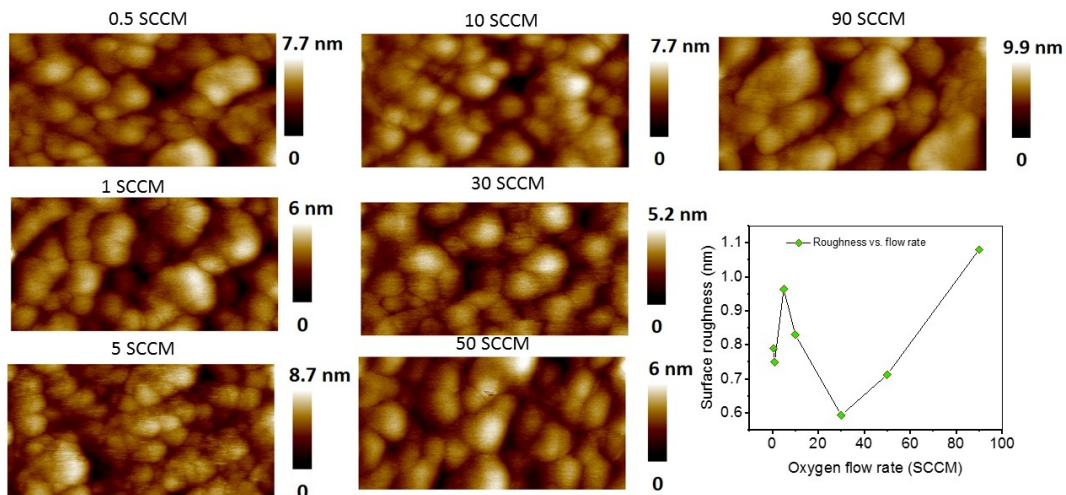


Figure 5.4: Roughness of thin films deposited under different oxygen flow rates. Variation of average surface roughness is plotted as a function of flow rate. The measured thickness of the film was 15-20 nm which was measured in our previous work [1]

There is a clear variation in the surface roughness with changing the flow rates. Rough surface was obtained for lower and higher oxygen flow rates while smoother surface was observed for optimum flow rates i.e. 10 and 30 SCCM. Lower flow rates of oxygen can possibly cause a more V/O ratio while too high flow rates can result as less V/O ratio leading to formation of

Table 5.2: Surface roughness of VO₂ films deposited on Si. Average surface roughness values were calculated using the image of interest with Bruker's Nanoscope analysis software. The peak value of the distribution of surface roughness was selected as average roughness of the sample.

flow rate (SCCM)	R ₀ (nm)
0.5	0.79
1	0.75
5	0.96
10	0.83
30	0.59
50	0.71
90	1.1

undesired phases of Vanadium oxide which can effect the microstructure and the nature of insulator to metal transition of the films.

5.4.4 Kelvin probe force microscopy for surface potential

Kelvin probe force microscopy (KPFM) can probe the local work function (ϕ) of a sample which is a characteristic of band structure[123]. Mapping the surface of VO₂ thin films can be used to examine the band bending in polycrystalline insulating sample as oxygen flow rate might be effecting the carrier concentration in the film. The local work function with KPFM is a nanoscale characterization of band structure and can provide useful insight whether the sample is more insulating, semiconducting or metallic[124]. Oxygen vacancy defects can play an important role in modification of phase transition of thin films by introducing the strain at the grain boundaries. Since the oxygen is a typical defect in VO₂ system so they tend to aggregate at grain boundaries. This concentration gradient between grains and grain boundaries can not only effect the localized work function of the grains but overall change in the resistivity of the film. Since we formulated that flow rate can effect the overall oxygen content in the films so its important to

understand how the local work function is varying with different oxygen flow rates. These point defects provide a pathway to tailor a preferential nucleation of thin films for any first-order phase change material.

Pt-Ir coated Si cantilevers with resonance frequency of 67 kHz were used to spatially map a local work function over an area of $1\mu m^2$. Work function all samples was calculated using equation 5.1 [125]. Where ϕ_{CPD} is contact potential difference measured between tip and the surface. KPFM potential scans are shown in Figure. 5.5.

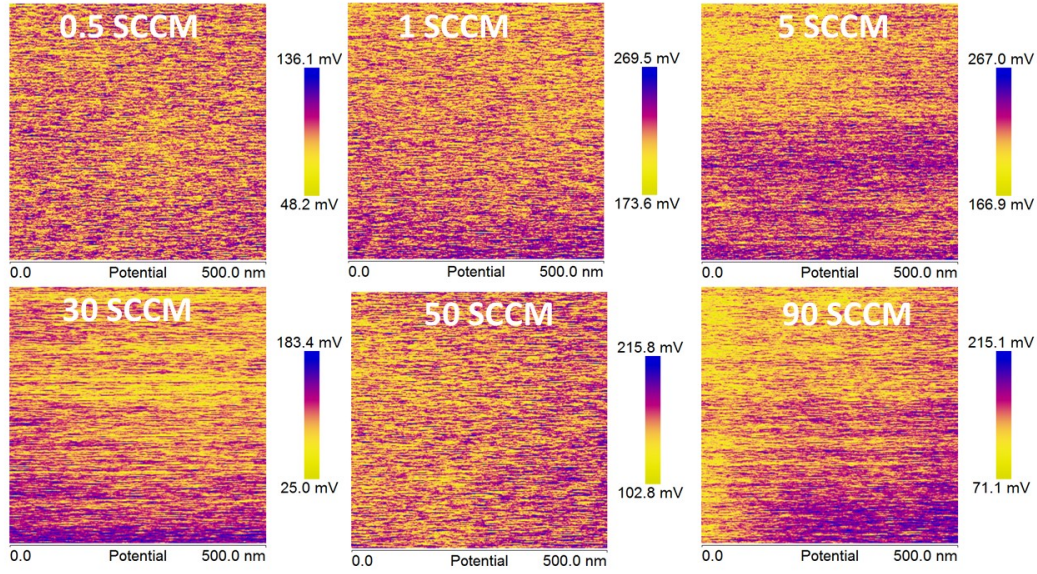


Figure 5.5: Spatial scans of $500\text{ nm} \times 500\text{ nm}$ for contact potential difference measurements with contact mode KPFM. Each scan is labeled with corresponding oxygen flow rate at which the film was deposited

$$\phi_{CPD} = \frac{\phi_{tip} - \phi_{sample}}{-e} \quad (5.1)$$

KPFM measurements were carried out for each sample by calibrating the work function of the tip with highly ordered pyrolytic graphite (HOPG) immediately before conducting the KPFM scan on each sample. Variations of surface potential of the sample was studied with and without shining a red laser (635 nm). In both cases surface potential increased up to flow

rate of 1 SCCM and started decreasing for 5, 10 and 30 SCCM and slightly increased for 50 and 90 SCCM in sample without laser. However there was not significant change in the potential for sample exposed with red laser above 30 SCCM. Average local work function dropped from 5.72 eV to 5.60 eV when the flow rate was increased from 5 SCCM to 30 SCCM in sample prior to exposing it to an optical excitation. Upon exposing the film with an external laser (635 nm, 3 mW), work function was found to drop from 5.70 eV to 5.56 eV for a flow rate of 5 SCCM to 10 SCCM. The change in work function between two curves as shown in Figure. 5.6 was ~ -0.10 eV. This suggests a shift in Fermi level when the system was exposed with an optical perturbation. The films for which the work function was highest had higher electrical resistance in the insulating phase.

5.4.5 Scanning helium ion microscope

Scanning helium ion microscope has several advantages over the tradition electron microscopes. It can provide high resolution topographic images because of higher secondary electrons yield and imaging currents as low as one femto-ampere [126]. It can image the insulating samples without any metal coating because the flood gun can help neutralize the positive charges on the surface whenever a charge build up occurs. Our thin films are semiconducting at room temperature and topographic images were obtained without any metal coating on the films. The images obtained for all flow rates are shown in Figure. 5.7. Microstructure is relatively rough at low flow rates up to 5 SCCM and becomes very smooth with small grains for 30 SCCM and again increases for higher flow rates. The grain size was maximum for 90 SCCM. By looking at the microstructure variation, we can argue that the grain size is slightly dependent on flow rates which is also evident from the tapping mode AFM analysis.

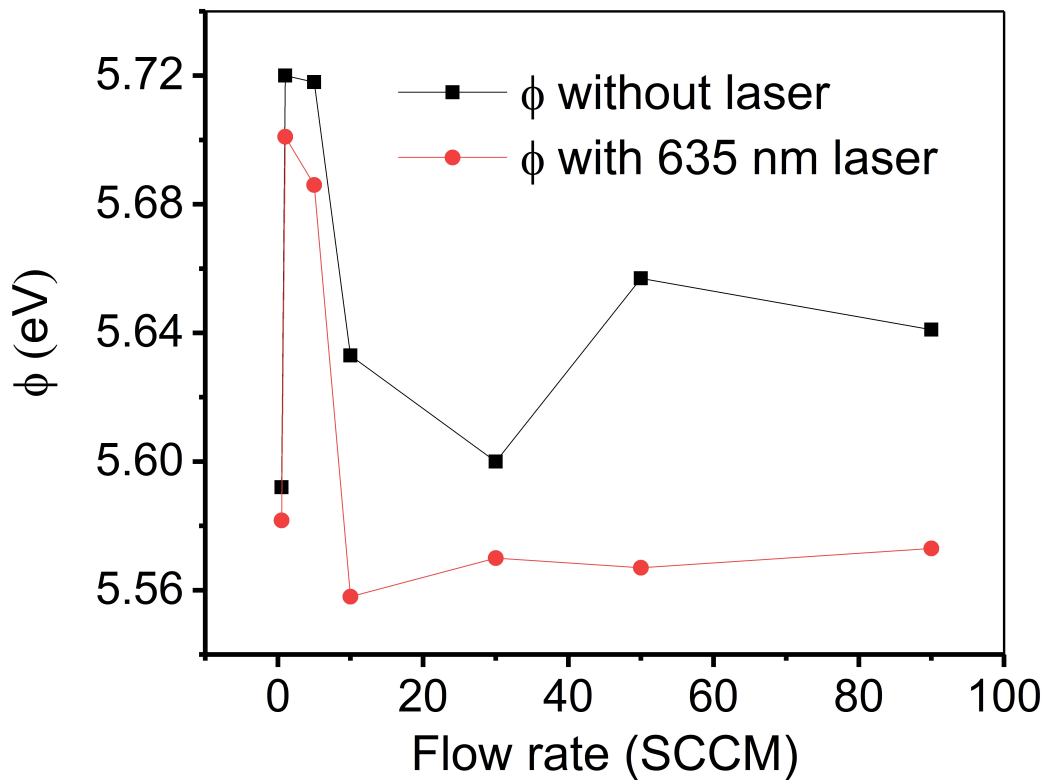


Figure 5.6: Variations of local work function of VO₂ films deposited on Si with and without the laser. The minimum of the work function appears for flow rates between 10 and 30 SCCM suggesting that an appropriate flow rate can effect the electronic properties of the films.

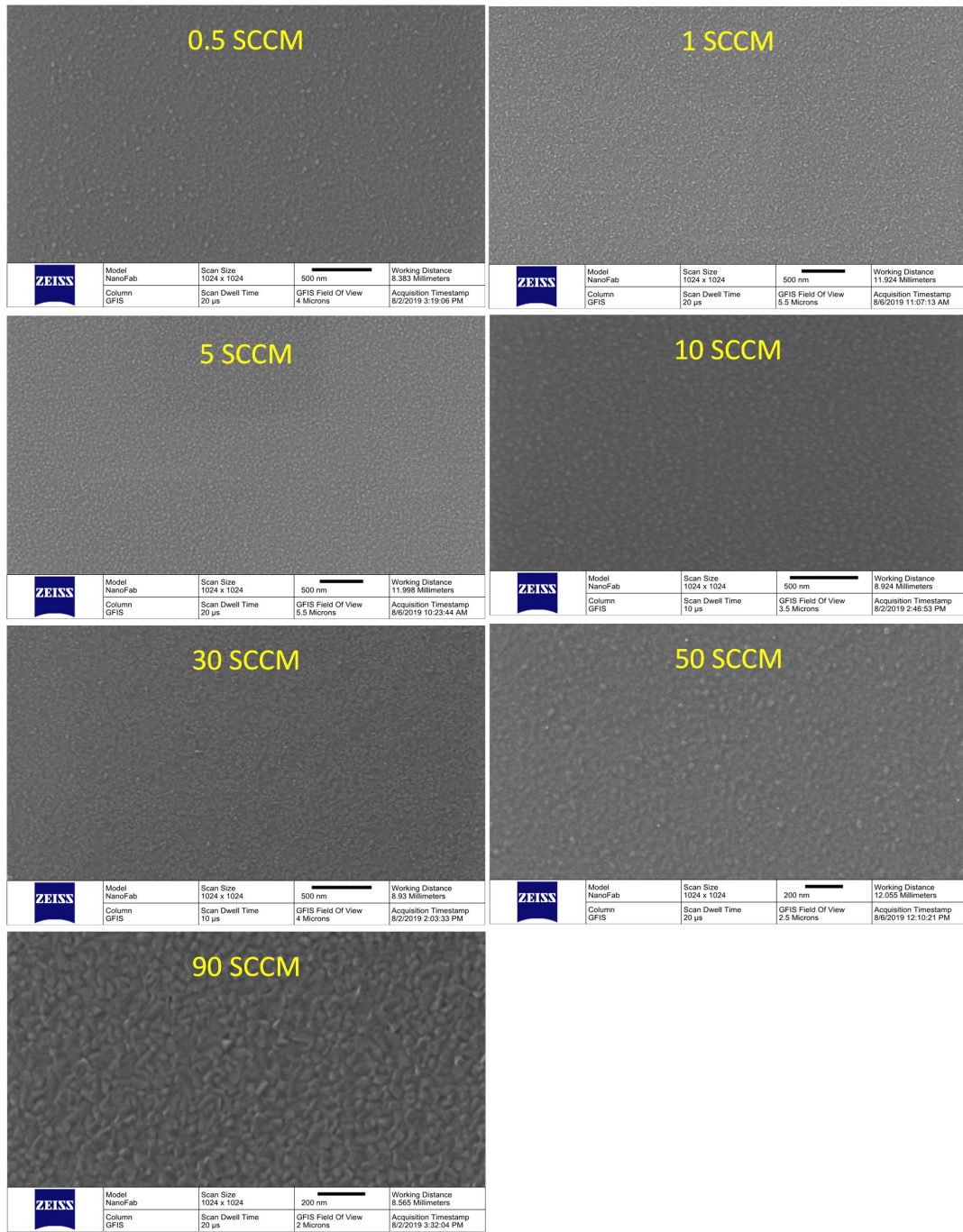


Figure 5.7: Scanning helium ion micrographs (S-HIM) of all seven samples deposited with PLD at constant pressure. Samples are labeled with oxygen flow rate. It is quite clear that polycrystalline VO_2 was formed for all flow rates but the relative grain size changed for higher flow rates. S-HIM was used to probe the surface because it offers imaging on insulating surfaces without metallic coating.

5.4.6 XPS analysis

X-ray photoelectron spectroscopy (XPS) was used to determine the surface chemical composition and binding energies of constituting elements (fig. 5.8 (a)).

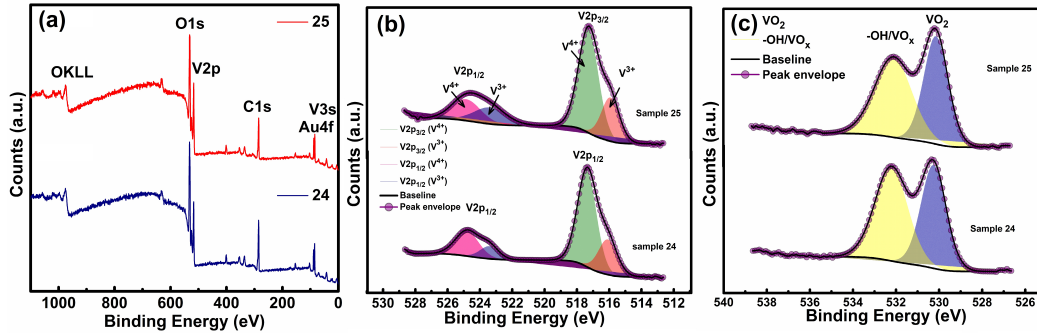


Figure 5.8: (a) XPS survey scan of VO_2 thin film treated at different flow rate, (b) Core-level HR-XPS spectra of VO_2 samples in $\text{V}2p$ region demonstrating various oxidation states and relative contribution, (c) HR-XPS spectra of VO_2 samples in $\text{O}1s$ region.

The XPS survey scan of material for elemental analysis exhibits characteristics $\text{V}2p$, $\text{O}1s$ peaks along with low and high energy core level peaks (OKLL, $\text{V}3s$) validates presence of all the composing elements. Sub-quantitative analysis by using peak to peak intensity ratio demonstrate $\text{V}2p$ to $\text{O}1s$ percentage atomic ratio at 0.5 SCCM flow rate was found 36.4/63.6 that was in between the theoretical ratio for VO_2 (33.3/63.7) and V_2O_3 (40.0/60.0) suggesting presence of both components in the material. After increasing the flow rate to 1.0 SCCM a slight decrease in oxygen contents was corroborated to transition of VO_2 (4^+) to V_2O_3 (3^+). However, further increase in flow rate (5.0, 10.0 and 30.0 SCCM) leads to increase in oxygen content (36.6/63.4, 29.7/70.3, 30.7/63.9) approaching toward atomic ratio of V_2O_5 (28.6/71.4) (Figure. 5.8 (a), Table 5.3).

Interestingly, at 50 SCCM the oxygen content was decreased slightly demonstrating partial transformation of VO_2 to V_2O_3 . Again at 90 SCCM the oxygen content gets increased (30.4/69.6). The core-level high resolution XPS

Table 5.3: XPS elemental analysis of VO₂ thin film showing the change in chemical composition of materials as function of flow rate. CasaXPS analysis software was used to determine the presence of Vanadium and oxygen in the films.

Flow rate	V _{2p} /O1 _s	V ⁵⁺ /V ⁴⁺ /V ³⁺	-OH+VO _x /VO ₂
0.5	34.6/63.6	(-)/40.2/59.8	44.5/55.5
1	43.4/56.6	(-)/70.5/29.5	49.4/50.6
5	36.6/63.4	8.8/63.2/28.0	64.3/35.7
10	29.7/70.3	28.0/44.0/31.0	72.7/27.3
30	30.7/63.9	36.0/45.6/18.4	70.3/29.7
50	42.5/57.5	(-)/60.8/39.2	47.5/52.5
90	30.4/69.6	(-)/48.1/51.9	48.1/51.9

spectra of materials in V_{2p} region show two major peaks assigned to V_{2p_{3/2}} and V_{2p_{1/2}} orbital splitting. Each V_{2p} peak components can be deconvoluted into various peak components showing existence of vanadium in variable oxidation state (Figure. 5.8 (b)). The deconvoluted V_{2p_{3/2}} peak of VO₂ thin film at 0.5 SCCM flow rate show two peak components located at 515.9 and 517.1 eV binding energy corroborated to V₂O₃ and VO₂ present as V³⁺ and V⁴⁺ oxidation state. Upon increasing the flow rate, the contribution of V³⁺ peak was decreased suggesting transition of V₂O₃ into higher oxidation state (VO₂ and V₂O₅). At 5.0, 10 and 30 SCCM a shoulder peak at BE ≈ 517.8 eV originated from V⁵⁺ oxidation state of V₂O₅ was observed which increases in order of flow rate indicating a small fraction get converted into V₂O₅. However further increase in flow rate does not reveal any existence of V⁵⁺ state and contribution of V³⁺ peak component was increased that might be due to increased flow rate oxygen molecules didn't get opportunity to adsorb/react with material. The observed pattern of relative contribution of each component is well matched with observed atomic percentage calculated from XPS survey scan.

Further, evidence of flow rate dependent transformation of oxidation state

comes from HR-XPS spectra of materials in $O1_s$ region (Figure. 5.8 (c)). The HR-XPS spectra of all the samples exhibits double peak structure and can be deconvoluted into two well-separated peak components centered at 530.2 and 532.1 eV. The peak at 530.2 eV was originated due to lattice bounded oxygen of VO_2 while another peak at 532.1 eV was observed due to cumulative contribution of non-lattice surface oxygens (-OH) and oxygens bonded with vanadium in higher oxidation state V^{5+} (V_2O_5/VO_x). From spectra it can be seen relative contribution of oxygen peaks from VO_2 was decreased (55.5 to 29.7 for 0.5-30 SCCM) while -OH/ VO_x peak was increased up to 30 SCCM agreed well with $V2_p$ XPS. For 50 and 90 SCCM flow rate the VO_2 contribution remain stable to 51-52% as expected from the $V2_p$ XPS spectrum.

5.5 Conclusion

In this work we have deposited VO_2 thin films onto thermal oxide using pulsed laser deposition and characterized the films with various techniques in order to understand the effect of oxygen flow rate in the deposition chamber during the deposition of the films. X-ray diffraction measurements revealed existence of VO_2 polycrystalline phase in all samples with a possible variation in oxygen vacancy defects. Resistance vs. temperature measurements confirmed the insulator to metallic transition in samples with flow rates > 1 SCCM but the amplitude, width and onset of transition is dependent on flow rates. No transition was observed for samples with oxygen flow rates of 0.5 SCCM and 1 SCCM. The amplitude of the transition was largest (≈ 3 orders of magnitude) for flow rates of 50 SCCM and 90 SCCM but the onset of transition was at relatively higher temperatures. A broad transition was seen for intermediate flow rates (10 SCCM and 30 SCCM) with lower onset temperatures and \approx two orders of magnitude transition amplitude. Tapping mode AFM revealed a variable average surface roughness of the samples

with relatively smooth surfaces for lowest and intermediate flow rates. Work function of the samples was studied with contact mode KPFM which revealed lowest work function values observed either at 0.5 SCCM (lowest room temperature resistance) and at 30 SCCM when sample resistance decreased again after increasing at 5 SCCM. XPS spectra showed a stable contribution of VO₂ for flow rates of 50 SCCM and 90 SCCM. There was partial transformation of VO₂ to either V₂O₃ or V₂O₅ compounds at flow rates up to 30 SCCM.

5.6 Acknowledgements

This work was supported by the Canada Excellence Research Chair (CERC) Program (ID: SF0926 and grant number: RES 0006296). The authors acknowledge the characterization facilities provided by the nanofab at the University of Alberta. Group members of Dr. Hyun-Joong Chung are acknowledged for providing valuable feedback during the group meeting presentations.

5.7 Supplementary data

5.7.1 Additional AFM Images

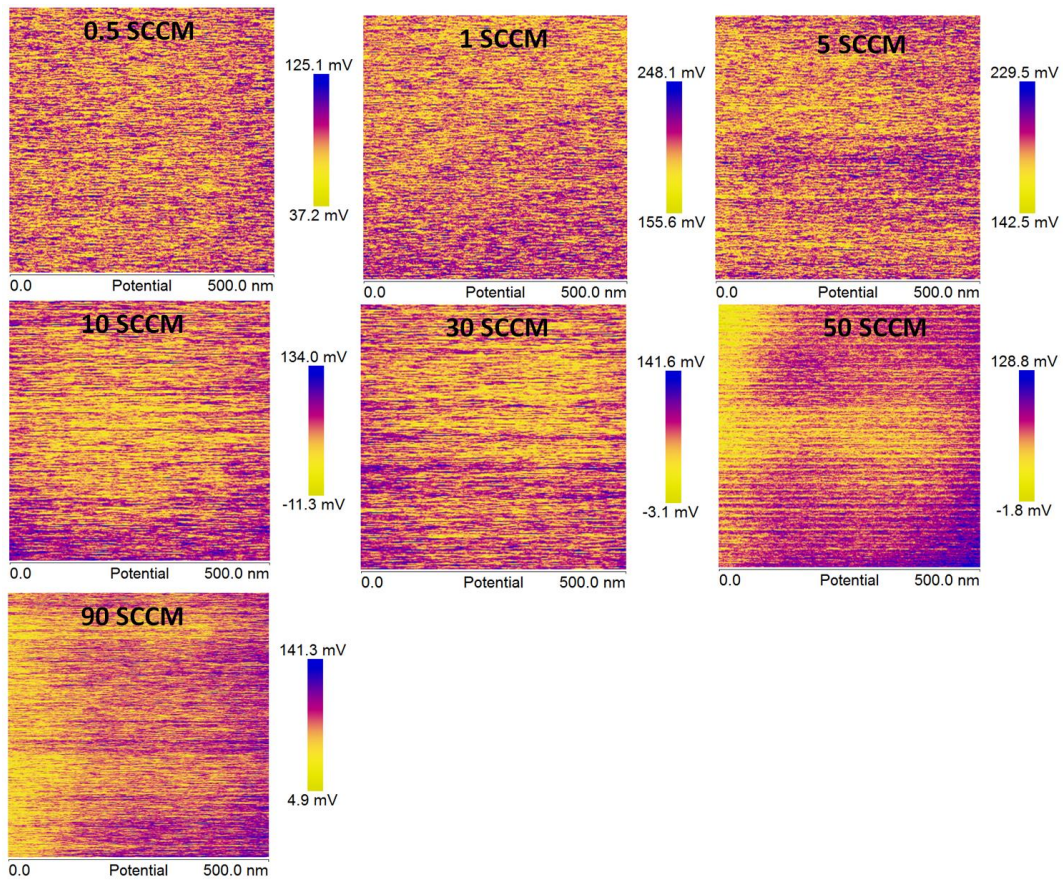


Figure 5.9: Kelvin probe force microscopy images for different flow rates with 635 nm laser ON while conducting scans.

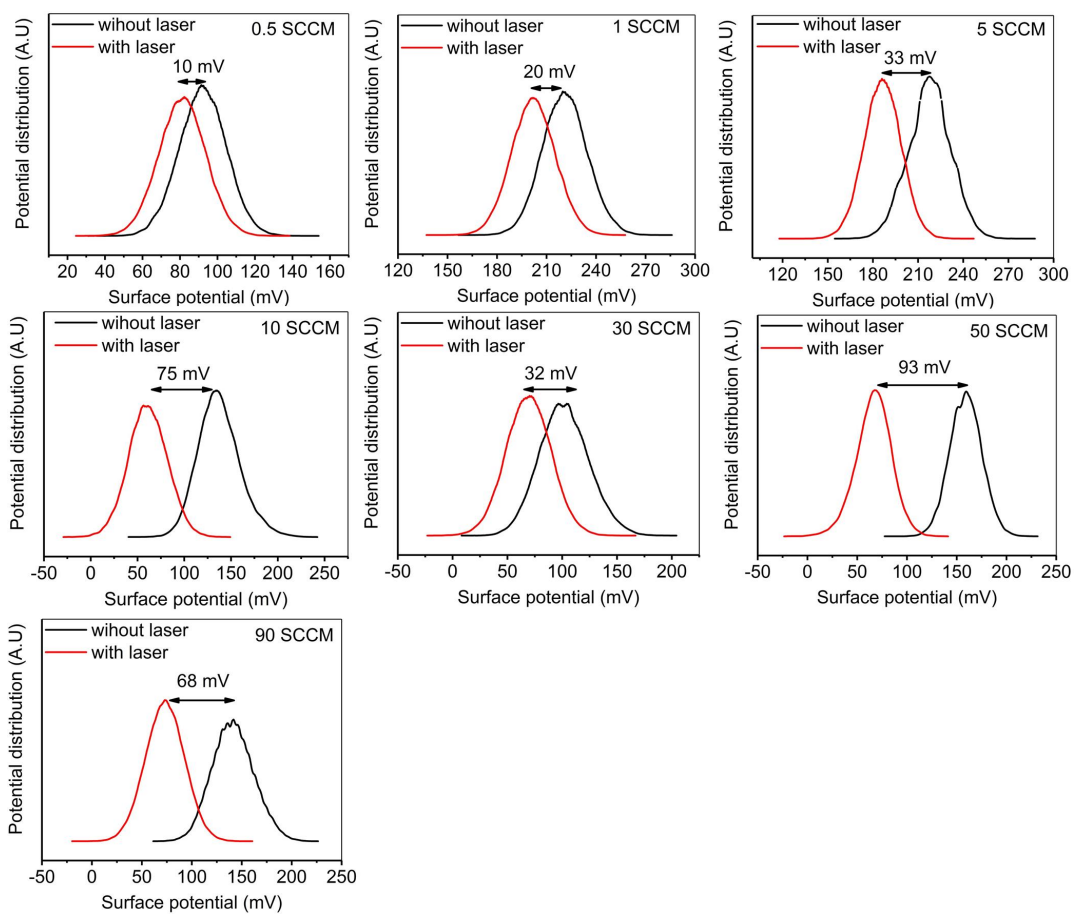


Figure 5.10: Surface potential distributions for different flow rates. Both with and without 635 nm laser.

Chapter 6

Photo induced insulator to metal transition in VO₂ microstrings and resonance frequency modulation

6.1 Abstract

Here we demonstrate mechanical detection of laser-induced Insulator to metal transition (MIT) in ultra-thin vanadium dioxide (VO₂) microstrings. Dynamic parameters of VO₂ coated strings (resonance frequency and amplitude of vibration) were studied as a function of incident optical power and gas pressure. The resonance frequency was found to be decreasing with increasing laser power from 25-38 μW and increased by 1-2 % when the laser power was further increased to 52 μW . The amplitude of vibration was also found to be consistent with the frequency data. The transition in films was induced and detected by a single pump and probe source i.e. laser built in with LDV. This trend in dynamic parameters of the strings can be co-related with reversible Insulator to metal transition in VO₂ films which creates change in density of the material and hence the overall stiffness of the strings leading to changes in string dynamics. The increase in frequency at

a particular optical power manifest a transition to a more ordered metallic phase which creates lattice compression adding a tensile stress onto the string. This noninvasive, non-contact laser-based excitation and detection of Insulator to metal transition using microstrings resonators at room temperature and with laser power in few μWs is important for low power electronic and optical switching applications..

6.2 Introduction

Micromechanical resonators have attracted great attention for their applications in frequency tuned devices which find many applications in gas sensing, ultrasensitive detection of physical quantities, signal processing and communication. The ability to tune the frequency of micro/nano electromechanical systems (MEMS/NEMS) devices has two important aspects. First, in order to compensate for the variability in manufacturing and thermal drift, frequency tuning is necessary. Second, in order to process a mechanical signal which requires signal tracking and frequency hopping tuning frequency of the devices is indispensable. In the case of MEMS/NEMS resonator, frequency tuning has been majorly attained by creating tension in the device through electrostatic pull in or Lorentz force. However, electrostatic tuning suffers due to pull-in induced failure at very high gate voltage whereas Lorentz force tuning is limited to magnetic devices. Apart from these two predominant methods of frequency tuning, there has been growing interest in electro-thermal tuning wherein frequency tuning has been achieved by employing Joule heating and has been demonstrated for silicon carbide-based nano-string resonator where frequency can be tuned up to 10%. In most of the cases tuning the mechanical frequency of the device are unidirectional i.e. either frequency increases or decreases with external stimuli. However, there have been rare literature available where bidirectional frequency can be tuned using the

same resonator employing external perturbation. Vanadium dioxide (VO_2) is one such material, which can satisfy this requirement to a larger extent. Strongly correlated systems provide a diverse range of complexity and functionality. These materials show a colossal change in response to the external stimuli such as electric field, magnetic field, temperature and light. Single crystal and undoped VO_2 exhibits reversible metal-insulator transition ideally at 68°C where it transforms from semiconducting monoclinic (M1) phase to metallic rutile (R1) phase[96]. The transformation is ultra fast (~ 100 fs) and ideally shows minimal hysteresis ($<1^\circ\text{C}$)[127]. Numerous literature has been devoted to measure the MIT of VO_2 by measuring the electrical resistance change as a function of temperature [121], [128]. Femtosecond laser pulses have been used to investigate the ultrafast nature of optical switching of VO_2 thin films keeping films at temperatures close to MIT transition temperature [129]. This study demonstrated that high temperature metallic phase was obtained within a timeline of 5 ps which opened up the doors for future researchers investigate further in order to develop technological applications.

This ultrafast transition in VO_2 was further investigated with reflectivity and transmission measurements and a timescale of sub picoseconds was measured for this transition [130]. Femtosecond x-ray absorption spectroscopy was used to investigate the femto-seconds electronic rearrangements produced by photoinduced insulator to metal transition [131]. Another important study was done on visualization of phase transformation from insulating to metallic phase by looking into atomic movements using ultrafast electron crystallography and the transition was observed to be in femtosecond time regime [2]. Terahertz pulses have been used to probe the solid-solid phase transition with the transition observed to be happening in short times of sub-pico seconds [10]. The ultrafast nature of this transition gave a motivation to integrate VO_2 thin films in MEMS structures and the expectation would be to have a reasonable fast time response of the resonators because of the

insulator to metal transition.

However, Rua et al.[132] were first to demonstrate the change of thermal and mechanical parameters of VO₂ such as coefficient of thermal expansion (α) and lattice strain (ϵ) by measuring the curvature change ($\sim 2100 \text{ m}^{-1}$) of VO₂-coated microcantilever under thermal cycle. This experiment opened the avenue to explore the MIT of VO₂ from a perspective of mechanical modulus changes and its relation to change in curvature of resonators. Later, Cabrera et al. showed that the bending of a VO₂ coated silicon microcantilever can also be triggered by photothermal stimulus or electro thermal actuation [133],[134]. In the former case, the cantilever was heated by laser source while in the latter scenario the thermal energy was supplied to the cantilever through the monolithic heater embedded in the VO₂ coated cantilever.

In both the cases the measurements were focused on bending of cantilever as in the case of cantilever structure the generated stress would be mostly released and transformed into bending. Whereas, in the case of doubly clamped cantilevers or micro-bridges the generated stress is contained within the structure due to the absence of any free-end unless the stress surpasses the Euler buckling limit. Hence, microstrings are more sensitive than singly clamped cantilever when measurement parameters are considered as frequency. These two observations were proven in the case of VO₂ systems by two different studies by Rua et al. and Marced et al. respectively. In the former case, tuning frequency was possible up to 3.6 % for 100 nm thick VO₂ coated cantilever with the function of temperature posing large hysteresis under heat-cool cycle. They showed the frequency of the cantilever increases near the MIT region where large stress is generated due to the structural transformation from insulating to metallic state. Later McGee et al. also found the similar observation in the case of 25 nm VO₂ coated silicon nitride (SiN_x) cantilever where they improved the frequency change up to 5 % with negligible hysteresis using TiO₂ as a buffer layer[64]. In both the reports they showed the

frequency of the cantilever increases at MIT and stabilizes after the transition. On the other hand, Merced et al. showed VO₂ coated SiO₂ microbridges have the capability to tune the frequency up to 23 % under where frequency largely decreases within the regime of 30 to 100 °C except the MIT zone (55 to 60°C) where 5 % frequency increment is observed [135]. Hence, Merced study showed bidirectional frequency tuning when microbridge platform is used. This idea allowed us to choose microstringing as a platform for VO₂ based frequency tuning device.

Conversion of photon energy into thermo-mechanical actuation is highly attracted research field in the scientific community because of potential applications in wireless actuation and remote control of soft robotics, sensors and thermomechanical energy harvesting devices. Photo-induced actuation can be precisely controlled by adjusting the multi-option input parameters of electromagnetic radiation e.g. wavelength, polarization, intensity and monochromatic filtering[136]. This remote actuation process is strongly dependent on structural assembly of the photo actuator as photo induced nanoscale deformations must be transformed to a macroscopic motion in order to use the structure for practical applications. Structural change in phase effects the optical and electrical properties which makes VO₂ an important candidate material for ultrafast optical, thermal and electronic switching [19], [137],[138], microbolometers [139], microcantilevers [64]and gas sensing [55].

In this study, we developed VO₂ and VO₂/TiO₂ coated suspended Pt/SiN microstrings which can show bidirectional frequency tuning under thermal cycle which has been reported in literature [135]. However, we show that this frequency tuning can be achieved by not only using very low optical power (< 1mW) but also changing the wavelength as well. Resonance frequency of the microstrings was tuned with highly focused optical power which can trigger the localized transition in the film and frequency can be tuned for a

range of input power. In second part of this study, we demonstrated that the resonance frequency can also be tuned by changing the wavelength of the optical spectrum. We showed that by keeping the probe laser at its minimum power ($\sim 20 \mu\text{W}$), and using an external LED laser to pump the system, the response is different at different wavelengths of laser because of the variations of optical absorption of VO_2 .

6.3 Experimental methods

Silicon nitride microstrings of different lengths were fabricated following a process recipe shown in Figure. 6.8 (S1). Released strings characterized by measuring their resonance frequency and amplitude of vibration at resonance. VO_2 and TiO_2 films were deposited onto all the strings at once by pulsed laser deposition (PLD) using Ti and V targets and in previously optimized oxygen flow rate (30 SCCM) with a chamber pressure of 50 mtorr. The distance from target to the substrate was maintained at 31 mm for all the depositions. A high energy KrF ($\lambda = 248 \text{ nm}$) excimer laser (Coherent, GmbH) with a fluence of 2.6 J/cm^2 was used to vaporize the material and deposit it onto the substrate which was held at a constant temperature of $600 \text{ }^\circ\text{C}$. The pulse repetition rate was set to 10 Hz and deposition was done for 15 minutes which means a total of 9000 pulses were used to deposit a film with a thickness of VO_2 ranging between 15-20 nm as reported in our previous work [1]. After deposition the phase and crystallinity was determined by X-ray diffraction (XRD) Rigaku Ultima IV diffraction system. Scanning helium ion microscope (Zeiss Orion NanoFab HiM w/ Ga-FIB (Trinity)) was used to obtain high resolution images of both coated and uncoated microstrings without doing any metallic coating on the strings.

Laser Doppler Vibrometer (LDV) is one state of the art technique which can be used for probing and exciting the MIT in VO_2 films deposited on Pt/SiN

microstrings. High resolution frequency and amplitude measurements were made using LDV by placing the strings into a high vacuum chamber. Microchip containing all resonators, piezo and Pt-1000 temperature sensor were fixed with peltier element in close proximity. The other side of the peltier was connected with a heat sink. The resonance frequency was continuously measured with each data point measured in 0.5 seconds while temperature was cycled between 25-90 °C at the an approximate rate of 2 °C per minute by driving the peltier element with a BK Precision 9183 power supply with a software controlled constant current and varying voltage scheme. The temperature of the system was measured with a Keithley 197 multimeter interfaced with LabView.

Once the temperature vs. frequency data was acquired and the insulator to metal transition was confirmed from the frequency increase of the strings, frequency response at room temperature was recorded by varying the built in power of LDV which can be varied at seven different levels. External diode laser with power (< 5 mW) were used by shining the light onto the strings at an angle of $\sim 45^\circ$ while keeping the LDV built in laser at minimum power. In both cases the power at the position of the string was measured using ThorLabs PM100 optical power meter. The total power contains the background power since we were working while the lights were on. Experimental set up for measuring the frequency response of VO₂ coated strings is shown schematically in Figure. 6.1.

6.4 Results and discussion

6.4.1 Frequency modulation with single pump and probe

Here we used built in LDV laser to vary the optical power and observe the mechanical response of VO₂ coated microstrings. First mode resonance

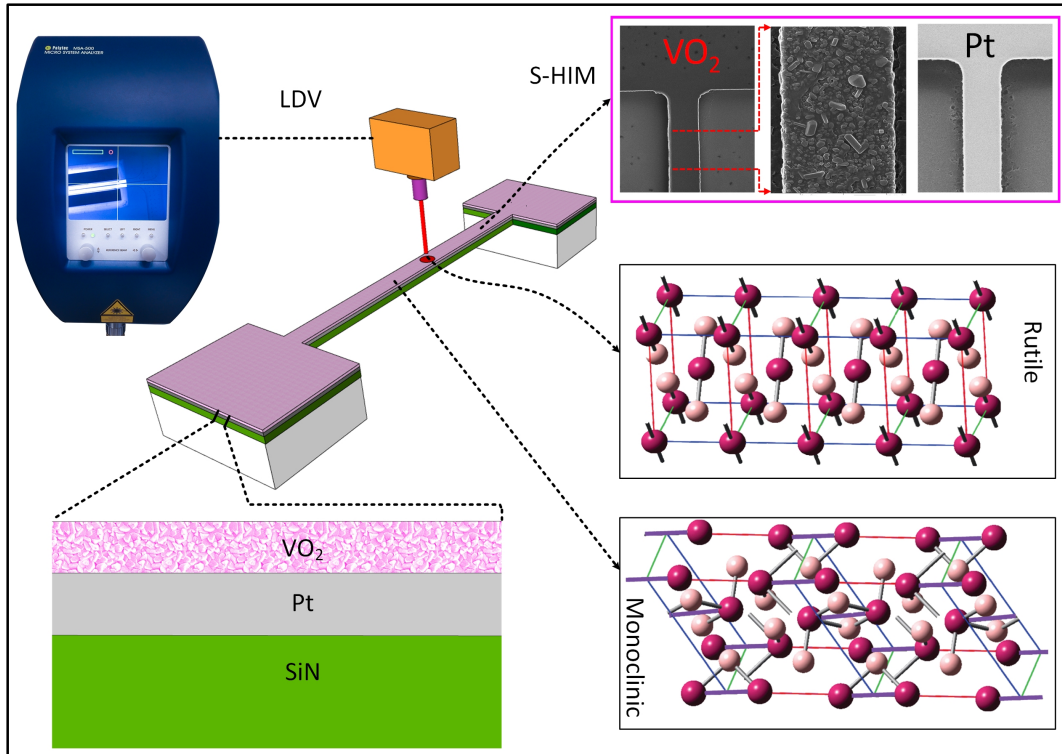


Figure 6.1: Schematic layout of non-contact laser based MIT measurement of VO₂ microstrings using LDV. The string has 15-20 nm VO₂ layer deposited on Pt and with 250 nm SiN as a base layer. The microstructure of VO₂ layer was taken with S-HIM at 500 nm resolution and imported into MS-Visio. Frequency and amplitude response of the VO₂ microstrings was recorded through Laser Doppler Vibrometer by exciting the string at its first resonance mode with forced actuation via a piezo. Scanning helium micrographs were taken at a resolution of 2 μm and at a working distance of 9 mm without any gold coating. The zoomed portion of the string was taken at 500 nm resolution and polycrystalline VO₂ structure can be seen. A structural transition with incident optical power above 38 μW will change the material from semiconducting monoclinic to metallic rutile phase [2]. It is assumed the focused laser beam can excite the IMT mechanism at a localized spot and that will change the dynamics of the microstrings. That is the reason for showing the rutile phase existing only where the laser is focused.

frequency before and after deposition of VO₂ is shown in Figure. 6.2(a). The resonance frequency and the amplitude of vibration dropped after depositing VO₂ layer because of addition of mass on the resonator. However when the coated resonator was heated from room temperature to 80 °C, the resonance frequency increased by 13 kHz. This was likely because of addition of tensile stress on the resonator because of lattice compression when the top layer transformed from monoclinic to rutile crystal structure.

Comparison between the resistance and frequency variations as a function of temperature is shown in Figure. 6.2(b). Two probe resistance measurements were done with probe station and controlled heating and onset of insulator to metal transition was observed close to 50 °C with a resistance change of 3 orders of magnitude at 80 °C compare to room temperature. This showed confirmation of thermally induced MIT in the resonator. On the same plot frequency vs. temperature data was obtained using same heating/cooling conditions while recording the resonance frequency of the resonator continuously with an interval of less than 0.5 seconds for each frequency data. At low temperatures, the frequency of the resonator started to decrease because of a decrease in Young's modulus E with temperature. There was a drastic increase in resonance frequency around 37 °C likely happened because of the additional stress generated on the resonator when VO₂ film transformed its crystal structure. This behavior can be explained by conventional beam theory additional tensile stress can increase the resonance frequency [90].

$$f_0 = 1.03 \frac{h}{l^2} \sqrt{\frac{E}{\rho}} \sqrt{1 + \frac{Sl^2}{\pi^2 EI}} \quad (6.1)$$

where l is the length of the string, h is thickness, S is tensile force, I is moment of inertia and ρ is density of the string. This equation is valid for a single material but can provide a platform to understand the effect of tensile stress onto the frequency assuming negligible residual stress on the string. The

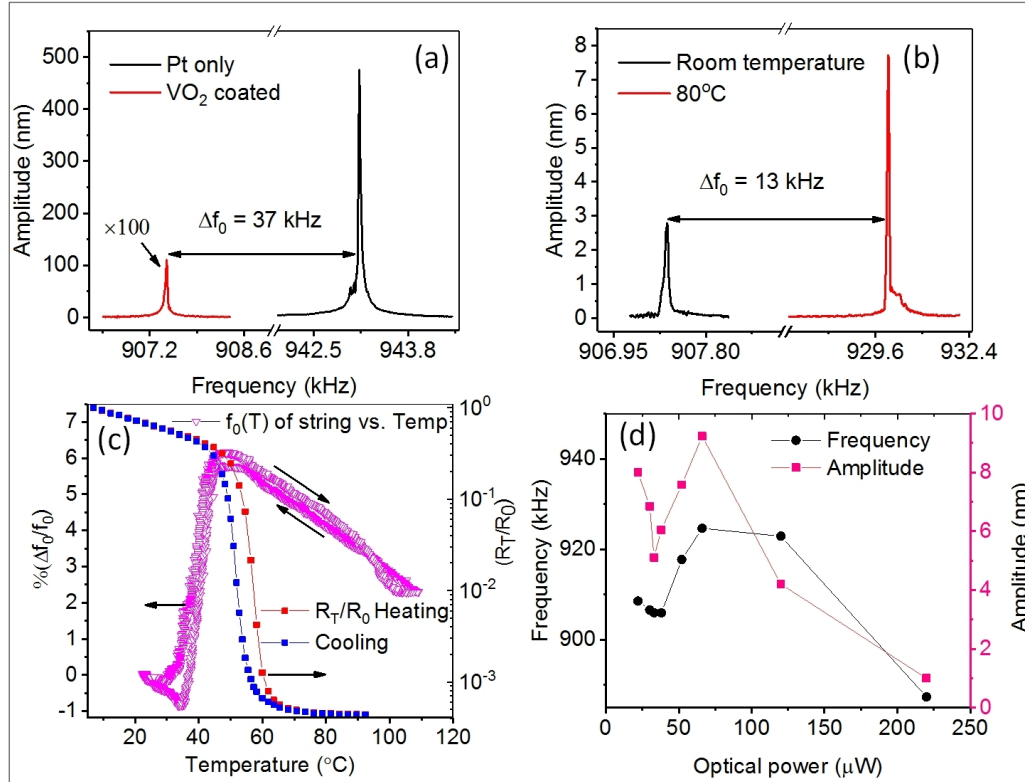


Figure 6.2: (a) FFT spectrum of VO₂ coated Pt strings on SiN in comparison with Pt/SiN strings. The decrease in resonance frequency corresponds to the added mass on the string. (b) VO₂ deposited string was heated to 80 °C and FFT spectrum was recorded. There is an increase in frequency by 13 kHz which is likely because of the top layer transitioning to metallic phase accompanied by a change in crystal structure leading to in plane tensile stress which would increase the stiffness and overall increase in frequency. (c) Shows comparison of electrical resistance and resonance frequency change of the string as a function of temperature. There is more than 3 orders of magnitude change in electrical resistance near 55 °C and $\Delta f/f \sim 6\%$ change in resonance frequency of the string. The resonance frequency changed in three different regions i.e. at temperatures slightly above room temperature, around the IMT transition and above IMT can be correlated with softening of the string at low thermal powers, triggering of IMT and causing a huge stress on top layer and hence increase in frequency and decrease in frequency upon further heating beyond 60 °C. The latter is most likely softening of the rutile phase after all VO₂ crystallites were transformed to rutile phase and further heating would only soften the material as expected. Frequency and amplitude variations as a function of optical power. (d) Here LDV laser was used for pumping and probing the system. A slight decrease in frequency and amplitude at very low optical excitation with a sharp increase near 50 μ W and a further decrease above 75 μ W can be correlated with decreased Young's modulus with heating, triggering of insulator to metal transition and further decrease in modulus of the rutile crystal phase of VO₂ respectively.

resonance frequency of doubly clamped beam resonators made out of SiN has been demonstrated to decrease with increasing temperature assuming the strings have been thermally cycled many times in order to release the residual stress [140]. The further decrease in frequency was observed beyond 60 °C suggesting that the top layer has been completely transformed to rutile structure and further increase in temperature lead to an overall decrease of the modulus of the system becoming more dominant phenomena compare to the stress induced increase in frequency.

The resonance frequency also followed similar trend while microstrings were subjected to an increasing optical power of laser beam which is focused at the center of the string as shown in Figure. 6.2(d) Part of the laser was absorbed which is designated as pumping laser. The reflected part of the laser is designated as probe laser. We see a decrease in frequency and amplitude when the pump and probe was at lower power levels. However the frequency jumped up for laser power beyond 38 μW and again decreased beyond 75 μW . The increase in frequency is probably because of highly focused laser creating a localized temperature increase to such an extent that material under laser exposure is changing its phase and hence adding stress onto the resonator which may increase the resonance frequency. Another fact is that the system is under vacuum and there are no convectional heat losses. Two anchor points of the strings are the only two heat sinks which have a cross sectional area of $1.5 \times 10^{-12} \text{m}^2$. This small area would eventually lead to a small heat flux and loose of heat into the sink and hence utilizing most of the laser power being increasing the temperature at a localized location. The further decrease in frequency is quite consistent to the behavior shown in part (c) which is domination of decrease in overall modulus as compare to stress induced increase in frequency.

Resonance frequency and amplitude variations measured by the LDV as a function of pump and probe optical power are shown in Figure. 6.3. Opti-

cally excited mechanical dynamics of the resonator are explained in terms of FFT spectrum as a function of laser power (Figure. 6.3 (a),(b),(c)) stability of resonator at different laser powers (Figure. 6.3 (d),(e)) and comparison of uncoated strings with VO₂ coated strings under the optical excitation (Figure. 6.3 (f)). There were seven different optical power levels ($P_0 - P_6$) were employed using pump and probe laser and the optical power at each of those levels was measured via Thorlabs PM 100 optical power meter. Power levels and optical power density of highly focused laser beam is shown in Table 6.1.

At a constant piezo force, frequency and amplitude show a decreasing trend for optical power $P_0 - P_2$ as shown in part (a) of Figure. 6.3 which is normally expected as the increasing temperature will decrease the modulus and hence the stiffness of the resonator which lead to not only decrease in frequency but in magnitude of vibration as well. However near to 40 μW , we saw a 1.8% increase in frequency. Above 52 μW , frequency started decreasing again. The increase in frequency can be correlated with an increased surface stress because of localized MIT in VO₂ at the top of the string. Since the geometry of the film might also change because of the change in crystal structure of the film, it is possible that the increase in frequency is a combination of both the surface stress and elastic deformation of the film. Upon further increase in laser power, the exposed area of the film may have been transformed to highly metallic state and therefore the decrease in frequency is again controlled by the Young's modulus change. At highest optical power, not only the frequency drops but the quality factor and the amplitude of vibration also decreases significantly because the area under exposure becomes soft and causes damping in the passage of acoustic wave generated by piezo resulting a large portion of that energy lost in each cycle of vibration. The stability of resonance frequency and amplitude was studied by continuously measuring recording the data for three minutes as shown in Figure. 6.3 (d) and (e). Frequency was very stable for all optical power levels except the

highest laser power P_7 while the amplitude was most unstable for laser power P_5 . Uncoated strings did not show any increase in frequency or the amplitude as compare to VO₂ coated strings as shown in Figure. 6.3 (f) suggesting the increase in frequency is only observed because of the insulator to metal transition. In order to further clarify this fact, we used a TiO₂ coated string of similar dimensions and observed decrease in frequency as a function of incident power as shown in supplementary information (Fig. 6.9).

After analyzing the stability and comparison studies, we studied the effect of pressure on the variation of frequency and amplitude. A controlled pressure was developed inside the chamber by flowing air via a needle valve and turbo pump operating at 300 rpm. The magnitude of the frequency change because of MIT (shown in Figure. 6.4(b)) is weakly dependent on the ambient pressure. A sharp transition was observed at the lowest vacuum level i.e. at $P_0(3 \times 10^{-5}$ mbar) but as we increased the pressure sharpness decreased slightly until we reach a pressure of 1.4 mbar (P_6). The final frequency value also increased with increasing pressure because all the heat produced by laser was conducted through the boundaries of the suspended string but a part of that heat also lost because of the conduction through air molecules. This would lead to a lower temperature on the film and a bit higher value of modulus which would increase the frequency.

Amplitude response of VO₂ coated string showed a peak around the same incident laser power where frequency increase was observed (shown in Fig. 6.4). The peak value of the amplitude at lowest pressure P_0 was found to increase by 60% at an incident laser power around 52 μ W which reduced with increasing ambient pressure because of the damping effect. At lower power, amplitude decreased with increasing laser because of decreased stiffness caused by the increasing temperature. Similar trend was observed if we increase the power beyond 52 μ W which would be again dominated by the decreased stiffness effect. Increase surface stress may have played a role in in-

Table 6.1: Optical power and density calculations. The power values were experimentally measured while the density is approximately calculated using dimensions of the resonator at the point of exposure. The values were measured by placing a Thorlabs PM 100 photo detector at the same distance from the LDV where microstring was placed. The glass cover of experimental vacuum chamber was also placed in between the LDV and the photo-detector. The power measured includes the background room light as well.

Power level	Measured P (μW)	Density (kW/cm^2)
P ₀	22	0.40
P ₁	30	0.54
P ₂	33	0.60
P ₃	38	0.68
P ₄	52	0.94
P ₅	66	1.19
P ₆	122	2.20
P ₇	220	3.96

creased amplitude at the power values where we see the onset of MIT in VO₂. Increased surface stress could increase the overall stiffness and reduction in loss of mechanical power delivered by the piezo which leads to an increase in amplitude of vibration.

6.4.2 Frequency modulation with external source

Selective tuning of mechanical frequency of VO₂ microstrings is demonstrated by varying the frequency of external (pump) optical power while keeping the probe optical power at a minimum level. VO₂ has a solid state phase transition above a critical temperature which not only changes the insulator to metal but also changes the lattice symmetry because of change in crystal structure. Integration of VO₂ with MEMS provide a platform where mechanical system can take advantage of the phase transition property which may lead to an increased functional tuning of the devices [141]. Here we demonstrate that mechanical frequency can be tuned while changing the

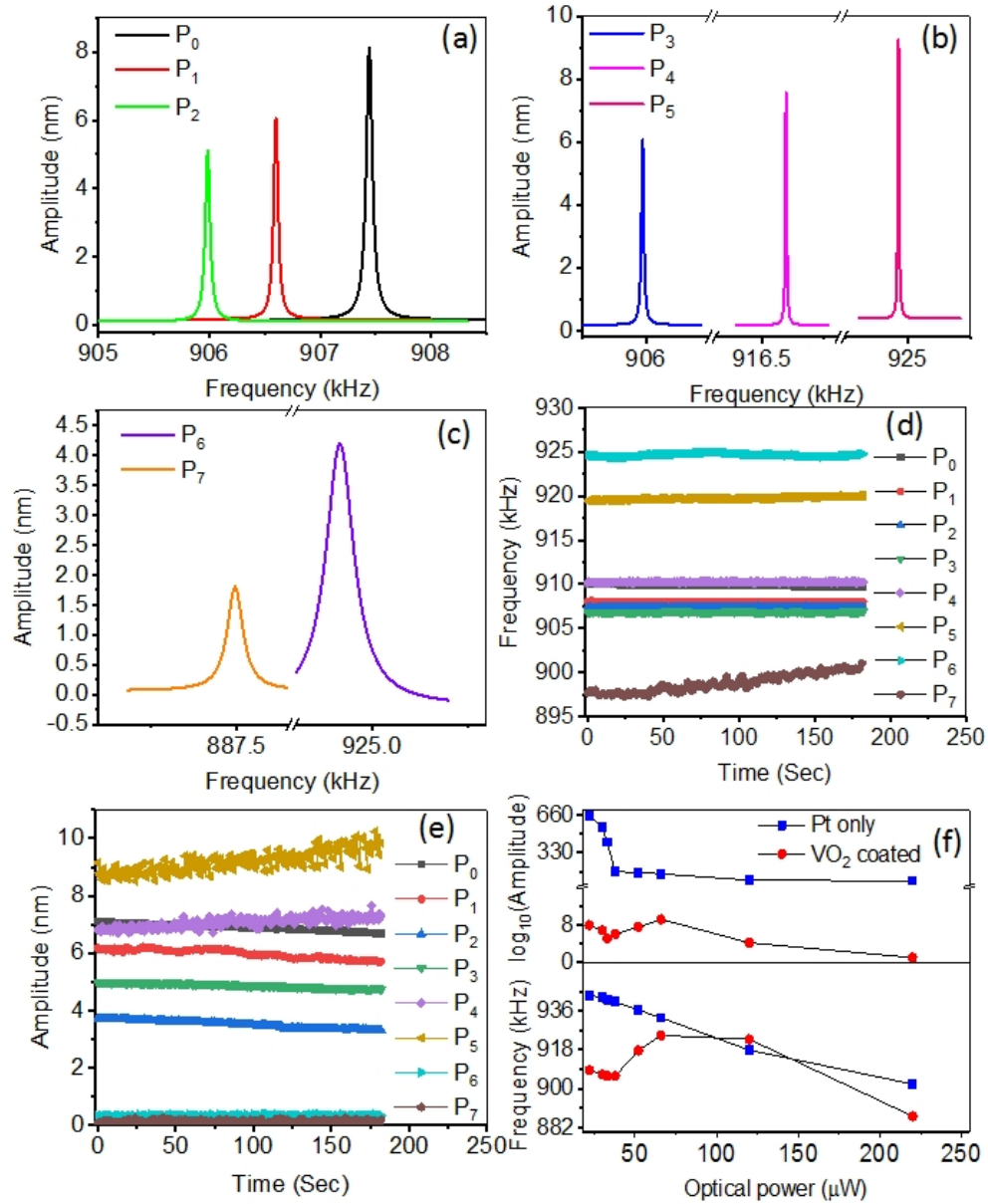


Figure 6.3: (a) FFT spectrum of resonance frequency of VO₂ coated microstrings for lowest pump and probe laser power P_0 , P_1 and P_2 levels. (b) FFT spectrum for powers P_3 – P_5 showed a huge increase in frequency with relatively small increase in amplitude suggesting that localized heating of VO₂ layer can trigger the crystal structure change from monoclinic to rutile phase which is likely cause additional stress leading to increased frequency of the string. (c) FFT spectrum for higher optical powers. Stability of resonator at a particular power was observed for 180 seconds for both frequency (d) and amplitude (e) drift as a function of time and at all optical power levels. (f) Shows a comparison between frequency and amplitude variation of uncoated and VO₂ coated strings as a function of laser power.

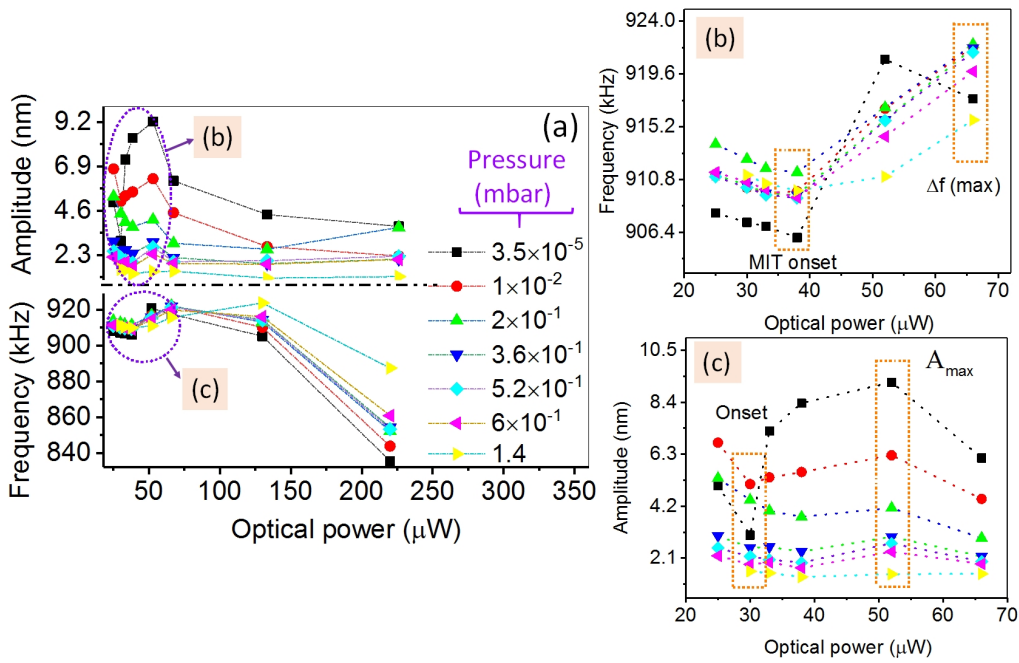


Figure 6.4: (a) Effect of pressure on magnitude of frequency/amplitude variations as a function of incident optical power. All pressures were measured for air flow into the vacuum chamber with a needle valve and standby ON mode of turbo pump at 300 rpm speed. The magnitude of increase in frequency and amplitude decreases with increasing air pressure. The decrease in frequency might be due to more heat been taken away by the gas molecules while decrease in amplitude could be because of additional damping introduced in the system. (b) and (c) represent the zoomed portions of (a) to visualize the optical power range up to 52 μW .

wavelength of external optical power.

Using red external laser, we observed a decrease in frequency for combined optical power of LDV laser and external laser between $32 - 67\mu W$ when the external power was turned ON. However, when the total optical power was raised to $97\mu W$, we saw a drastic shift in frequency of the strings as shown in Figure. 6.5 (a) and (c). We did not see any change in frequency for optical power less than $32\mu W$. In part (d) of fig. 6.5, we set the external power constant and started increasing the internal power using LDV internal laser power control. The exposure was for 10 sec interval and data was recorded continuously until 80 seconds. Frequency increase upon laser exposure was observed until the internal power was increased to level P_3 and it started decreasing for laser ON condition when internal power was increased to P_4 and beyond.

In case of pumping the system with green laser with wavelength of 520 nm and probing with LDV internal laser at its minimum power level (P_0 , 635 nm), we saw a decrease in frequency for a total power of $97\mu W$ as shown in Figure. 6.6(a). However when the internal laser power was increased to P_1 , the frequency behavior reversed with ~ 5 kHz increase in frequency when the external laser was turned ON and a change of ~ 3 kHz for ON/OFF cycles afterwards as shown in part (b) of Figure. 6.6. The change in frequency became smaller as the power of probe laser was increased to P_3 . The change was beyond the detection limit for power levels $> P_3$.

When the wavelength of the pump laser was decreased further, the string behavior changed. The resonance frequency of the string was found to drop by ~ 2 kHz when the system was exposed to a total power of $97\mu W$ as shown in Figure. 6.7. We did not see any change in frequency behavior for all power levels of probe laser from P_0 to P_7 . Now we did some time dependent study of frequency by continuously measuring the frequency of the resonator while setting the LDV power to level P_3 . After some time we saw a flip in frequency

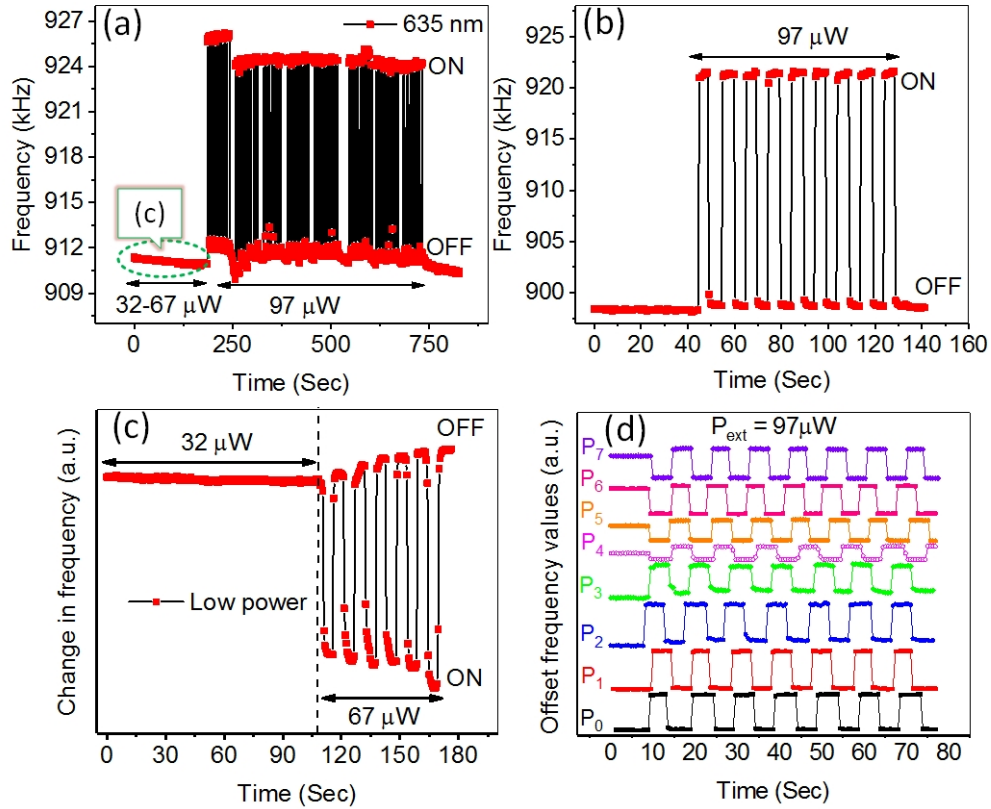


Figure 6.5: (a) Frequency response of VO₂ string with external optical power of 635 nm laser keeping the LDV laser at minimum P_0 . External power was regulated with an electronic controller. Total optical power includes the ambient and the minimum power of LDV laser which is $22 \mu\text{W}$. Response within $32\text{-}67 \mu\text{W}$ is zoomed in part (c) while response for optical power of $97 \mu\text{W}$ is shown in (b). (d) Shows vertically offset frequency response by keeping the external power constant at $97 \mu\text{W}$ and increasing the LDV power from $P_0 - P_7$.

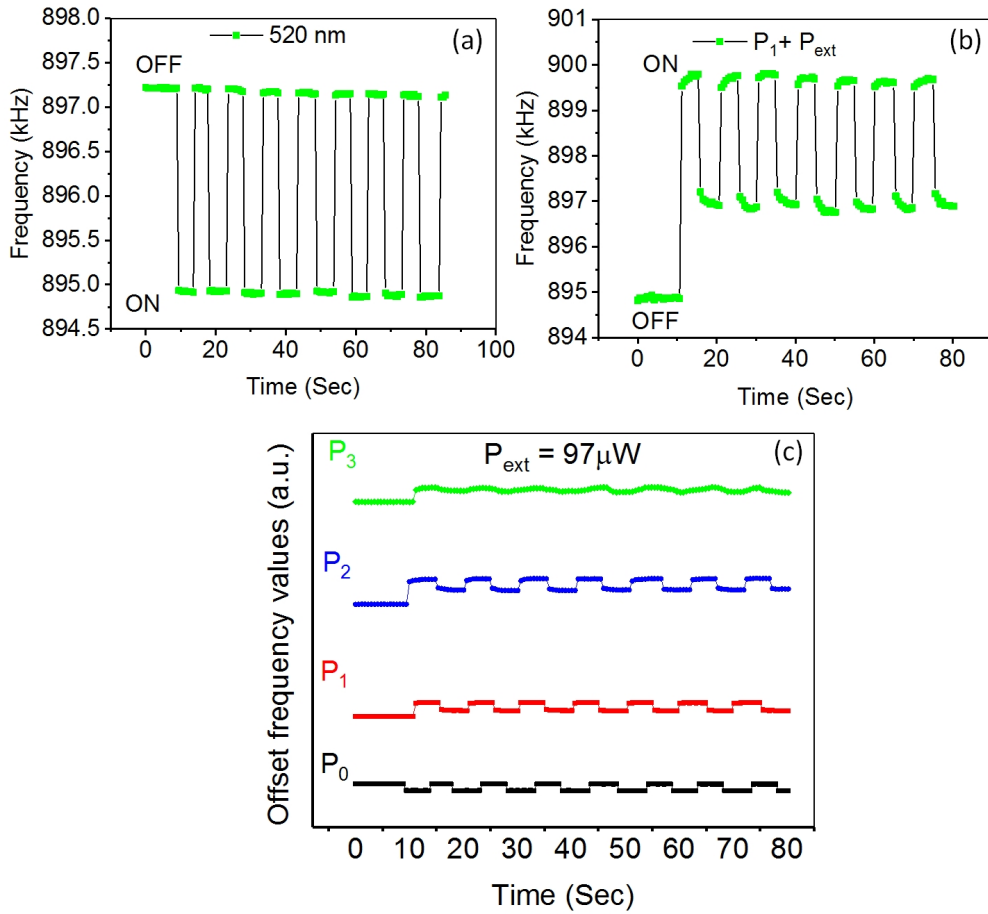


Figure 6.6: Frequency response with 520 nm external laser. (a) Response for a $97 \mu W$ power. Here we saw decrease in frequency as the power was turned ON. Upon switching internal power to level P_1 , a large increase in frequency was observed with high frequency state representing the ON and lower state representing the OFF status of laser (b). However we could only see observable change in frequency up to internal power level P_3 as the difference between ON and OFF state is practically the same for level $P_3 - P_7$.

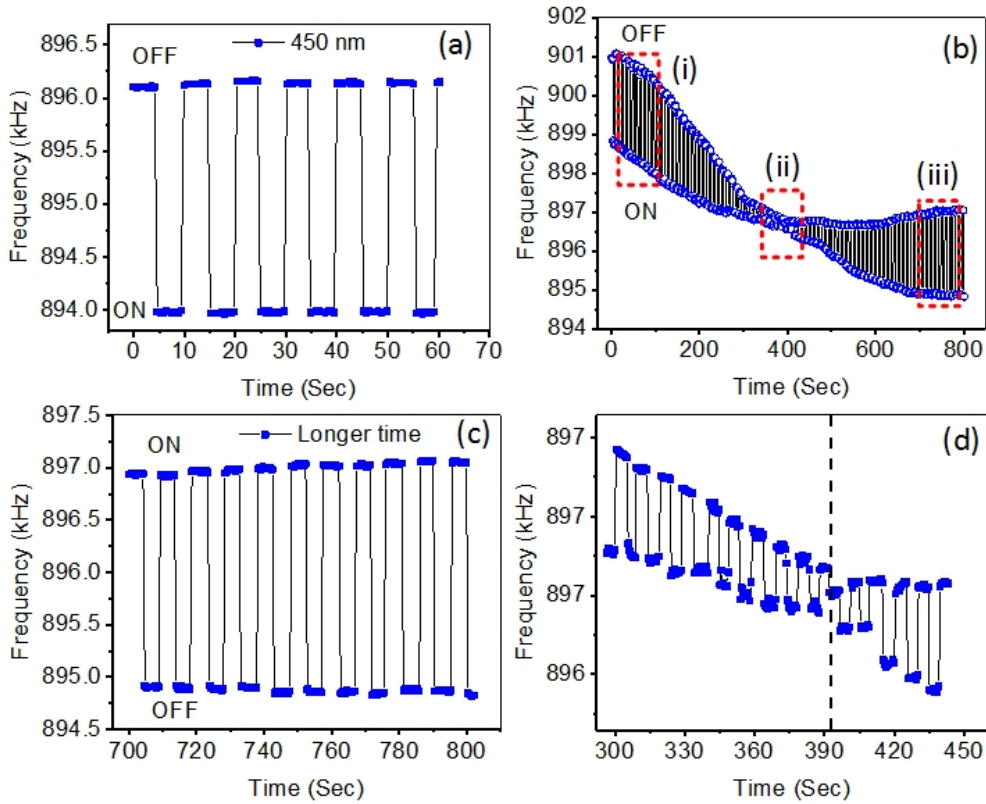


Figure 6.7: Frequency response for 450 nm (blue) external laser. We saw same trend for all internal LDV power values from $P_1 - P_7$ while keeping the external power to a maximum value of $97 \mu\text{W}$ (a). When the system was subjected to the constant maximum external power and internal power level P_0 for longer times (b), a transition from decreasing frequency with power happened and system responded opposite way above that transition (c). The system response reversed instantly around 390 seconds and an increase in frequency with laser being in ON state was observed (d).

with a crossover. Below that time, the frequency was dropped with laser being in ON state and opposite above that time which was around 400 seconds. The behavior can be explained by dividing the curve in three different regimes as shown in part (b) of Figure. 6.7. Depending on the absorption and reflectance of light from VO₂ layer and underneath Pt layer, the system took some time to trigger the localized transition. Region (ii) and (iii) of Figure. 6.7 (b) have been zoomed in in part (c) and (d) where a an increase in frequency (c) and a crossover around 390 seconds (d) is shown.

UV-Vis spectroscopy of VO₂ films deposited on Si may help us to understand the dynamics of resonators as a function of changing wavelength of the external light [142]. It has been shown recently that the absorption of light drops for VO₂ films deposited on Pt substrate as the wavelength of light increases from 300 nm to 500 nm [143]. There is a sharp increase in absorption for 635 nm laser while 520 nm lies towards the positive slope of the cusp. The reflectance of Pt also increases with increasing wavelength means portion of light transmitted through VO₂ layer will also reflect more in case of higher wavelengths causing more absorption of light in the VO₂ layer. This strong absorption will likely increase localized temperature and create zones of metallic VO₂ phase within the heated area and leading to lattice compression because of crystal structure change. The stress created will increase the resonance frequency of the strings. In case of green laser (520 nm), the absorption is weak as compare to 635 nm but good enough that the transition can be triggered by just increasing the internal LDV power to one step up. Since blue laser is very weakly absorbed by VO₂ layer so we do not have enough energy available at the focus point of the laser and it would be time dependent phenomena where the transition happens but after accumulation of energy while system kept under optical exposure for some time.

6.5 Conclusion

Here we have investigated the tuning of mechanical resonance frequency of VO₂ coated microstrings with varying optical power and wavelength. We demonstrated that highly focused beam of laser can locally trigger the insulating to metal state regions in the heated area. This localized transition can cause lattice compression because of crystal structure change from monoclinic to rutile phase. The resonance frequency decreases with increasing optical power below a critical power ($\sim 50 \mu\text{W}$) which is expected increase in temperature decreases the modulus and makes the resonator soft. Above a critical optical power but below a certain power level, the resonance frequency was increased which is likely because of MIT of VO₂ layer causing an additional stress on the resonator and an increase in resonance frequency. If the optical power is very high, the resonance frequency starts decreasing again which could be because the most of heated region is already transformed to metallic state and increasing the optical power will consider rutile crystal structure as a starting point where after the transformation, additional heat will cause the stiffness to decrease and hence the associated resonance frequency as well. Drift in resonance frequency was studied by continuously measuring the resonance frequency for 80 seconds while the system was exposed with external laser. A positive drift in frequency was observed at laser power level P_7 suggesting that nearby regions might also be transforming to metallic phase and adding stress on the resonator if the system was exposed for a long time. A positive drift in amplitude of vibration was seen for a laser power P_5 suggesting some sort of actuation mechanism because of optimum power for transition. Pressure dependent frequency and amplitude variations suggest that the convection heat losses suppress the magnitude of frequency and amplitude increase but the onset remained unchanged. The increase in frequency was only observed for VO₂ coated microstrings in comparison with Pt coated

strings and TiO_2/VO_2 coated resonators of similar dimensions. The resonance frequency was also tuned as a function of wavelength by exciting the system with external optical source and measure the mechanical frequency with LDV laser. Because of good absorption of 635 nm (1.95 eV) light, the increase in frequency was observed for $97 \mu\text{W}$ of total optical power. As the internal LDV power was increased, the resonance frequency was found to decrease after the internal power level P_4 . The decrease in frequency was observed for lower optical powers which is quite consistent with pump and probe with same laser done earlier. As the energy increased to 520 nm or 2.38 eV, we observed a decrease in frequency for exactly the same power i.e. $97 \mu\text{W}$. However, the trend reversed with increasing the probe laser power level to P_2 . We saw a decrease in frequency for all power levels $97 \mu\text{W} + P_i$ ($i=1,2,\dots,7$) for blue laser. Leaving the exposure ON for 390 seconds lead to a cross over in frequency when the frequency started to increase when the laser turned ON. These observations open new avenues to use VO_2 coated resonators for modulate the frequency of resonators with varying optical power and frequency.

6.6 Acknowledgements

This work was supported by the Canada Excellence Research Chair (CERC) program (ID: SF0926 and grant number: RES 0006296). The authors would like to acknowledge the characterization facilities at the University of Alberta nanofab, as well as Ms. Rosmi Abraham for useful discussions.

6.7 Supplementary data

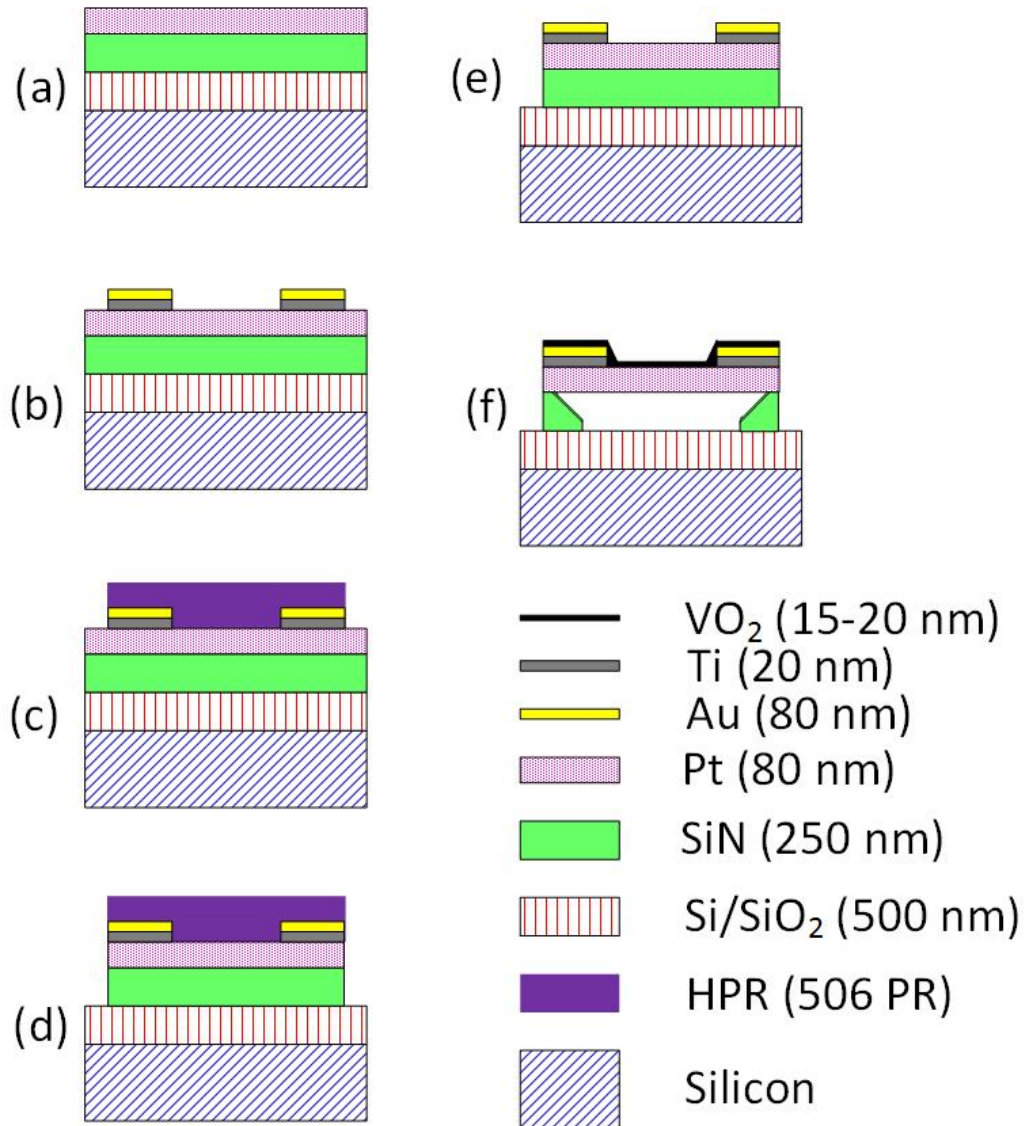


Figure 6.8: Process flow for fabrication of VO₂ coated microstring resonators. Mechanical response of released devices was recorded using LDV before and after depositing VO₂.

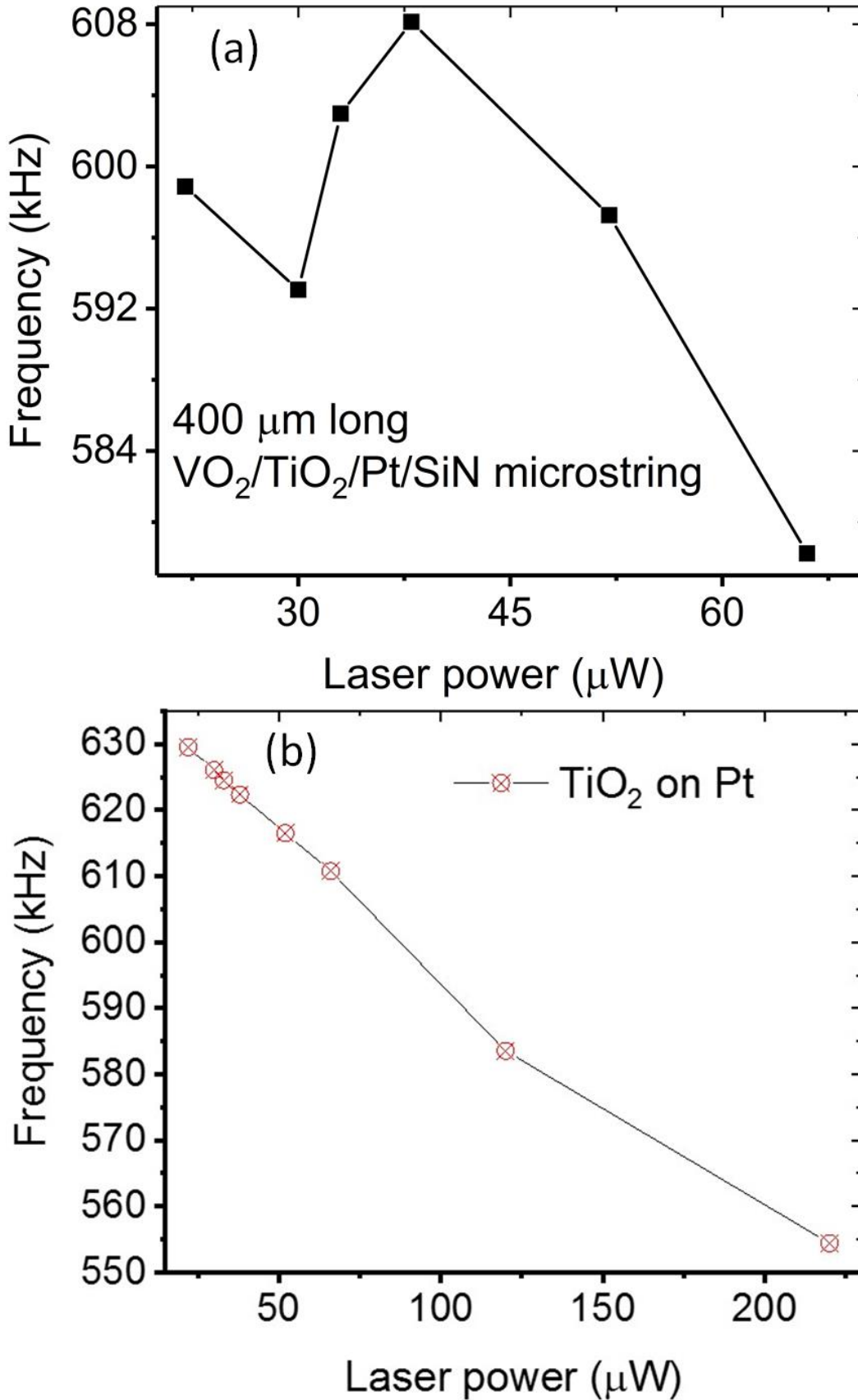


Figure 6.9: Optical response of a ¹¹⁸doubly clamped string coated with VO_2/TiO_2 shown in (a) and only TiO_2 coated on Pt.

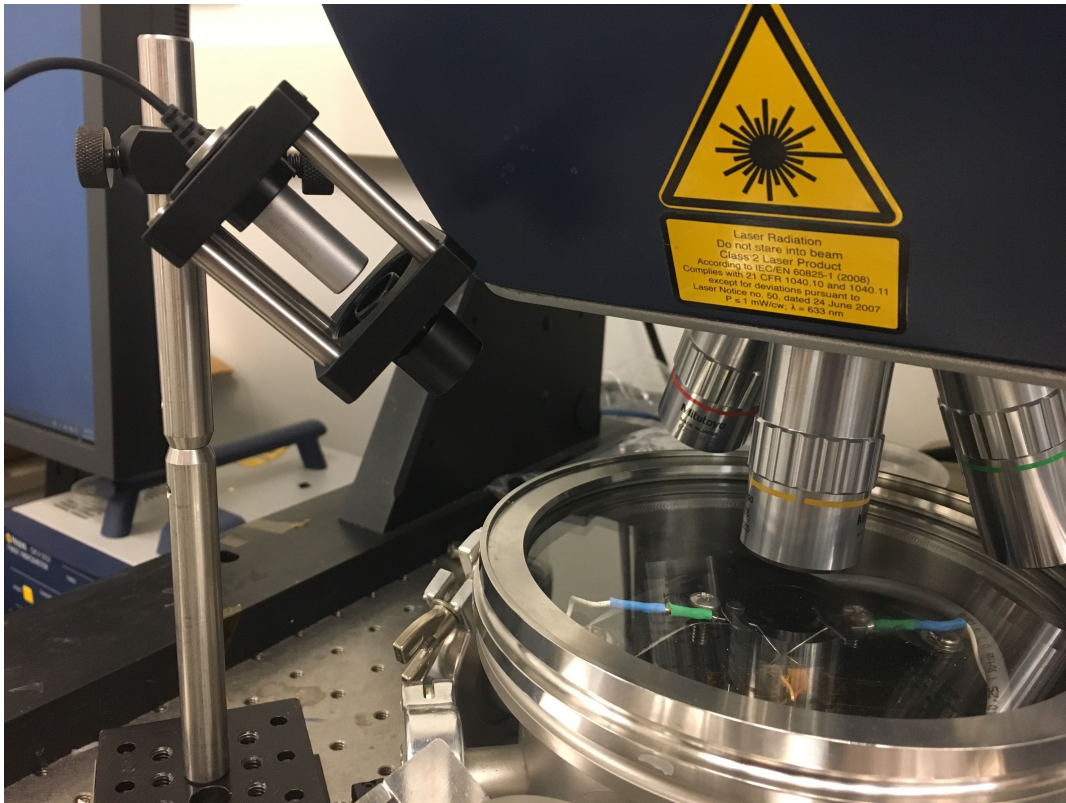


Figure 6.10: Using the external light as a pump while probing the mechanical response with LDV laser.

Chapter 7

Spatial frequency tuning of VO₂ resonators with opto-thermal excitation

7.1 Abstract

Tuning mechanical frequency of MEMS and MOEMS devices by integrating the conventional silicon based devices with functional oxides has become very important recently. Because of insulator to metal transition in VO₂, the change in mechanical modulus, optical absorption, thermal expansion of VO₂ can provide a pathway to bi-directional frequency tuning of the MEMS resonators. While properties of VO₂ have been extensively studied for various applications using thin films, heterostructures, and electronic switches, there are minimal efforts put on frequency tuning of MEMS with optically driven MIT in VO₂. Here we demonstrate that VO₂ microstrings have bi-directional spatial frequency tuning which is not only dependent on the irradiated power but also on the spatial variation along the direction of the string. Depending upon how much power is retained and lost by the system through two anchor points of the resonator, the response of VO₂ coated resonator is very different

as compare to conventional Si based resonators.

7.2 Introduction

Micro and nano electromechanical systems (MEMS/NEMS) are a diverse topic of research for scientific community because of their small size, compact geometrical shapes, high resolution and sensitivity, functionality and selectivity along with low power consumption and cost [144–146]. These resonators can be fabricated in different shapes and sizes using various microfabrication techniques. These resonating systems have been used for advanced technological applications like mass and force sensing, chemical & biological sensing, cooling, environmental monitoring and quantum measurements [147–151]. Despite proven applications in many areas of technological significance there are still challenges in tuning the frequency of micro nano resonators. The most important characteristic of any resonator is its fundamental frequency and quality factor. Tuning of fundamental resonance frequency of the resonator is important because it can be used to compensate the shift in frequency caused by the changes in temperature, pressure, humidity, mass, electric and optical fields [152].

One key aspect of tuning mechanical frequency of resonator is timescale. Ultrafast tuning of frequency is important for signal processing, detection with a challenge of signal tracking and rapidly switching the transmitting signals to several frequency channels [153]. One way of obtaining the tuning is controlled fabrication process by changing the structural dimensions of the resonator [154, 155]. Tuning of mechanical frequency is important for future applications of MEMS/NEMS resonators in high or ultra-high frequency regimes and fast timescales. Vanadium dioxide (VO_2) is a correlated oxide of transition metal which demonstrates a reversible phase transition

close to room temperature (T_c) of 340 K [96]. This phase transition not only changes the crystal structure but also electrical conductivity, optical absorption, and coefficient of thermal expansion. At room temperature, it shows semiconducting properties with a band gap of ~ 0.6 eV [98, 156]. This phase transition can be excited thermally, optically and electronically. The optically excited, mechanically detected phase transformation makes it a good candidate material for tuning frequency and photodetection [157]. This transition has proven applications in uncooled bolometers [16, 99, 158], gas and strain sensing [55, 111], memory devices [102, 103], and smart windows [107, 108]. Recently, phase change materials (VO_2) have been used to demonstrate strong frequency tuning abilities in MEMS [159]. Another study showed that insulator to metal transition in VO_2 can be used to dynamically tune metamaterials in terahertz frequencies by integrating VO_2 material in the hybrid structure. This lead to ultrafast modulation of resonator in THz regime [160]. Silicon cantilevers coated with VO_2 showed shift in resonance frequency upon heating [161]. The study demonstrated that the magnitude of change in frequency of the resonating cantilever was found to be dependent on crystallite size of the deposited film on Si.

Since the mechanical response of VO_2 coated resonators depends on joule heating (thermal and optical), or Poole-Frenkel effect ([162]), it is possible to tune the mechanical frequency based on localized heating and heat flux leaking from ultrathin VO_2 films coated on a doubly clamped resonator. In this study, we demonstrated that the resonance frequency of VO_2 coated microstrings can be controlled via a spatial variation of optically heated regions along the string. We used a pump and probe laser built in LDV polytec system to excite a localized transition with highly focused laser beam (635 nm) with and without applying external electric field across the resonator. We showed that a highly focused beam of laser can transition a localized region from insulating to metallic phase which can be detected by the change in

mechanical resonance frequency. We observed a converse effect on resonance frequency of VO₂ coated string as compare to the same string when uncoated. The minimum measured power of the pump and probe laser which caused the flip behavior in frequency was 52 μ W. In order to observe this response we divided the string into 15 equidistant points along the string between two anchors. This was done using LDV software control which would allow the laser to turn ON and expose at the pre set point.

7.3 Experimental process

Fabrication process of the strings has been shown in Fig 6.8. Once released, strings were characterized by measuring their resonance frequency and amplitude of vibration at resonance. VO₂ films were deposited onto the strings with pulsed laser deposition (PLD) using and V target (99.9 % purity, American Elements) and optimized deposition conditions. The distance from target to the substrate was set at 31 mm. A high energy KrF ($\lambda = 248$ nm) excimer laser (Coherent, GmbH) with a fluence of 2.6 J/cm^2 was used to evaporate the material and deposit it onto the substrate which was held at a constant temperature of 600 °C. The laser pulse repetition rate was set to 10 Hz and deposition was done for 15 minutes which lead to a film with a thickness of VO₂ ranging between 15-20 nm as reported in our previous work [1]. In order to characterize the phase, we used X-ray diffraction (XRD) of thin films Rigaku Ultima IV diffraction system. Scanning helium ion microscope (Zeiss Orion NanoFab HiM w/ Ga-FIB (Trinity)) was used to obtain high resolution images of both coated and uncoated microstrings without doing any metallic coating on the strings. Tapping mode AFM was used to analyze surface roughness and grain size of the deposited film.

Laser Doppler Vibrometer (LDV) is one state of the art technique which can be used for probing and exciting the MIT in VO₂ films deposited on Pt/SiN

microstrings by measuring the resonance frequency of the films. High resolution frequency and amplitude measurements were made using LDV by placing the strings into a high vacuum chamber. Microchip containing all resonators, piezo and Pt-1000 temperature sensor were fixed with peltier element in close proximity. The other side of the peltier was connected with a heat sink. The resonance frequency was continuously measured with each data point measured in 0.5 seconds while temperature was cycled between 25-90 °C at the an approximate rate of 2 °C per minute by driving the peltier element with a BK Precision 9183 power supply with a software controlled constant current and varying voltage scheme. The temperature of the system was measured with a Keithley 197 multimeter interfaced with LabView. Using the simulation tool of LDV software, the coated string was divided into 15 parts each separated by 13.3 μm in order to understand the variation of frequency with lateral movement of the heat source. The experimental set up is schematically shown in Figure. 7.1. The suspended and released part of the coated string was divided into 15 equidistant sections as shown in Figure. 7.1 (a) . Laser light of 635 nm wavelength was used to pump and probe the system dynamics. The blue color of VO₂ film is designated for insulating phase while the circular red portions on the string are designated as portions in conducting rutile phase once get exposed with the laser. Scanning helium ion microscope images are shown in Figure. 7.1 (d) and (e) and polycrystalline VO₂ structure was visible at 200 nm resolution. The optical image of a 400 μm long string is shown in Figure. 7.1 (c) because of a better image quality but all the experiments were done on 200 μm string.

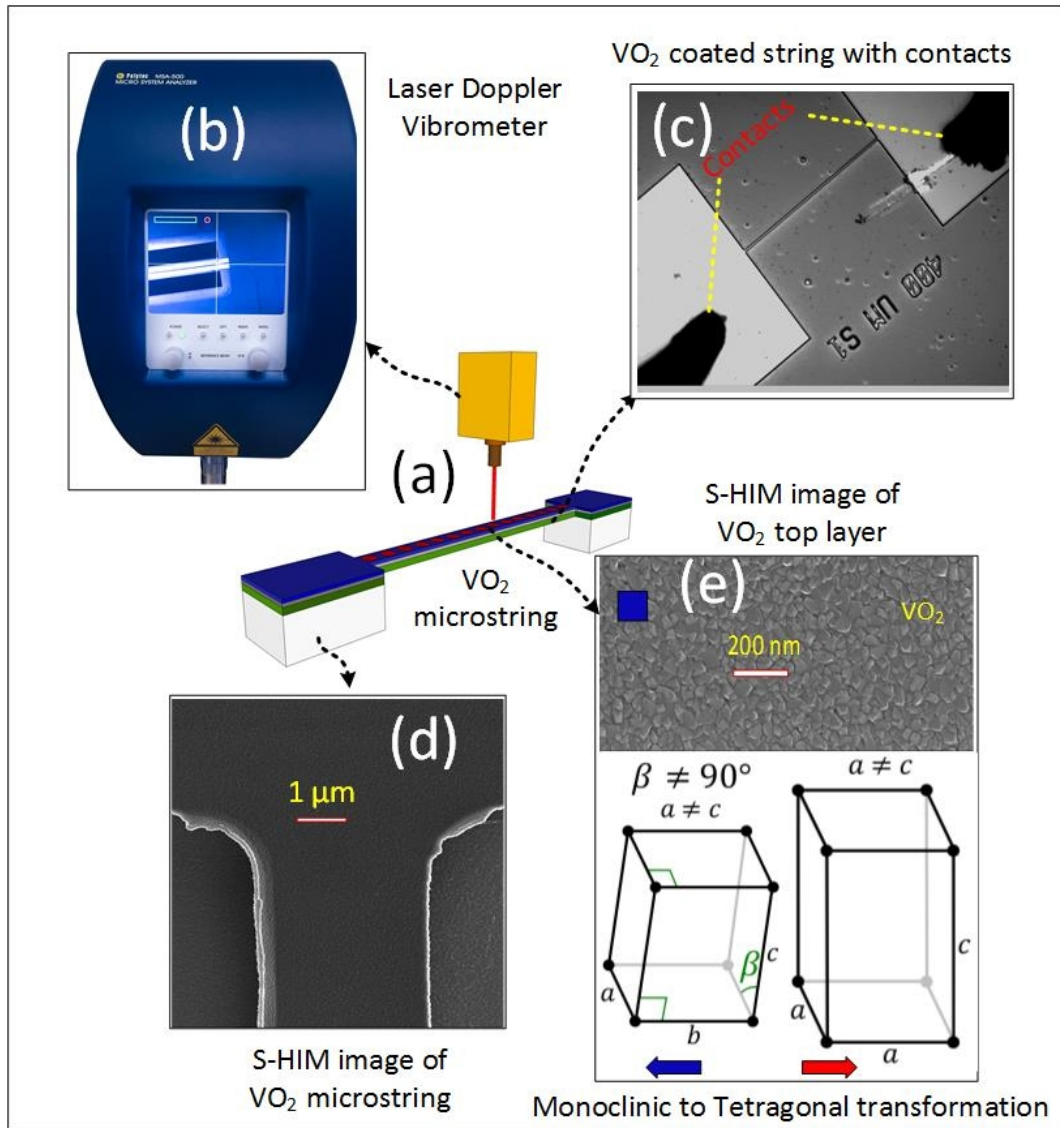


Figure 7.1: (a) Microstring resonator with frequency being measured as a function of spatially distributed scanning points along the lateral direction (b) Polytec MSA 500 vibration measurements, (c) optical image of doubly clamped strings with electrical contact probes (d) Scanning-HIM image of VO₂ coated resonator close to its one anchor point, (e) high resolution image taken at the center of the resonator showing VO₂ crystallite with cartoon showing red label for tetragonal (rutile) phase and blue region corresponding to insulating monoclinic phase of VO₂ film deposited on the string.

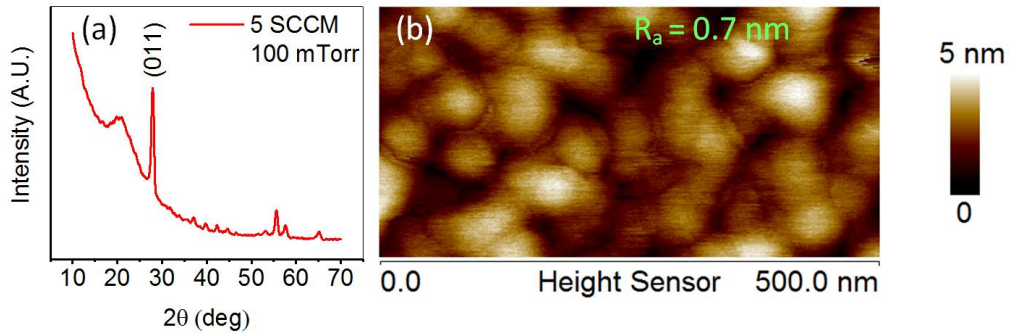


Figure 7.2: (a) XRD analysis polycrystalline VO₂ deposited on Pt/Si/SiN strings with optimized oxygen flow rate of 5 SCCM and chamber pressure of 100 mTorr (b) Tapping mode AFM image of 250 nm × 500 nm area showing island type formation of VO₂ and a smooth film of average surface roughness of 0.7 nm.

7.4 Analysis of experimental data

7.4.1 Optically induced frequency modulation

Detailed microfabrication information of the microstrings resonators used in this study is provided in the supplementary information 7.6. After deposition of VO₂ film on resonators, crystalline phase of the film was identified with XRD. The room temperature monoclinic phase was identified with a large intensity peak from (011) plane at 2θ value of 29.88° Fig. 7.2 (a). Microstructural analysis was carried out using tapping mode AFM and average surface roughness of the polycrystalline VO₂ was calculated to be 0.7 nm as shown in Fig. 7.2 (b).

Resonance frequency in first mode of uncoated and coated VO₂ resonator is shown in Fig. 7.3 (a). A frequency drop of 7 kHz was observed when VO₂ was deposited onto the resonator while a frequency increase of 28 kHz was observed when VO₂ coated string was heated to 66 °C. The decrease in frequency reflects addition of mass onto the resonator while the increase in frequency corresponds to addition of tensile stress on the surface of the resonator because of the top layer transformation from monoclinic to ru-

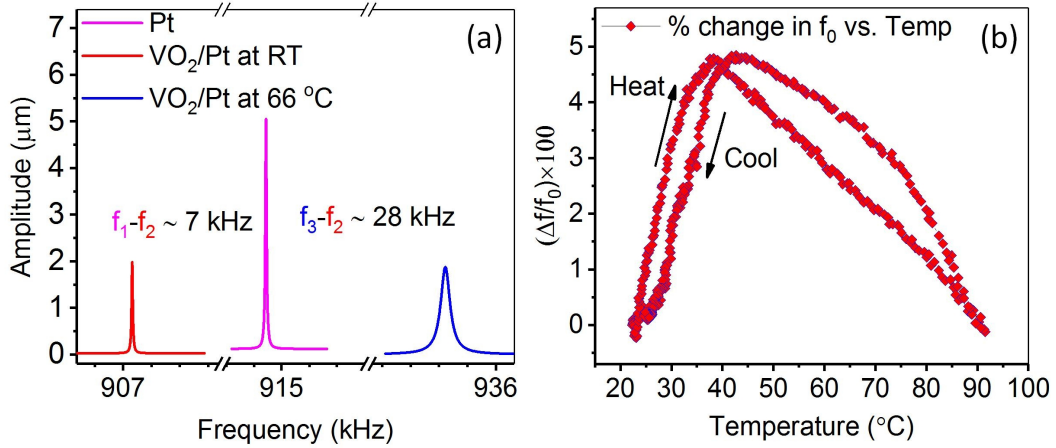


Figure 7.3: (a) FFT spectrum of uncoated microstring resonator in first mode, VO₂ coated resonator in first mode at room temperature and at 66 °C. (b) Temperature dependence of frequency variations during thermal cycling of resonator from room temperature to 92 °C with control heating/cooling.

tile crystal structure. This transformation can cause lattice compression and hence addition of stress on the resonator. Detailed description of resonance frequency variation of VO₂ deposited strings is given in our previous work [163]. Temperature dependent frequency variation of the resonator was studied by controlled heating of the resonator with peltier element and measurements of temperature with Pt-1000 sensor. The frequency dropped slightly for a lower temperature values and started increasing as temperature reached to 26 °C and reached to a maximum value around 40 °C. Beyond this temperature, frequency started dropping again. The peak of frequency can be correlated with complete insulator to metal transition of the VO₂ layer. The decrease in frequency may be related with decrease in modulus of conducting phase of VO₂ when heated after it transitioned completely from insulating to metallic phase.

Variation of resonance frequency and amplitude was studied as a function of pump and probe optical power (Fig. 7.4). LDV built in laser was used for opto-thermal heating (the absorbed part of the light) and probe the mechanics

(reflected part of light). The resonance frequency decreased for LDV power levels $P_0 - P_3$ as the laser spot moved from one anchor to the center and minimum of the frequency was observed close to $100 \mu\text{m}$ (Fig. 7.4(a)). The minimum shifted towards lower frequencies as the laser power increased from P_0 to P_3 . The frequency is highest close to the anchor points as a large part of the heat source is close to the heat sink (anchor point) which would allow a large portion of the heat to leak out to the sink instead of diffusing through the string. The small amount of heat diffuses through the string towards the other anchor point which causes a decrease in the modulus of the material and hence a decrease in frequency. However when the heat source is placed at the center of the resonator, the symmetric distribution of flow of heat on both sides results as all the heat been consumed in heating the material and lowering its modulus. That is why we observed the lowest frequency when we heated the string at the center. The shift in minimum of the curve as we increase the optical power is because more heat is added to the system at P_3 than at P_0 .

The amplitude of vibration was maximum at the center of the resonator which was expected as we are operating the resonator at its first resonance mode (Fig. 7.4(b)). This amplitude increased with increasing of optical power because the system has to vibrate with larger amplitude in order to utilize the extra energy and attain a thermodynamic equilibrium. Since the heat flux to the sink is constant for each power level, the excessive heat in the system would cause the system to vibrate at higher amplitudes.

For optical powers higher than P_4 , we saw a very different response as shown in Fig. 7.4(c). We observed an increase in frequency as the optical exposure was scanned through the equidistant points closer to the center along the string for power levels P_4 to P_6 . For power level P_4 , the frequency decreased up to $\sim 65 \mu\text{m}$ from the anchor point and started increasing up until $135 \mu\text{m}$ from the left anchor point. In case of power level P_5 , the onset of frequency

increase shift slightly to the left and the magnitude of increase in frequency was also increased. The largest increase in frequency ~ 20 kHz was observed when the power level was increased to P_6 . The onset was also shifted very close to the anchor point at about $26.6 \mu\text{m}$ from the left anchor point. For highest available optical power P_7 ($220 \mu\text{W}$), the increase in frequency was only seen for point very close to the anchor and a large decrease in frequency was observed as we scanned the optical source through the center of the resonator.

The increase in frequency can be correlated with localized insulator to metal transition in VO_2 film coated on the resonator. The resonator behaves normally as expected for lower optical powers but the transition from insulating to metallic phase adds surface stress on the resonator which would increase its resonance frequency. Depending upon how many localized grains transition to metallic state, the magnitude of stress on the string increases and hence its frequency. The transition also depends on the location of the power source along the string as heat diffuses to sink when the source is close to the anchor point. When the localized heating spot gets too warm, the heated region may transform completely to conducting phase with a part of the heat supplied and remaining part may just heat the conducting state further causing a decrease in modulus of tetragonal (rutile) phase and making the string softer and hence decreasing its resonance frequency as observed for optical power level P_7 .

The peak of amplitude of vibration was observed to decrease for power levels P_4 to P_7 which is opposite of what we observed for P_0 to P_3 . The amplitude however increases as we move the heat source towards the center. The later can be explained with the fact that increased optical power will increase the amplitude as the system has to equilibrate at its lowest energy state by utilizing the excess power in increasing the amplitude of vibration. The decrease in the peak amplitude is can however be explained by the fact that

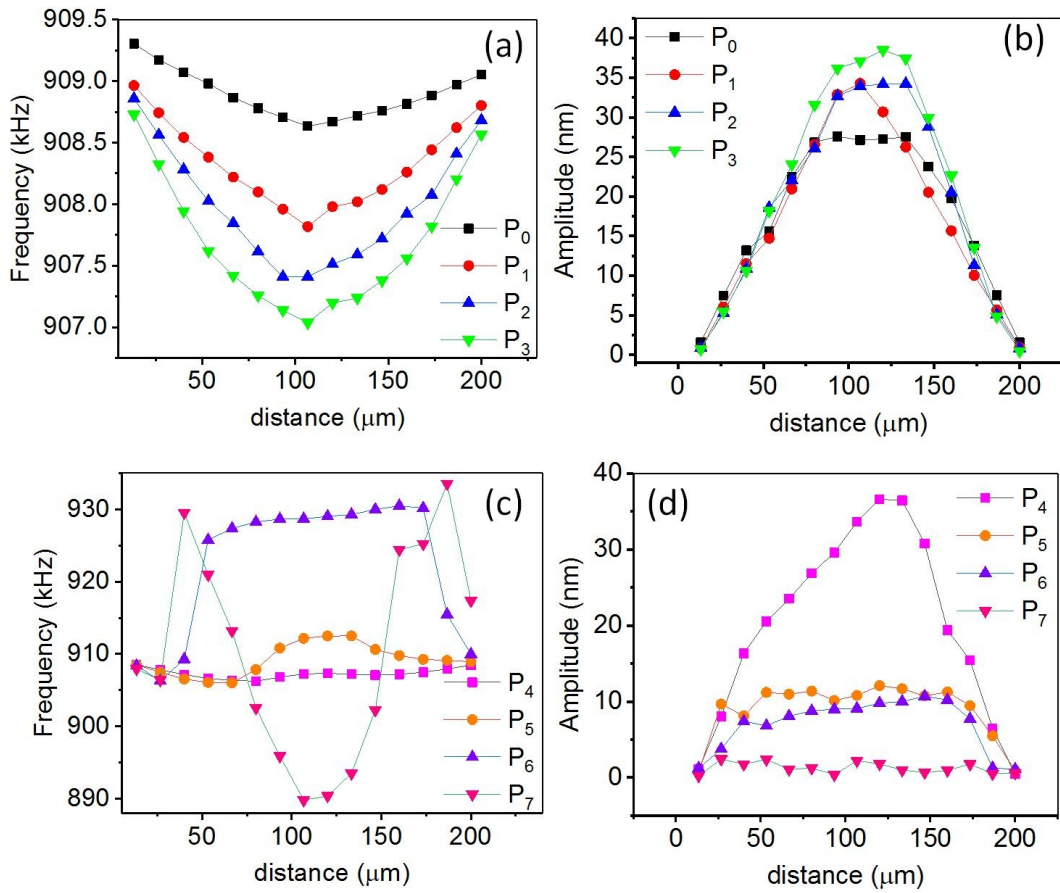


Figure 7.4: (a) Frequency variation of VO₂ coated resonator when at different spatial positions along the string as a function of incident laser power ($P_0 - P_3$). Two extreme points are close to the anchors of the beam. (b) Amplitude of vibration measured at fifteen equidistant points along the string ($P_0 - P_3$). (c) Frequency variation at fifteen equidistant points along the strings for laser power levels $P_4 - P_7$ and (d) amplitude variation for same power levels.

addition of tensile stress on the resonator because of localized Insulator to metal transition forces the the resonator to vibrate at small amplitudes. We observed a tri-directional frequency tuning of VO₂ coated resonator with expected frequency decrease for lower optical powers, a frequency increase when the localized heating caused a change in crystal structure of the material and a decrease in frequency for highest optical powers when the transitioned system was heated further.

7.4.2 Electro-optic frequency modulation

Resonance frequency variation along the direction of the string was also studied with combine electrical and optical excitation. We developed a vacuum probe station in order to apply electric field across the the string resonators. The laser was set to its minimum level i.e. P_0 so that only the effect of electric field may be explored. The suspended part of the resonator was divided into fifteen equidistant points. Resonance frequency was measured as a function of ac electric field intensity. The resonator showed bi-directional frequency tuning below and above a critical voltage as a function of lateral distance from the anchor points. The schematic of this study along with results for both lower and higher electric voltages is shown in Fig. 7.5. Resonance frequency was found to decrease with both positive and negative cycle of the electric field for lower electric fields up to 200 mV as shown in part (b) of Fig. 7.5. This is normally expected for Si based resonators as the increasing field causes increased dissipated power, so called joule heating effect. The increase in temperature (not measured here) is probably not enough to cause the top VO₂ layer to transition so the dominate effect comes as a result of decrease modulus of the resonator which decreases the stiffness and hence the resonance frequency. For higher voltages i.e. 300 mV and 400 mV, the resonance frequency showed a reversed behavior. In case of 300 mV, the frequency increase was lower close to the anchor points and higher when the laser was shined at locations close to the center with a maximum frequency increase observed when the light was at location 7 (Fig. 7.5 (c)). It is worth noting that frequency first decreased up to a certain voltage level and then started increasing at a particular value of electric field. The former can be explained by the fact that combined optical and electrical power close to the center leads to higher temperature rise leading to localized phase transition in VO₂ which can lead to lattice compression and a resultant increase in resonance frequency. The later is expected as the resonator behaves normally

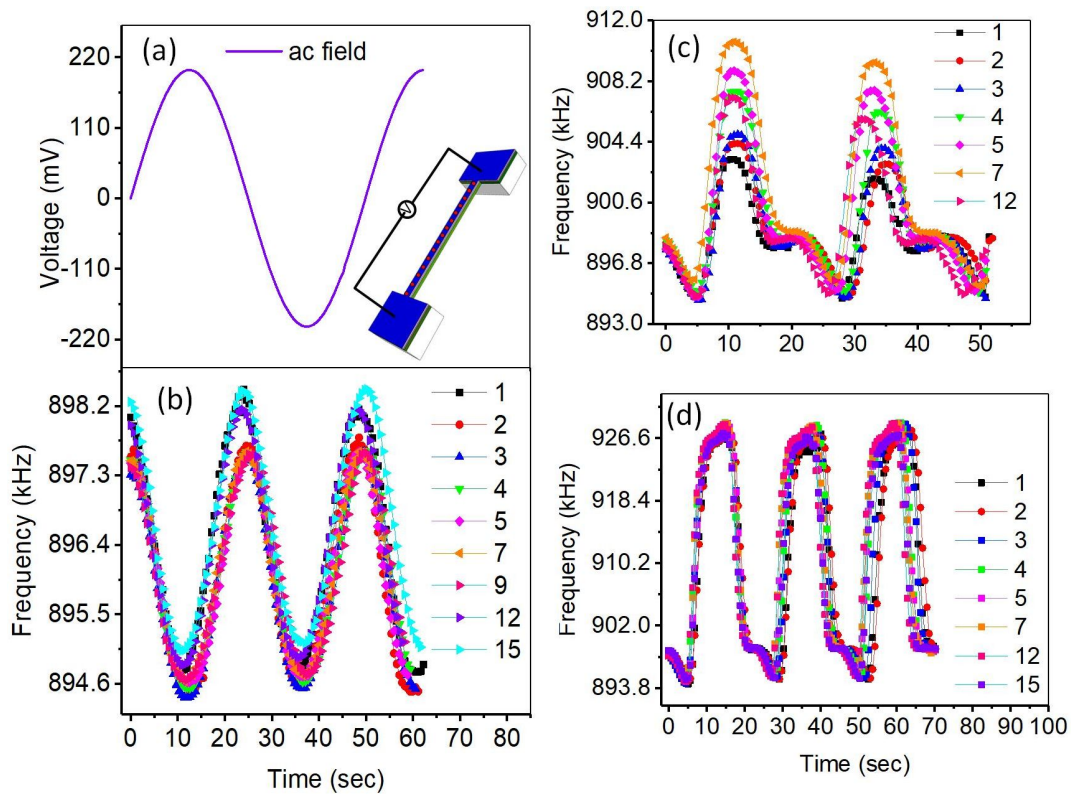


Figure 7.5: (a) Schematic of VO₂ coated resonator with 15 equidistant points along the lateral direction and electrical contacts. (b) Variation of mechanical resonance frequency at different locations as a function of ac signal of 200 mV applied across it. (c) Frequency response of resonator for 300 mV signal, (d) frequency response for a 400 mV signal.

below a critical field. The magnitude of this decrease in frequency reduced along with a large increase in frequency above the critical field when the applied voltage was increased to 400 mV. The peak amplitude of mechanical frequency increase was also found to be at the same level. At this point, most of the temperature rise can be correlated with joule heating not the optical power. The heating is probably good enough to create a transition in the whole film of VO₂.

7.5 Resonance frequency shift caused by optical and electrical heating

The effect of optical power on resonance behavior of VO₂ coated string can be represented by Gaussian distribution of the incident laser power [164]. Consider R_r be the reflectivity, L be the length and w be the width of the top layer of the resonator then the absorbed power at different intensities can be calculated by following equation.

$$P_{abs} = (1 - R_r) \int_{-w/2}^{w/2} \int_{-L/2}^{L/2} I_{max} \exp \left[-\frac{2(x^2 + y^2)}{r_0^2} \right] dx dy \quad (7.1)$$

where I_{max} is the maximum intensity of light, r_0 is the radius of the laser spot. The heat transport along the top layer of the resonator can be essentially estimated to be one directional assuming negligible heat transfer across different layers of the resonator.

$$\frac{\partial T(x, t)}{\partial t} = \frac{\kappa_t}{\rho_p c_p} \frac{\partial^2 T(x, t)}{\partial t} + \frac{P_{laser}}{\rho_p c_p L w h} - 2 \frac{(w + h) \alpha_H}{\rho_p c_p w h} [T(x, t) - T_0] \quad (7.2)$$

where L , w and h are length, width and thickness of the resonator and K_t is thermal conductivity, ρ_p is average density, c_p is heat capacity and α_H is heat

transfer coefficient of the resonator. The change in temperature is expected to cause a a localized solid-solid phase transition of VO₂ film which will eventually change the resonance frequency. Stress induced resonant change in first mode with optical excitation is given by. [165].

$$f_0 = \frac{\pi d}{16\sqrt{3}L^2} \sqrt{\frac{E}{\rho}} \sqrt{1 + \frac{11.6}{\pi^2} \frac{L^2}{Ed^2} \sigma} \quad (7.3)$$

where E Young's modulus and σ is the stress generated because of lattice compression. Same mechanism can also be created with electric field where instead of optical power, joule heating is dominant mechanism to raise temperature of the string. Stress dependent resonance frequency of the electrothermally excited VO₂ resonator can be described by [154].

$$f_\sigma = f_0 \sqrt{1 + \frac{\sigma L^2}{3.4Ew^2}} \quad (7.4)$$

where f_0 is the initial resonance frequency of the resonator.

7.6 Conclusion

Here we presented localized heat and thermal conduction dependent bi-directional tuning of VO₂ microstrings. Depending upon critical optical power and critical electric field, spatial variation of optical heat source along VO₂ resonator resulted as different pattern of frequency variation compared to conventional silicon based devices. For lower optical powers from 22-38 μW , the resonance frequency was highest close to the anchor points and lowest at the center because of proximity of heat source with the heat sink causing a large amount of heat transfer to the sink close to anchor points and equal amount of heat transfer on both sides of the string when heat source was placed close to the center of the string. The resonance frequency at the center was least for highest optical power of 38 μW . The amplitude of the string for

low optical powers increased close to the center of the resonator up to $38 \mu\text{W}$ as the system had more energy to force the resonator to vibrate with higher amplitudes. The response got different for intermediate optical powers where the resonance frequency started increasing when the laser heat source was moved close to the center. The maximum increase in frequency was $\sim 20 \text{ kHz}$ which was observed for optical power of $120 \mu\text{W}$. The highest power caused an increase in frequency close to the anchor point and large drop in frequency close to the center of the resonator. Frequency tuning was demonstrated by applying electrical field across the resonator. The large frequency increase can be related with insulating to metallic state transition accompanied by a large change in electronic thermal conductivity but not a great change in phonon thermal conductivity. The resonator is good conductor of electrical charge but a bad conductor of heat above the transition leading to large amount of heat dissipation at the localized point and causing a decrease in frequency.

7.7 Supplementary information

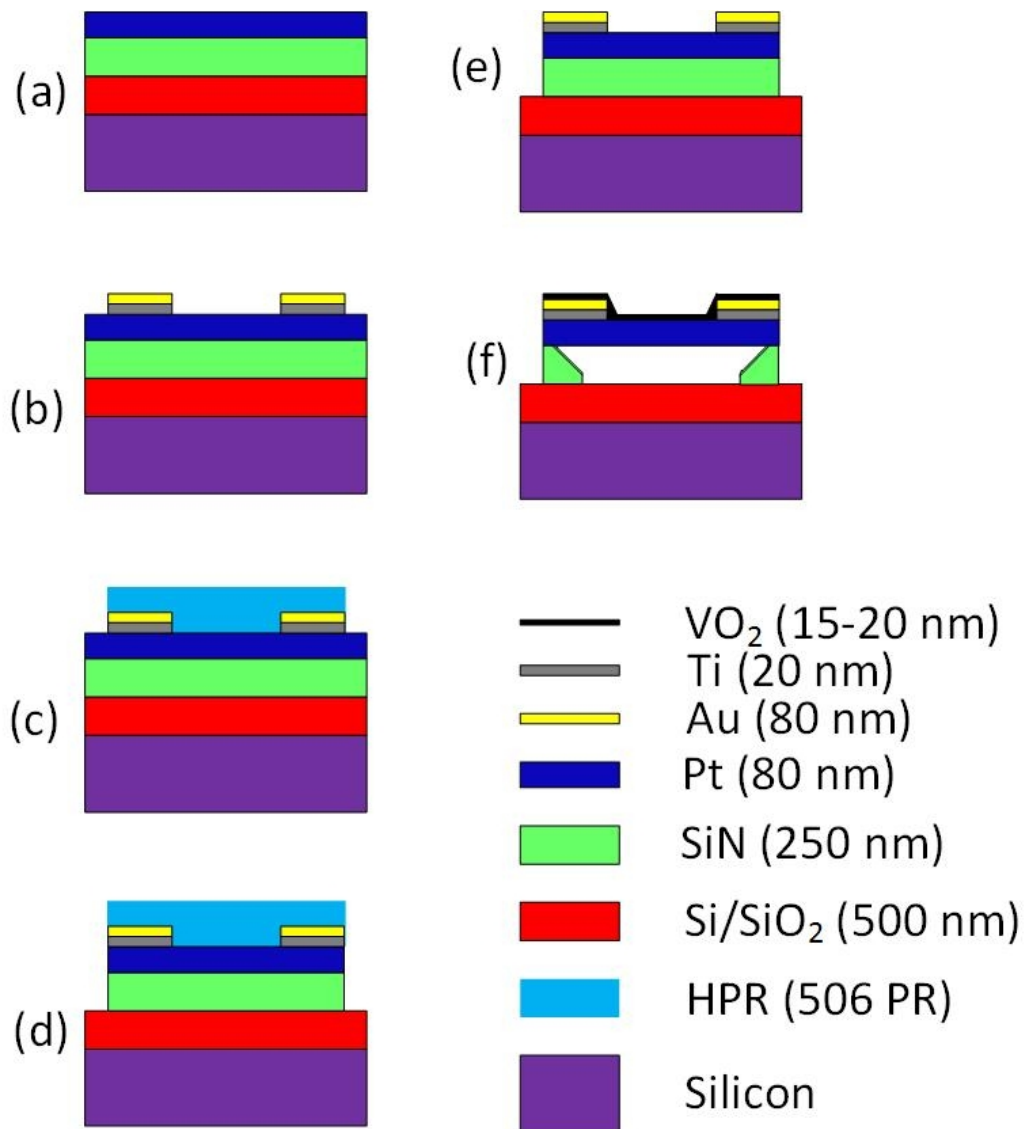


Figure 7.6: Process flow for microfabrication of doubly clamped beam resonators. Thermal oxide wafers were coated with 250 nm SiN using LPCVD and 80 nm Pt in step (a). Patterning and lift off, etch, steps were done until the device was released. VO₂ films were deposited on released devices using an optimized deposition condition

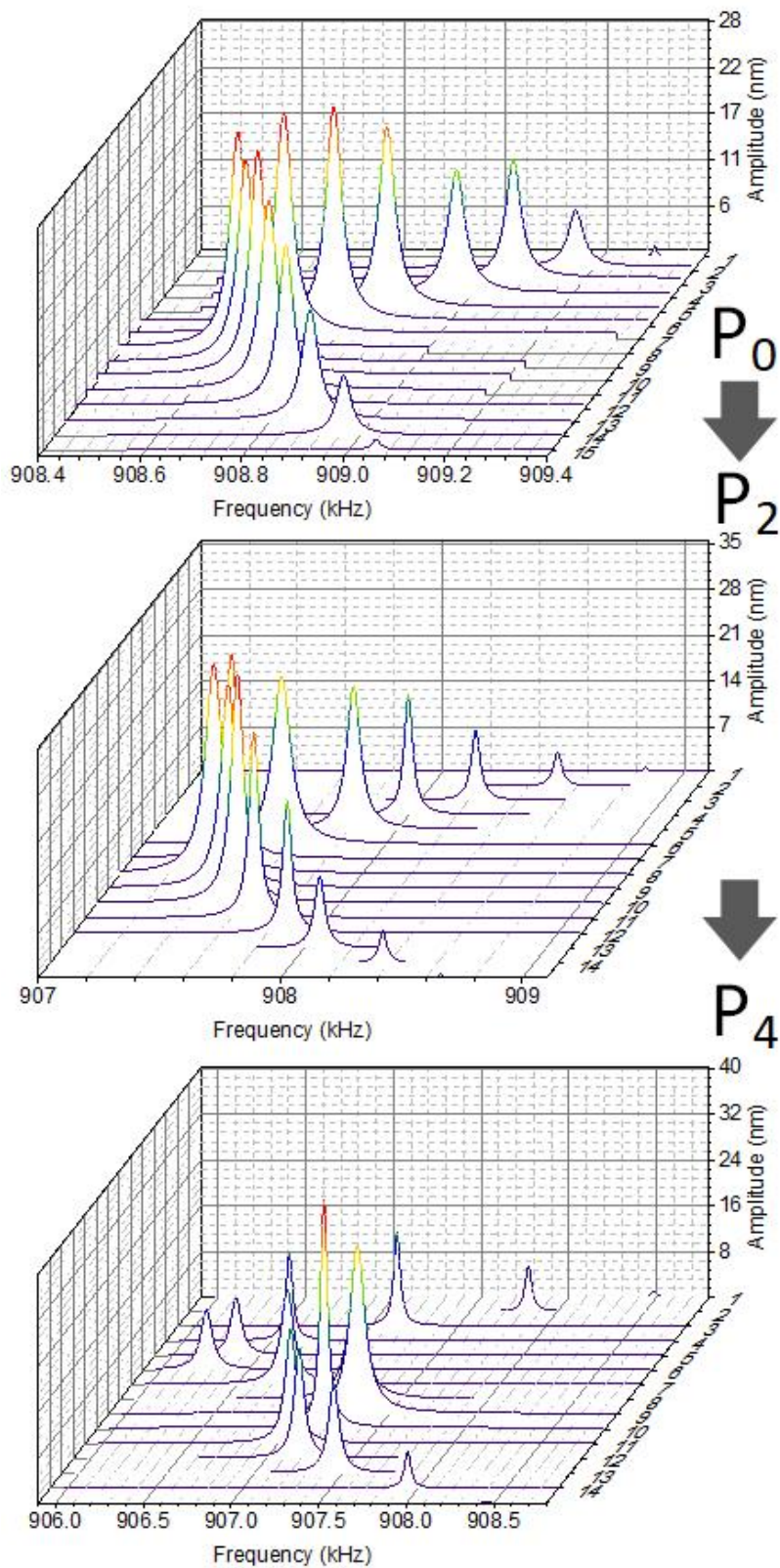


Figure 7.7: 3D plot of frequency and amplitude variation of the resonator at fifteen different locations in the suspended part in between the anchor points at different power levels.

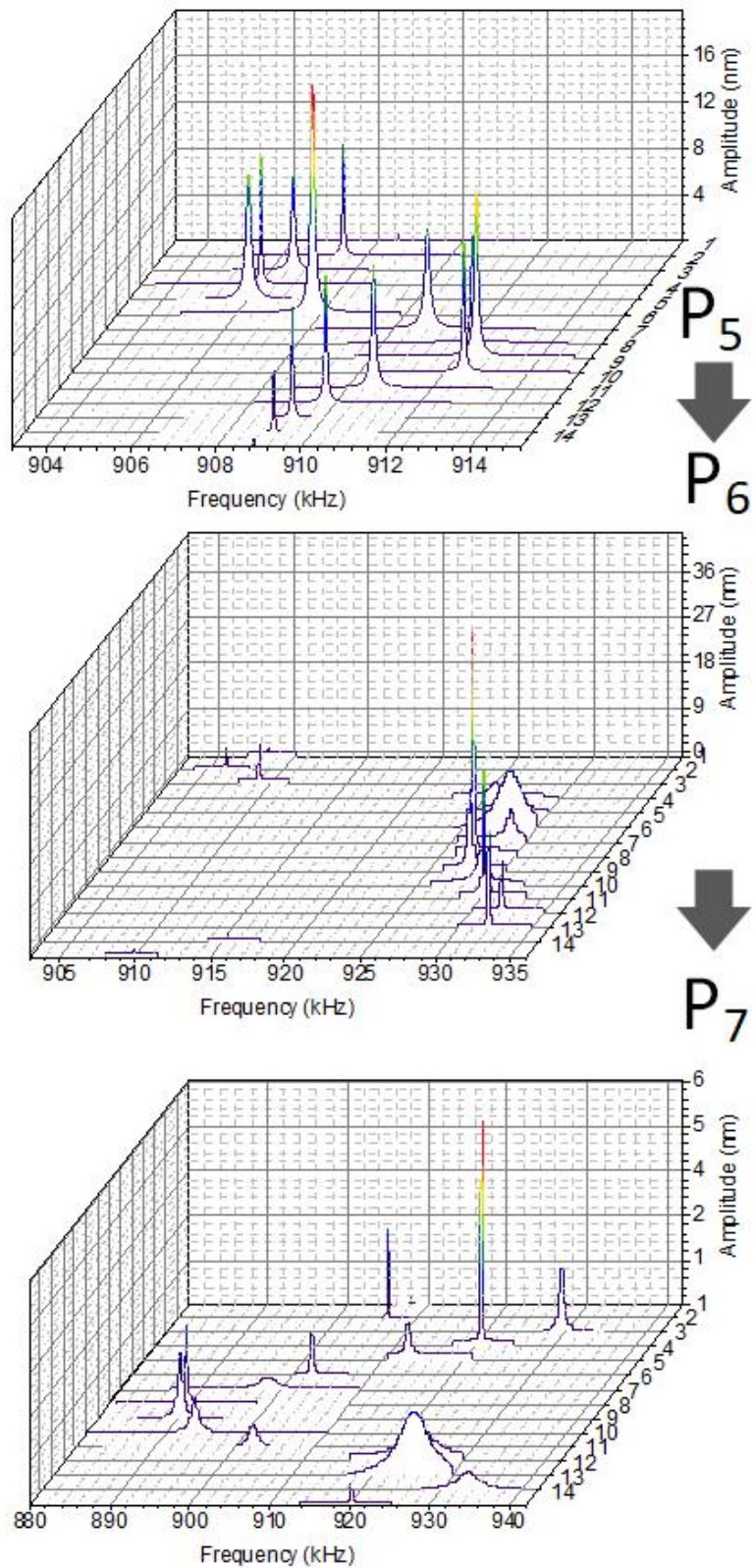


Figure 7.8: 3D plot of dynamic response of the resonators for higher optical powers.

Chapter 8

Electro-mechanical frequency tuning of VO₂ coated resonators

8.1 Abstract

In this study, we investigated the effect of electric field on dynamic mechanical response of a VO₂ coated microstring resonator. A two contacts vacuum probe station was developed to apply electric field on VO₂ film deposited on the string and resonance frequency was measured as a function of ac and DC electric fields. Doubly clamped beam of VO₂ resonator was heated by applying direct and indirect electrical current and a three way frequency tuning was achieved at room temperature. The electro-thermal energy caused a decrease in frequency of the resonator below the insulator to metal transition of VO₂ which resulted as decrease in resonance frequency when the power was below a critical level. Above the critical level, the system demonstrated a large increase in frequency for both ON/OFF cycles and ac electric field. This reversed behavior in frequency got reversed again for highest electric fields resulting as a decrease in frequency. Three way frequency tuning of VO₂ base resonator at room temperature would provide an avenue to develop deployable system devices for electronic switching and tunability. Controlled

frequency tuning provides an understanding of electro-thermal actuation in vanadium dioxide MEMS devices.

8.2 Introduction

Micromechanical resonators have been a great area of interest in scientific community because of their extensive diversity of applications starting from sensing, detection, energy harvesting, actuation, molecular manipulation, and information processing. Among them, micromechanical actuators got significant attention recently after the incorporation of phase changing material into this technology. Phase changing material possesses unique advantages in creating stress, strain and force gradient, due to the alteration of its intrinsic properties (like elastic modulus, thermal expansion co-efficient, magnetic properties etc.) owing to the external stimuli (electric field, magnetic field, temperature), which is the basis of actuating devices. In order to address this purpose transition metal oxide (TMO) has been exploited extensively in the recent past where phase transitions arise from electronic correlation, lattice distortion and magnetic ordering which give rise to the non-linear change in various physical properties.

Vanadium dioxide (VO_2) is one of the candidates in the family of TMO's which shows such non-linear variation in its physical properties at 68°C (ideally). It undergoes a first order transition at this temperature where its resistance sharply changes three to five orders of magnitude. This transition is reversible and ultrafast in nature, and occurs because of its change in crystal symmetry due to the transformation from monoclinic (M1) insulating phase (space group $P2_1/c$) to rutile (R) metallic phase (space group $P4_2/mnm$). More precisely, the dimerization of alternating V atoms which results in two different V-V bond lengths and tilting of these dimers with respect to the c-axis causes the transition. Although the mechanism of the transition is still

remains elusive as there are two scenarios possible: a lattice distortion driven (Peierls-like) or an electron correlation driven (Mott-like) [166], however, recently it has been proposed that the transition happens due to the strong interaction of electrons and phonons together and hence it is described as “Mott-assisted Peierls” mechanism.

Despite the puzzling physics of VO₂, it has been widely explored in varieties of technological applications such as thermal optical and electronic switches, smart windows, microbolometer, nonvolatile memory and memristors. Most of these applications are explored by exploiting the electronic properties of VO₂. For instance, variation of its electrical conductance by thermal stimulus is the key for smart windows, microbolometer and thermal switches applications. On the other hand, VO₂ also changes its electrical conductance isothermally under critical electric field (E_c) which is known to be electric field assisted metal-insulator transition (E-MIT). This property has been widely explored in nonvolatile memory, memristors and neuromorphic devices. Although there are numerous reports on VO₂ based devices taking advantages of the electrical conductance change but there are few reports on variation of mechanical responses when it undergoes a thermal cycle but the stress induced phenomena was well explained by studying the bending of VO₂ coated microcantilevers [167]. McGee et.al [64] showed similar behavior by measuring frequency change with the function of temperature. Recently such modulation of mechanical responses was also observed by photothermal actuation by Wang et.al [168]. However, there is no such report where mechanical modulation can be controlled isothermally by manipulating DC electric field taking the advantage of E-MIT property of the VO₂.

Voltage driven insulator to metal transition in VO₂ is very promising for its potential applications in electronic devices. Considering the ultrafast phase change in VO₂, this transition can potentially be triggered in picoseconds [169]. At room temperature, high resistivity of VO₂ which can create joule

heating effects and increase the temperature causing the material to transform into metallic state caused by the temperature rise [170]. Here we will study both thermal and electric field induced mechanical frequency variations of VO₂ microstring resonator at its first mode.

The resonance frequency of the resonator has been tuned with contraction or expansion of the structure itself with application of electric field assisted joule heating [171]. Electric field assisted joule heating provides simplest platform where electrical wire contacts can be used to apply current with wire bonding which simplifies the fabrication process of frequency tuneable cantilevers [172]. Because of very small size of the resonators, the actuation can be done at very low voltages making it suitable for applications in electronic switching applications [173].

In this work we demonstrate modulation of mechanical frequency of a suspended VO₂ coated microstring using DC and AC electric-field. The suspended VO₂ microstring was allowed to vibrate by piezoelectric vibrator. We showed that the resonance frequency of the microstring can be reduced by applying an electric field lower than E_c whereas it can be enhanced by applying higher electric fields greater than E_c . The MIT of VO₂ can be greatly tuned by controlling the tensile stress of the film. Larger tensile stress shifts the MIT towards higher temperature as well as higher electric field whereas larger compressive stress does the opposite. In order to facilitate compressive stress during growth, titanium dioxide (TiO₂) was used as buffer layer at the interface before depositing VO₂. Electric-field induced joule heating can cause a change in resonance frequency which can be described by [154].

$$f_T/f_i = \sqrt{1 + (f_0/f_i)^2 \left(\frac{\alpha_e}{\Lambda_e}\right) \times \frac{L^3}{40.8w^3h} P_e} \quad (8.1)$$

where, f_T is temperature dependent frequency of resonator as a function of joule heating power P_e , α_e is thermal expansion coefficient, Λ_e is average

thermal conductivity of the resonator,

$$f_i = f_0 \sqrt{1 + \frac{\sigma_i L^2}{3.4 E w^2}} \quad (8.2)$$

is the frequency of the resonator with residual stress and without electro-thermal heating and

$$f_0 = 1.03 \frac{w}{L^2} \sqrt{\frac{E}{\rho}} \quad (8.3)$$

is frequency of the resonator in first mode without any residual stress. These equations represent the approximate behavior of the resonator based on electro-thermal effects in Si based devices. However the thermally induced Insulator to metal transition can change the expansion coefficient and change in change in dimensions in equation. 8.1 leading to an increase in f_T .

8.3 Experimental

8.3.1 Fabrication and deposition

The devices fabricated in this work were carried out in Nanofab with pre-optimized recipe. Boron doped p-type <100> Si wafers (dia ~4") were thermally oxidized via wet oxidation in a tube furnace (Tystar) at 1050 °C of 1.5 μm thickness, followed by deposition of 200 nm thick stoichiometric silicon nitride (SiN) on top by low pressure chemical vapour deposition (LPCVD). The film stress was found to be 1.2 GPa measured by a Flexus 2320 stress measurement tool. The wafers were diced into 12.5 mm \times 12.5 mm square shape. Subsequently, the wafer were named as *SiN/SiO₂/Si*. The wafers were cleaned in piranha followed by acetone, IPA and water before depositing TiO₂ and VO₂ using pulsed laser deposition (PLD) technique. Both VO₂ and TiO₂ were deposited onto the *SiN/SiO₂/Si* wafers by pulsed laser deposition (PLD) from vanadium (99.9% purity, American Elements) and titanium

metal (99.9% purity, Kurt J Lesker) targets in an oxygen environment. A KrF ($\lambda = 248$ nm) excimer laser (Coherent, GmbH) was directed at the rotating target with a laser fluence of 2.6 J/cm^2 and a repetition rate of 10 Hz. The substrate, maintained at 600°C for the duration of the deposition, was placed directly opposite the target, 31 mm apart. Oxygen pressure was maintained at 10 mTorr for TiO_2 and 50 mTorr for VO_2 respectively. Initially TiO_2 was deposited for 15 min followed by 30 min annealing time before depositing VO_2 for 15 min. Parameters for the VO_2 deposition have been fully optimized in our previous work [1].

8.3.2 EMIT measurements with LDV

After deposition the phase and crystallinity were determined by X-ray diffraction (XRD) and the surface morphology by atomic force microscopy. The total thickness of the film was found to be 40 nm in which TiO_2 and VO_2 were 20 nm each. We built the electrical test probe station for device characterization and analysis under vacuum. This two probe set up was used to apply electric voltage across VO_2 strings. Two aluminum sheets were bent in bracketed shapes and screwed on a PET (insulating) surface which was screwed on a micro-manipulator which would allow one to move the stage laterally and vertically. Spring loaded probe station pins were glued at the unscrewed side of the brackets in such a way that they are fully compressed when they make a contact with the sample surface. Electrical connections were made via male-female adapters attached to the probe station sharp pin-bracket set up via electrical feedthrough. Controlled electric current/voltage was supplied via a BK PRECISION 9183 DC power supply with a computer controlled software program. Dynamic mechanical response (frequency, amplitude and phase) of the microstrings was recorded via Laser Doppler vibrometer (LDV) model Polytec MSA 500, at pressure of 2.5×10^{-5} mbar as a function of input voltage across the microstrings via Ti/Au contact pads. Red laser

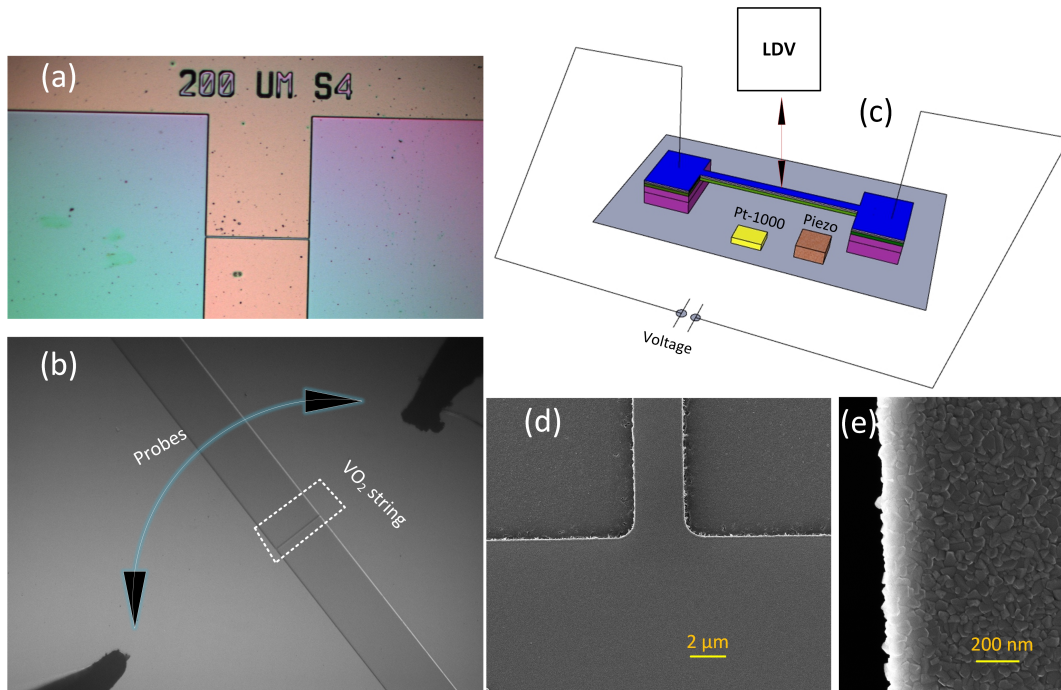


Figure 8.1: (a) SEM image of 200 μm long VO_2/TiO_2 coated string resonator with contact pads. (b) Microstring contact pads with probes. (c) schematic of electrical current applied to the string with Pt-1000 sensor for temperature measurements and piezo for applying acoustic vibrations to oscillate the resonator at its fundamental mode. (d) Scanning helium ion images of resonator without using any gold coating. Large VO_2 grains are visible at 200 nm resolution (e).

built in with LDV (633nm) with minimum laser intensity ($22 \mu W$) was used to record the Doppler shift. Input voltage was ramped at $0.1V/\text{minute}$ using a CSV excel file run with the power supply software for determination of EMIT while voltage pulses between 0 to $+600 \text{ mV}$ were used in order to see mechanical response of the strings below and above the EMIT. Resonance frequency was measured before and after the deposition of TiO_2 and VO_2 in order to estimate the mass and stress depending on the shift in resonance peak. AC signal was applied using function generator 3390 with different frequencies and voltages. Maximum peak amplitude of 400 mV was applied as too much power could possibly burn the resonator. Measurement set up is shown schematically in Fig. 8.1.

8.4 Results and discussion

Microfabricated VO_2/TiO_2 coated microstrings were subjected to 400°C for 2 hours in order to release any residual stress built during the fabrication. The resonance frequency of the uncoated resonator prior to the deposition was found to be 269.5 kHz . After depositing a 20 nm layers of TiO_2 and then VO_2 , the resonance frequency was measured again and it decreased by $\sim 92 \text{ kHz}$ as shown in Fig. 8.2 (a). The decreased frequency correspond to addition of mass on the resonator. The amplitude of vibration also decreased by order of magnitude because all other parameters were same except deposition of extra mass on resonator resulting which means driving more mass with same force meaning resonator would vibrate at small amplitudes. Resistivity measurements were done using two-probe contacts with the string with each resistance value recorded after waiting two minutes at a particular temperature during heating and cooling. Three orders of magnitude change in resistivity was confirmed as shown in Fig. 8.2(b). Tapping mode AFM studies were conducted to visualize the surface of the film. The average

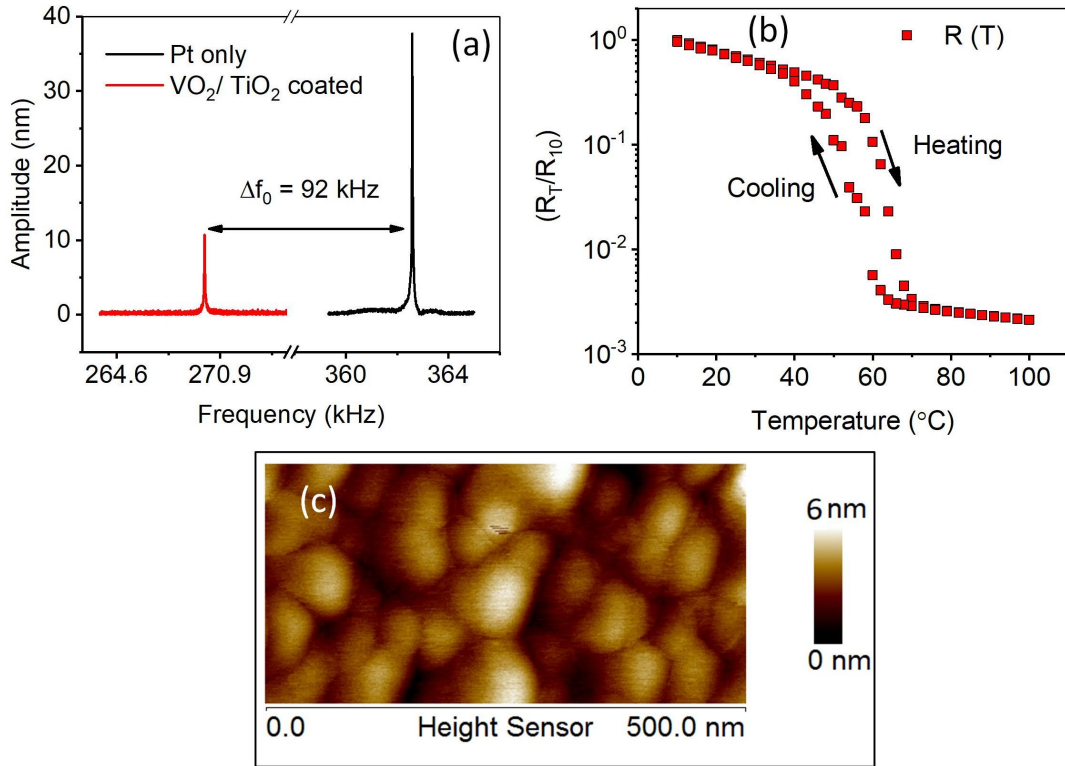


Figure 8.2: (a) FFT of first mode resonance frequency of uncoated and coated VO₂ strings. (b) Normalized resistance change of the film as function of temperature and (c) tapping mode AFM scan for 500 nm × 250 nm area with calculated average surface roughness of 0.69 nm.

roughness was 0.69 nm as calculated from the image in Fig. 8.2(c).

8.4.1 Frequency tuning with DC field

In order to understand the effect of DC field on mechanical frequency change of VO₂ resonator, we studied the dynamics of a 400 μm long resonator. The room temperature resonance frequency of resonator was 360.6 kHz. At lower electric fields, the resonance frequency was found to decrease abruptly as soon as the electric field was switched ON and returned to its initial value when the field was switched OFF. This was expected as electro-thermal effect causes joule heating reducing the stiffness of the string and decreasing its frequency when the the field is ON. This has been demonstrated in Fig. 8.3

(a) and (b). One can notice a drift in frequency which is likely because the resonator does not get enough time to retain thermal equilibrium and that some of the heat is still in the system leading to a drift in frequency. The change in frequency between ON and OFF states started increasing when the field was increased e.g. the frequency change for 63 kV/cm and 100 kV/cm fields was about 1 Hz which increased in case of an applied electric field of 125 kV/cm. However the response suddenly dropped to less than 0.5 Hz when the field was increased to 150 kV/cm. When the field was increased to 175 kV/cm, the frequency response was exactly reversed what we saw for lower electric field values. The increase in frequency was 3 times large as compare to a two time decrease in frequency for lower fields when the field was turned ON at 175 kV/cm as shown in Fig. 8.3(c). The amplitude of vibration however decreased with increased electric fields beyond 150 kV/cm as shown in Fig. 8.3 (d). We believe that the sudden increase in frequency is because of the insulator to metal transition in VO₂ film causing lattice compression because of crystal structure transformation of the film. The overall stress on the resonator is controlling the string dynamics as compare to a modulus decrease with increasing temperature. The increased compressive stress would make it harder for resonator to vibrate freely which would decrease the amplitude of vibration as evidenced by the amplitude decrease of the resonator above a critical field in part (d) of Fig. 8.3.

In order to see how much frequency increase can be controlled by the input voltage, we employed a voltage ramp across the resonator. While increasing the voltage, we saw a decrease in frequency for lower voltages and a sharp increase in frequency when the voltage increased beyond a critical value as shown in ramp up box in Fig. 8.4(a). All AC measurements were recorded with a fixed input signal of 20 mHz applied through the function generator. When voltage was decrease from 0.7 V, the frequency decreased up to a critical value and started increasing when the power was removed from the

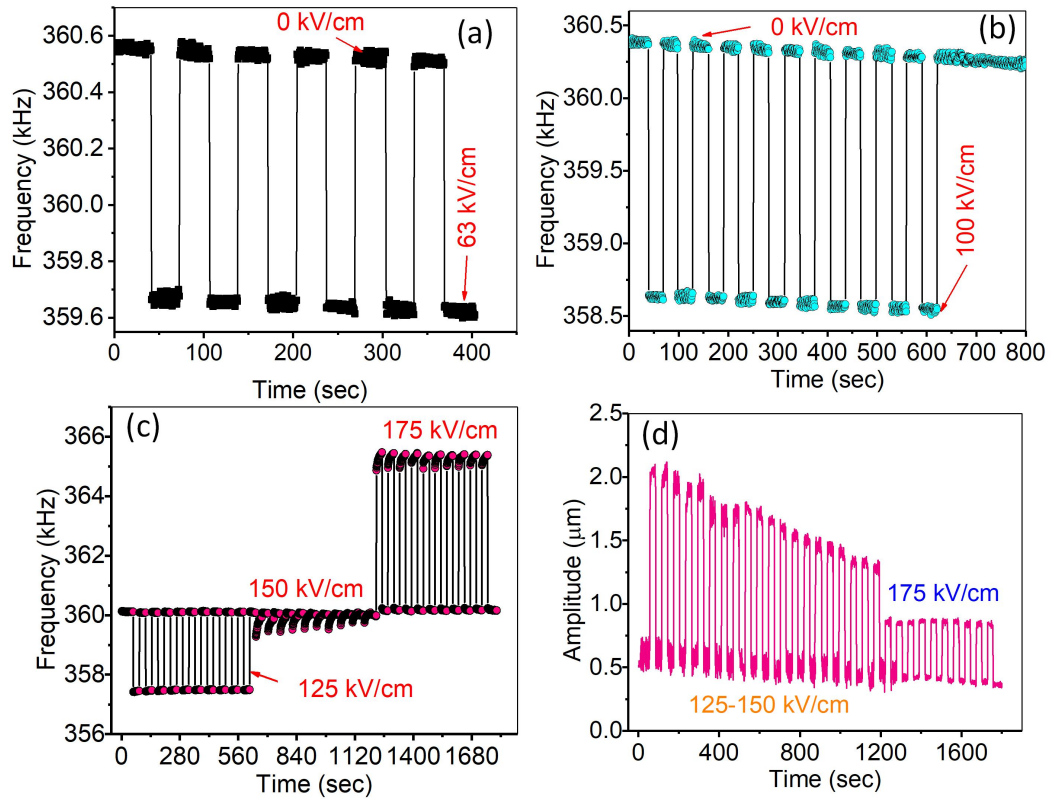


Figure 8.3: (a) Mechanical frequency of resonator when the resonator was subjected to an ON/OFF cycle of an electric field of 63 kV/cm and 100 kV/cm (b). Frequency and amplitude variation for electric fields from 125-175 kV/cm in (c) and (d) respectively.

system leading to the starting value of resonance frequency as shown in ramp down box in Fig. 8.4(a). A 2 kHz decrease in frequency followed by a 12 kHz increase in frequency was observed for voltage ramp between 0 to 0.7 V. In order to find out the critical voltage for maximum change in the frequency, we increased the ramp window to 0-1 V. It turned out that after a 12 kHz increase in frequency, further increase in voltage caused a sharp decrease in frequency of about 15 kHz was observed as shown in ramp up box of Fig. 8.4(b). When the voltage ramp down, the system quickly transformed to metallic VO₂ state increasing the frequency of resonator to about 20 kHz. This is likely because system got overheated at 1 V and possibly losing heat at a smaller rate as compare to when it was heated as the experiment is done under high vacuum and the only heat sinks are the conduction through the anchor points. In order to further confirm this behavior, we ran ON/OFF cycles for 0.8, 0.9, and 1V and observed that the frequency starts decreasing for 0.9 V. This can be explained that VO₂ is a bad conductor of heat in metallic state when it is still a good conductor of electricity [174]. When in complete metallic state, the loss of heat from the system is decreased because of poor thermal conduction leaving the system in this state for longer times as compare to the heating cycle. That might be a reason we observed a large frequency shift during the ramp down cycle. We saw a positive drift in frequency as opposed to a negative one (seen for lower voltages below critical field) which is again possibly because the the system still retains some heat when the external power was turned OFF and this residual heat adds up as we keep switching between ON/OFF cycles leading to a positive drift in frequency because this drift adds up to the next ON cycle of the voltage.

8.4.2 Frequency tuning with AC field

Mechanical frequency variation as a function of amplitude variation of applied electric field was studied. We chose a small microstring from the same

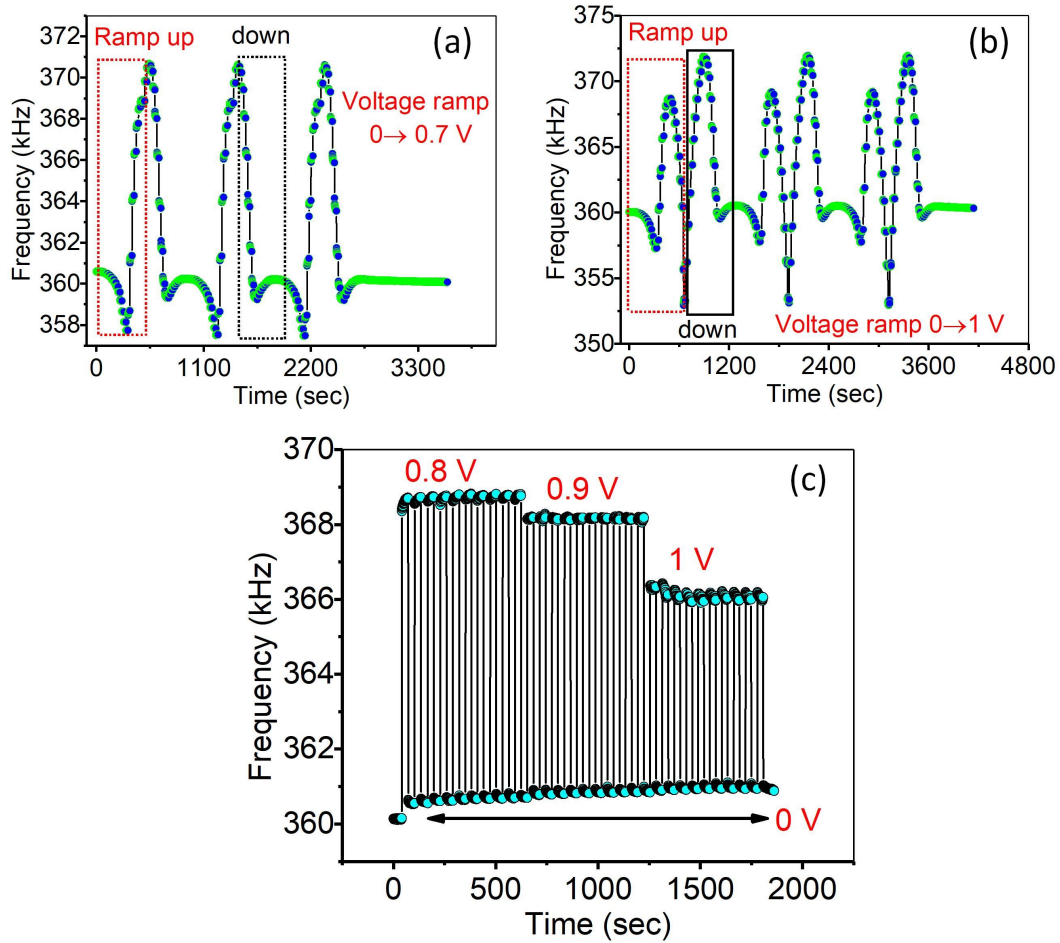


Figure 8.4: (a) Mechanical frequency response for a voltage ramp of 0-0.7 V for both heating and cooling cycles with electro-thermal energy. (b) Voltage ramp of 0-1 V leading to confirm the upper critical field for EMIT transition with slightly different behavior during the cooling and heating cycles. (c) confirmation of upper critical field with ON/OFF cycles of 0.8, 0.9 and 1 V.

chip because it offers higher frequency sensitivity. For applied voltages of 150 and 200 mV, the frequency of resonator was found to decrease with increasing peak voltage value and a cosine type wave of mechanical frequency variation was observed with doubled frequency as compare to the input signal. This was expected as increase in voltage of input signal in both directions caused an increase in frequency of the resonator. The low amplitude frequency response is shown in Fig. 8.5 (a) and (b). However the frequency response of resonator got complex as voltage was increased to 260 and 270 mV. A decrease in frequency followed by a sharp increase in frequency was observed for a positive peak voltage as shown in Fig. 8.5 (c). The frequency started decreasing when the slope of input voltage became negative until it reaches to zero amplitude. When the voltage pulse entered to negative peak, we saw an increase in frequency again followed by a sharp decrease. A total of twelve peaks were observed for three peaks of input signal and twelve negative peaks were observed for three negative peaks of input signal as shown in Fig. 8.5 (c). When the amplitude of the same input signal was increased to 270 mV, the total number of peaks and valleys of response signal became 14.

The out frequency response did not change when the voltage was increased to 290 mV as shown in Fig. 8.6 (a). However a large increase in frequency for both positive and negative half cycles was observed when the the amplitude was increased to 320 mV as shown in Fig. 8.6 (b). A small decrease in frequency was followed by a huge increase in frequency ~ 20 kHz was seen. The response oscillation was doubled as compare to input signal frequency for both 320 mV and 330 mV signals shown in Fig. 8.6 (b). Even though we observed a time lag in all the AC field tuned frequency measurements with respect to the input signal but it became more dominant for 400 mV signal as shown in Fig. 8.6 (d). The output signal lags input signal because the LDV converts the time domain data into frequency domain and fits the data with FFT with an in built macro which takes minimum of 0.5

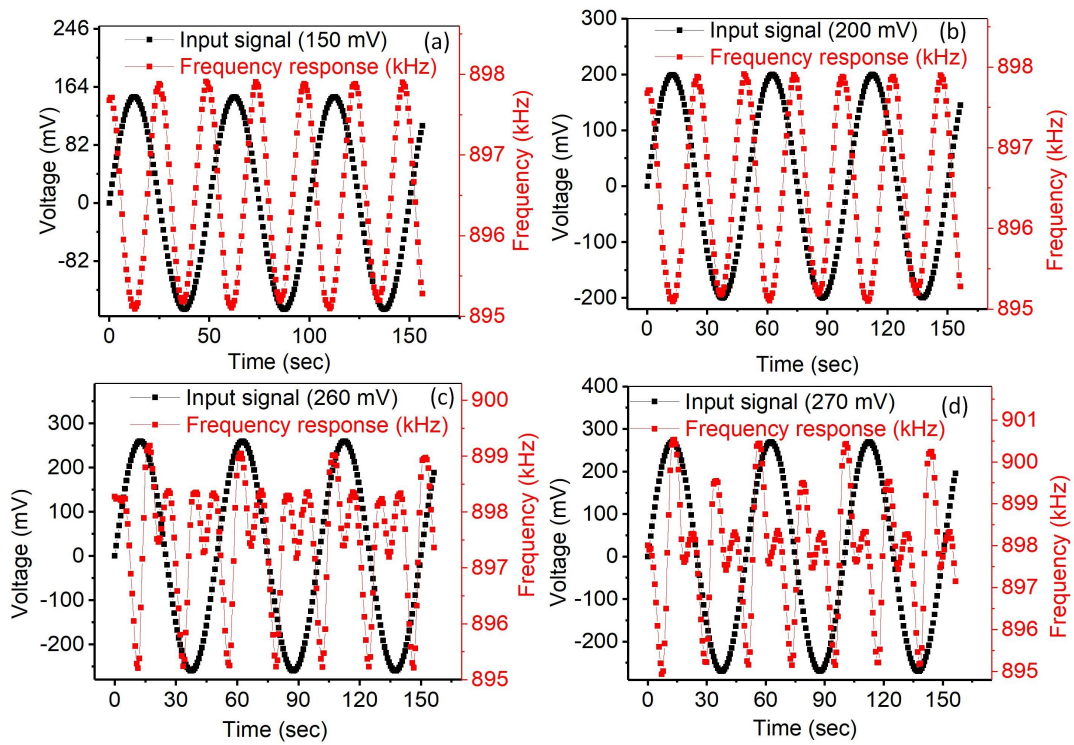


Figure 8.5: (a) Dynamic response of 200 μm long resonator as a function of ac electric field with input voltage of 150 mV. (b) mechanical response for an ac signal of peak voltage of 200 mV, 260 mV (c) and 270 mV (d).

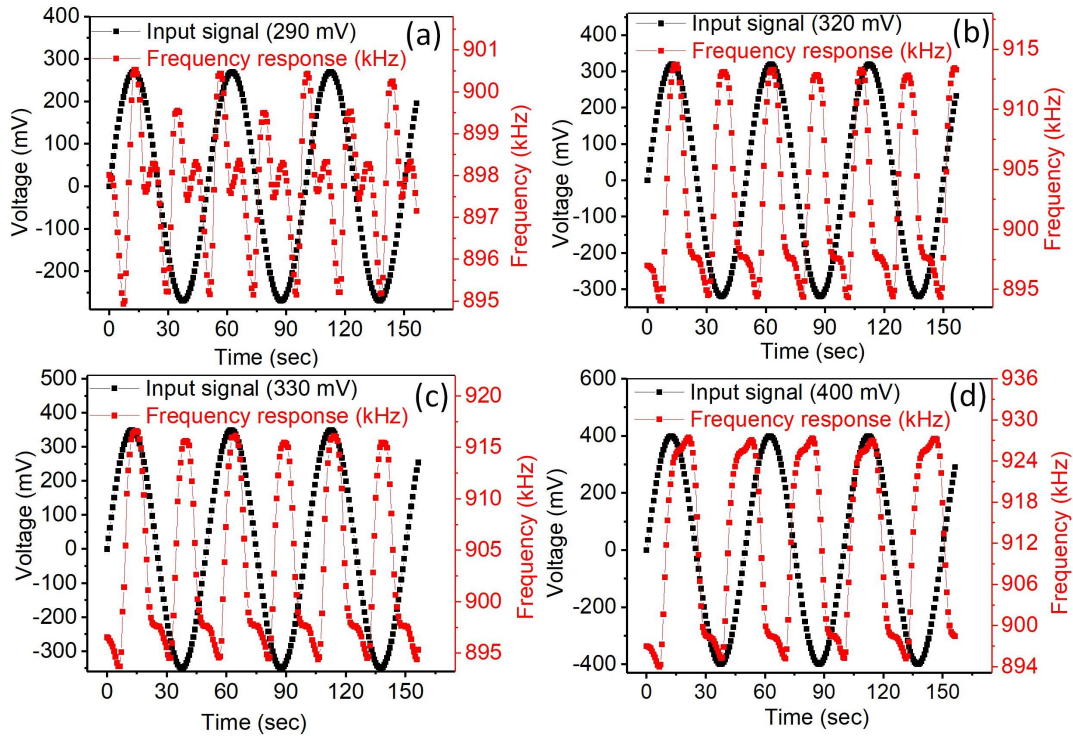


Figure 8.6: Mechanical frequency response vs ac field applied for input amplitude of 290 mV (a), 320 mV (b), 330 mV (c) and 400 mV (d).

seconds for each frequency value. The string response is expected to be much faster and the input signal is overlaid to the output signal by using a MATLAB code which generated 20 mHz signal. The change in frequency for 400 mHz signal was ~ 25 kHz.

A different kind of modulation was seen when the input signal was changed to square wave instead of a sine wave as shown in Fig. 8.7. When a 400 mV signal with a frequency of 20 mHz was applied, a frequency increase of 25 kHz (2.8%) was observed. However the frequency did not reversed back to its initial value as the voltage was quickly shifted to -400 mV from 400 mV. A small frequency shift of ± 1 kHz was observed within the initially elevated frequency as zoomed in marked region of Fig. 8.7 (a) is shown in Fig. 8.7 (b).

Since the LDV limitations on recording the data, we selected only one frequency to see the variations in frequency as a function of amplitude variation

of the input signal. The response for lower and higher frequencies is documented in supplementary information Fig. 8.8 and Fig. 8.9. The response time was beyond measurement time for input frequencies above 1 Hz.

8.5 Conclusions

In this work, we demonstrated frequency tuning of VO₂/TiO₂ coated microstrings resonators with both DC and AC electric fields. First mode mechanical resonance frequency of the resonator was continuously measured as a function of applied electric field across the resonator via Au/Cr contact pads. Electro-thermal joule heating was employed and was responsible to heat the VO₂ microstring and caused a phase change at a particular value of electric field. The resonance frequency was measured with Laser Doppler Vibrometer. For DC fields, resonator's frequency decreased until an electric field of 150 kV/cm where the resonator frequency started increasing with applied voltage. We called this a critical field E_c which causes insulator to metal transition in top layer and induces a large stress because of the lattice compression. Above a certain level of field, which was 200 kV/cm corresponding to an applied voltage of 0.8 V, the frequency started decreasing. Since the area of cross-section of the resonator is very small and the all measurements were done in high vacuum, the resonator was able to contain more heat than heat conduction because of poor thermal conductivity of VO₂ in metallic phase. This accumulated heat is enough to soften the string via decreasing its modulus and hence an overall decrease in amplitude of frequency change was observed. Similar behavior was seen for a sine wave AC applied signal across a 200 μ m resonator where the mechanical frequency was tuned in three different ways depending on the voltage applied. Frequency behavior was also recorded for a square wave input where the resonator remained at high frequency regime with ± 1 kHz variation in offset upon a ± 400 mV applied

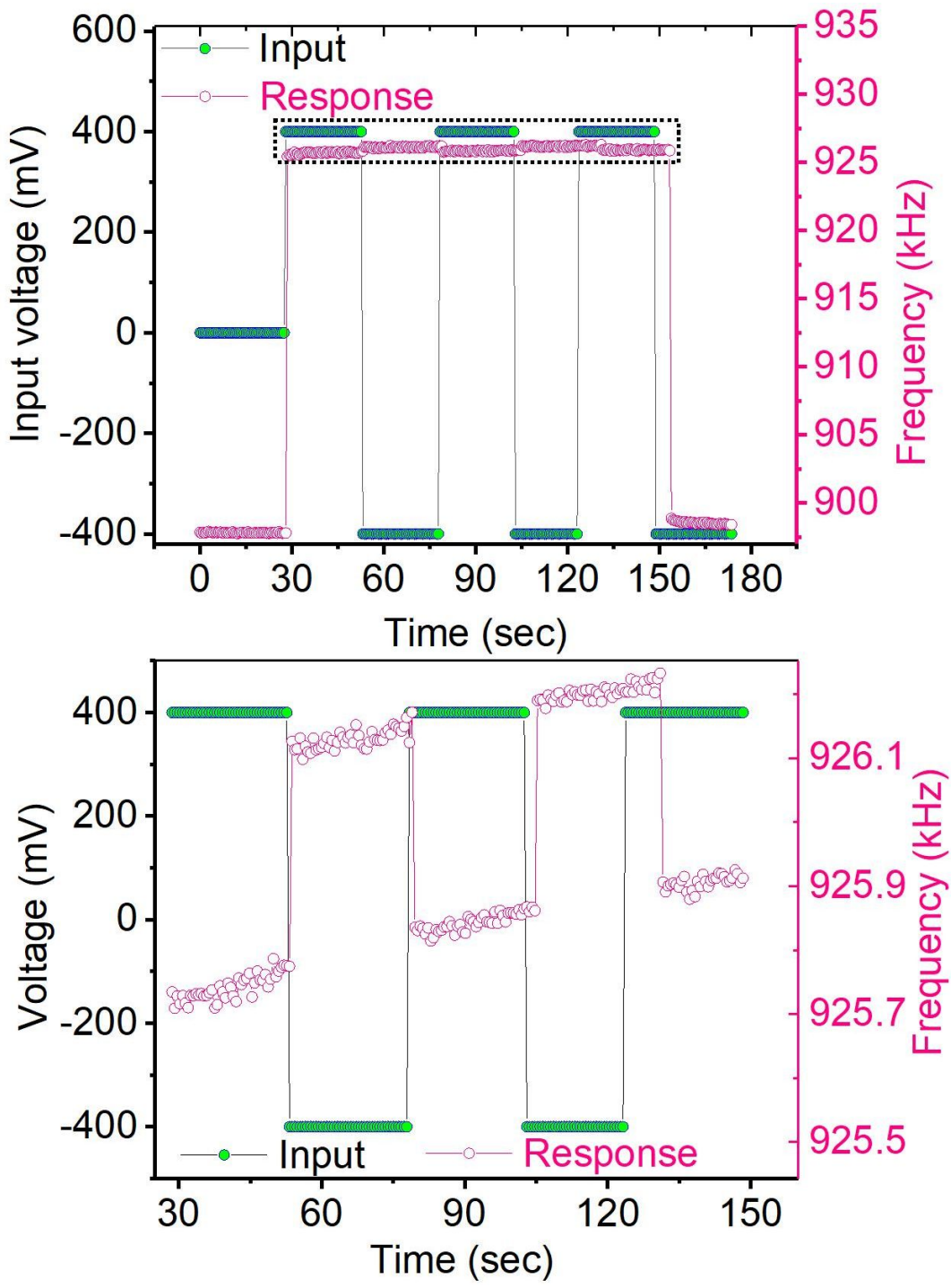


Figure 8.7: (a) Mechanical frequency variation as a function of step function of peak amplitudes of ± 400 mV. (b) Zoomed in selected portion of (a) to visualize the frequency changes after the first voltage step.

signal. This work provides an excellent platform for tuning mechanical frequency of TMO coated resonators and applications in electronic switching, sensing and actuation.

8.6 Acknowledgments

This work was supported by the Canada Excellence Research Chair (CERC) program (No. SF0926). The authors acknowledge the Nanofab at the University of Alberta for providing the fabrication facility. Authors also thank Ms. Rosmi Abraham for useful discussions and Dr. Hyun-Joong Chung 's team for providing valuable feedback during the weekly presentations.

8.7 Supplementary data

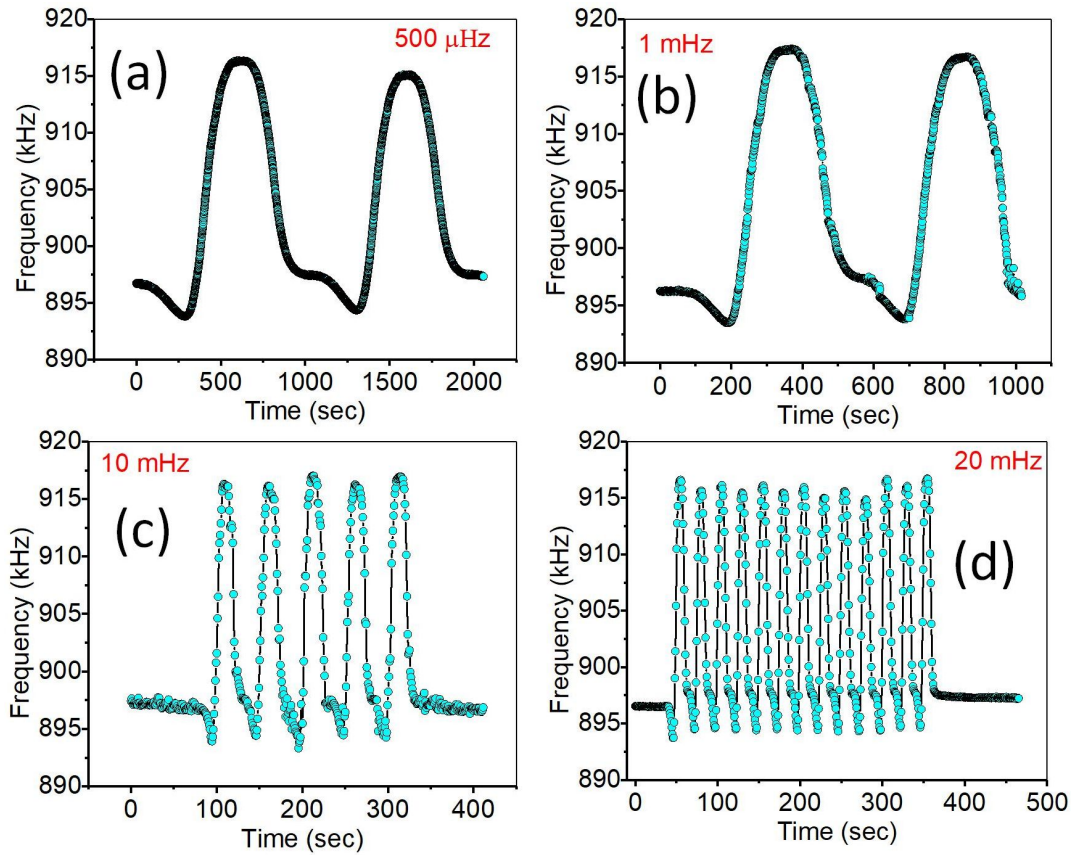


Figure 8.8: (a) Mechanical frequency variation as a function of step function of peak amplitudes of ± 400 mV at $500 \mu\text{Hz}$, (b) 1 mHz , (c) 10 mHz and (d) 20 mHz .

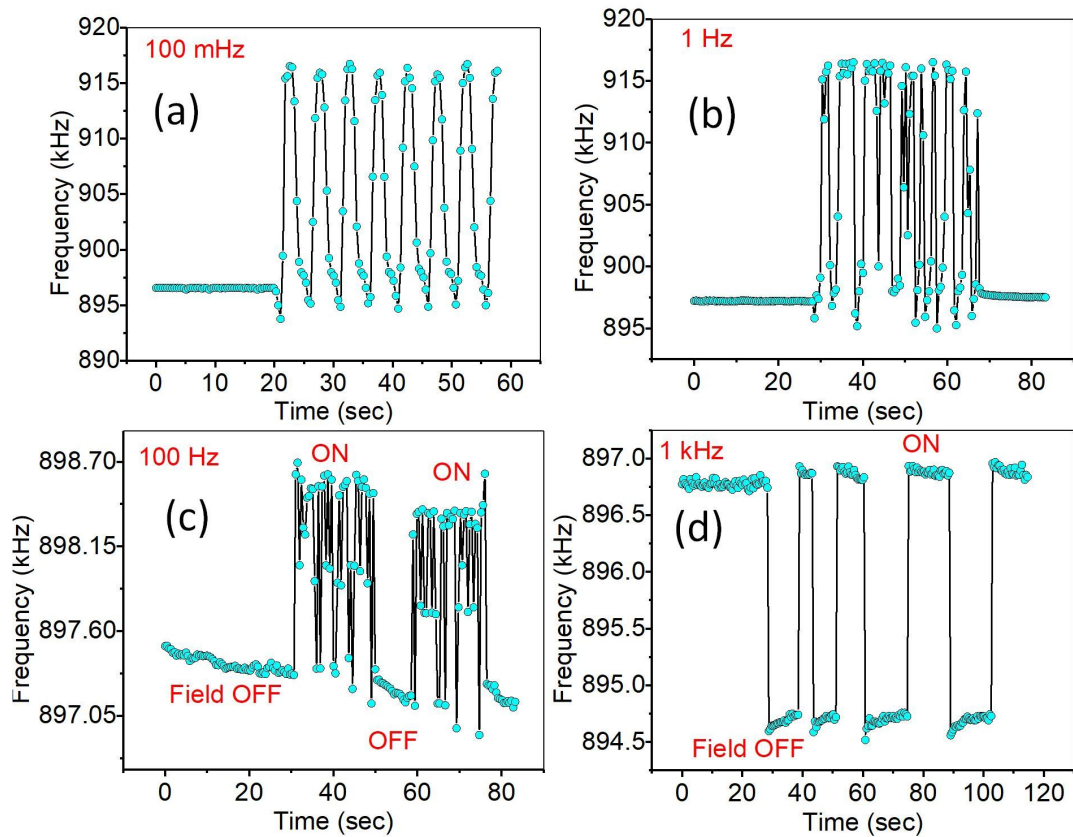


Figure 8.9: (a) Mechanical frequency variation as a function of step function of peak amplitudes of ± 400 mV at 100 mHz, (b) 1 Hz, (c) 100 Hz and (d) 1 kHz.

Chapter 9

Conclusions

9.1 Summary of completed work

This thesis was focused on dynamic mechanical response of small thermal mass resonators for probing phase transitions in polymers and solids. We chose suspended channel microcantilevers for thermal analysis of polymers and doubly clamped beam/microstrings resonators for probing solid-solid phase transitions with thermal, opto-thermal and electro-thermal excitation. First three chapters of the thesis addressed the literature, fundamentals and theory, fabrication, experimental designs and characterization techniques. A motivation with summary of research objective was also presented.

The experimental chapters in this thesis (Chapters 4-8) are devoted for understanding the mechanics of small thermal mass MEMS devices and using these devices to probe thermal properties of materials. Both first order phase transitions (melting and solid-solid phase transition) and second order phase transitions (glass transitions, β relaxation and cold crystallization) were detected with miniaturized devices.

Chapter 4 specifically targets the use of suspended, singly clamped microcantilever with embedded microchannel to study the phase transitions in polymers. Two well known polymers PMMA and PLA were melt flown into

the microchannel and dynamic response of channel was studied as a function of controlled heating. The large change in frequency was observed at the phase transition temperatures. The results were compared with standard DSC technique. This study used pico-liter volume of polymers and detected some of the side chain motions of polymers (e.g. β relaxation in PMMA) which was not detectable with conventional calorimetric techniques.

Chapter 5 discusses the deposition of a phase change materials VO₂ using pulsed laser deposition method. The idea of this chapter was to obtain optimized film deposition conditions which would later be used for deposition on doubly clamped beam resonators. Dependence of flow rate of oxygen during the deposition of polycrystalline VO₂ on thermal oxide substrate material was specifically discussed. Oxygen flow rates of 0.5 to 90 SCCM were used for deposition of thin films. It was observed that oxygen vacancies or defects at the grain boundaries may depend on oxygen flow rate during the deposition. Oxygen flow rates of 0.5-5 SCCM did show polycrystalline monoclinic VO₂-(011) peak in XRD but did not show insulator to metal transition. Intermediate flow rates 10-30 SCCM showed a decrease in onset temperature as well as in magnitude of MIT. Higher flow rates 50-90 SCCM showed a large hysteresis with highest magnitude of MIT with offset temperature shifted 60 °C. Even though the deposition conditions for chamber pressure, substrate temperature and laser plume size were optimized in our previous study [1], the effect of reaction gas flow rate on microstructure and phase was never reported before. We showed that by depositing the films at an optimal flow rate, one can reduce the percentage of other polymorphs of VO₂ and that the insulator to metal transition can be shifted to either high or low temperatures. In Chapter 6, opto-thermal induced phase transition in VO₂ microstrings was studied from the dynamic mechanical response of the resonator. Pre-optimized deposition conditions (Chapter 5) were used to deposit the thin films on resonators. Triggering of phase change at different optical wave-

lengths and powers was studied at room temperature and high vacuum. Bi-directional frequency tuning was obtained by varying input optical power and a tri-directional frequency tuning was obtained by using different optical wavelengths. We used LDV built in laser of fixed wavelength of 635 nm for both pumping the system and probing the dynamic response in case 1. In case 2, the probe laser was set to its minimum power while pump lasers were used externally. A 6.5 % change in frequency was observed upon heating the resonator above 68 °C with three to four order of magnitude change in electrical resistance of the resonator during the phase transition. Pump and probe optical excitation resulted as 1.2 % increase in frequency at optical power of 52 μ W. When the resonator was pumped externally with a total power of 97 μ W, 635 nm source, a total increase of 2.5% in frequency was observed.

After investigating the resonance frequency tuning with optical power being irradiated at the center of the microstring (Chapter 6), the resonance frequency variations were also studied by moving the pump and probe laser along the resonator between the anchor points in Chapter 7. Depending on the heat conduction and proximity of heat sink, various different frequency tuning mechanisms were studied. Combined electrical and optical powers were used to study the effect on mechanical response of the resonator. The resonance frequency was dropped (\sim 1-2 kHz) as the scan spot moved towards the center for an optical power of 22-33 μ W and increase significantly (20-26 kHz) as the power was increased. The change in frequency was found to be dependent on optical power intensity as well as the proximity of the exposed area from the anchor points of the string (Heat sink).

Chapter 8 was focused on electrical induced insulator to metal transition in VO₂ microstrings and mechanical frequency response as a function of DC and AC fields. Frequency response was studied as a function of applied electric field across the resonator. A tri- directional frequency tuning was

obtained for system being in below T_c , just above T_c and over heated regime. A different sort of frequency tuning was reported when AC signal of 20 mHz was applied across the resonator at different voltages. Electro-thermal heating of the resonator caused a decrease in mechanical resonance frequency up to 300 mV electric voltage applied across it. The maximum increase in frequency was observed for peak voltage of ± 400 mV. Above that voltage the effect of modulus decrease of SiN combined with the stiffness increase because of MIT in VO₂ leading to lower values of frequency increase. We were not able to probe higher voltage/electric field for which microstrings frequency would be completely dominated by the decrease in modulus of underneath layer of SiN as the strings were found to be burnt above 1 V signal applied.

9.2 Recommendation for future work

Given the success of the work presented previously, there are several projects that are currently being investigated for potential applications of both suspended microchannel cantilevers and VO₂ thin films based resonators. The ability of suspended resonator system to analyze a pico-liter volume and its extraordinary sensitivity to study changes in density, viscosity and viscoelasticity in liquids, this technique has definitely huge potential studying biological systems where higher sensitivities are required and sample size is small. Since the insulator to metal transition in VO₂ is very close to room temperature which makes it very interesting material for numerous applications in switching, sensing, energy harvesting and Bolometers.

Bibliography

- [1] R. Mcgee, A. Goswami, B. Khorshidi, K. Mcguire, K. Schofield, and T. Thundat, "Effect of process parameters on phase stability and metal-insulator transition of vanadium dioxide (VO₂) thin films by pulsed laser deposition," *Acta Mater.*, 2017.
- [2] A. H. Z. Peter Baum, Ding-Shyue Yang, "4d visualization of transitional also have a wavelength on the scale of atomicdistances and as demonstrated in the studies of melt and ing and lattice dynamics by ultrafast x-ray ab," in *Science*, 2007.
- [3] E. Inshakova and O. Inshakov, "World market for nanomaterials: structure and trends," *MATEC Web of Conferences*, vol. 129, p. 02013, 2017.
- [4] C. Palmberg, H. Dernis, and C. Miguet, "Nanotechnology: an overview based on indicators and statistics," *OECD Science, Technology and Industry Working Papers*, p. 112, 2009.
- [5] I.-B. Baek, S. Byun, B. K. Lee, J.-H. Ryu, Y. Kim, Y. S. Yoon, W. I. Jang, S. Lee, and H. Y. Yu, "Attogram mass sensing based on silicon microbeam resonators," *Scientific Reports*, vol. 7, apr 2017.
- [6] T. P. Burg and S. R. Manalis, "Suspended microchannel resonators for biomolecular detection," *Applied Physics Letters*, vol. 83, pp. 2698–2700, sep 2003.

- [7] B. A. Schmid S, Dohn S, "Real-time particle mass spectrometry based on resonant micro strings," *Sensors*, 2010.
- [8] C. N. Berglund, "Thermal filaments in vanadium dioxide," *IEEE transactions on Electron devices*, 1969.
- [9] A. P. G Stefanovich and D. Stefanovich, "Journal of physics: Condensed matter," in *Electrical switching and Mott transition in VO₂*, 2000.
- [10] A. Cavalleri, C. Tóth, C. W. Siders, J. A. Squier, F. Ráksi, P. Forget, and J. C. Kieffer, "Femtosecond structural dynamics in VO₂ during an ultrafast solid-solid phase transition," *Physical Review Letters*, vol. 87, nov 2001.
- [11] M. Liu, H. Y. Hwang, H. Tao, A. C. Strikwerda, K. Fan, G. R. Keiser, A. J. Sternbach, K. G. West, S. Kittiwatanakul, J. Lu, S. A. Wolf, F. G. Omenetto, X. Zhang, K. A. Nelson, and R. D. Averitt, "Terahertz-field-induced insulator-to-metal transition in vanadium dioxide metamaterial," *Nature*, vol. 487, pp. 345–348, jul 2012.
- [12] S. Yu, S. Wang, M. Lu, and L. Zuo, "A metal-insulator transition study of vo₂ thin films grown on sapphire substrates," *Journal of Applied Physics*, vol. 122, no. 23, p. 235102, 2017.
- [13] J. MacChesney and H. Guggenheim, "Growth and electrical properties of vanadium dioxide single crystals containing selected impurity ions," *Journal of Physics and Chemistry of Solids*, vol. 30, no. 2, pp. 225 – 234, 1969.
- [14] A. Beaumont, J. Leroy, J.-C. Orlianges, and A. Crunteanu, "Current-induced electrical self-oscillations across out-of-plane threshold switches based on vo₂ layers integrated in crossbars geometry," *Journal of Applied Physics*, vol. 115, no. 15, p. 154502, 2014.

- [15] P. Kiri, M. E. Warwick, I. Ridley, and R. Binions, "Fluorine doped vanadium dioxide thin films for smart windows," *Thin Solid Films*, vol. 520, no. 4, pp. 1363 – 1366, 2011. Transparent Conductive Materials (TCM 2010).
- [16] C. Chen, X. Yi, J. Zhang, and B. Xiong, "Micromachined uncooled IR bolometer linear array using VO₂ thin films," *Int. J. Infrared Millimeter Waves*, vol. 22, no. 1, pp. 53–58, 2001.
- [17] M. D. Goldflam, M. K. Liu, B. C. Chapler, H. T. Stinson, A. J. Sternbach, A. S. McLeod, J. D. Zhang, K. Geng, M. Royal, B.-J. Kim, R. D. Averitt, N. M. Jokerst, D. R. Smith, H.-T. Kim, and D. N. Basov, "Voltage switching of a vo₂ memory metasurface using ionic gel," *Applied Physics Letters*, vol. 105, no. 4, p. 041117, 2014.
- [18] A. W. Smith, "Optical storage in vo₂ films," *Applied Physics Letters*, vol. 23, no. 8, pp. 437–438, 1973.
- [19] J. D. Ryckman, V. Diez-Blanco, J. Nag, R. E. Marvel, B. K. Choi, R. F. Haglund, and S. M. Weiss, "Photothermal optical modulation of ultra-compact hybrid si-vo₂ ring resonators," *Opt. Express*, vol. 20, pp. 13215–13225, Jun 2012.
- [20] G. Xu, Y. Chen, M. Tazawa, and P. Jin, "Surface plasmon resonance of silver nanoparticles on vanadium dioxide," *The Journal of Physical Chemistry B*, vol. 110, pp. 2051–2056, feb 2006.
- [21] C. Zener and R. H. Fowler, "A theory of the electrical breakdown of solid dielectrics," *Proceedings of the Royal Society of London. Series A, Containing Papers of a Mathematical and Physical Character*, 1934.
- [22] Y. T. Masatoshi Imada, Atsushi Fujimori, "Metal-insulator transitions," *Rev. Mod. Phys*, 1998.

- [23] N. M. K. Williams, *An introduction to Microelectromechanical systems Engineering*. Artech House, Inc., 2004.
- [24] M. W. Ashraf, S. Tayyaba, and N. Afzulpurkar, "Micro electromechanical systems (MEMS) based microfluidic devices for biomedical applications," *International Journal of Molecular Sciences*, vol. 12, pp. 3648–3704, jun 2011.
- [25] T. P. Burg, M. Godin, S. M. Knudsen, W. Shen, G. Carlson, J. S. Foster, K. Babcock, and S. R. Manalis, "Weighing of biomolecules, single cells and single nanoparticles in fluid," *Nature*, vol. 446, pp. 1066–1069, apr 2007.
- [26] M. Godin, F. F. Delgado, S. Son, W. H. Grover, A. K. Bryan, A. Tzur, P. Jorgensen, K. Payer, A. D. Grossman, M. W. Kirschner, and S. R. Manalis, "Using buoyant mass to measure the growth of single cells," *Nature Methods*, vol. 7, pp. 387–390, apr 2010.
- [27] W. H. Grover, A. K. Bryan, M. Diez-Silva, S. Suresh, J. M. Higgins, and S. R. Manalis, "Measuring single-cell density," *Proceedings of the National Academy of Sciences*, vol. 108, no. 27, pp. 10992–10996, 2011.
- [28] M. G. von Muhlen, N. D. Brault, S. M. Knudsen, S. Jiang, and S. R. Manalis, "Label-free biomarker sensing in undiluted serum with suspended microchannel resonators," *Analytical Chemistry*, vol. 82, no. 5, pp. 1905–1910, 2010. PMID: 20148583.
- [29] S. A. M. Bukhari, M. F. Khan, A. Goswami, R. McGee, and T. Thundat, "Thermomechanical analysis of picograms of polymers using a suspended microchannel cantilever," *RSC Advances*, vol. 7, no. 14, pp. 8415–8420, 2017.

- [30] M. Yun, I. Lee, S. Jeon, and J. Lee, "Facile phase transition measurements for nanogram level liquid samples using suspended microchannel resonators," *IEEE Sensors Journal*, vol. 14, pp. 781–785, mar 2014.
- [31] I. Lee, K. Park, and J. Lee, "Precision density and volume contraction measurements of ethanol–water binary mixtures using suspended microchannel resonators," *Sensors and Actuators A: Physical*, vol. 194, pp. 62–66, may 2013.
- [32] H. Park and K. Park, *Polymers of Biological and Biomedical Significance, Copyright, 1993 Advisory Board, Foreword*, ch. 1, pp. 2–15. American Chemical Society, 1993.
- [33] F. Hussain, M. Hojjati, M. Okamoto, and R. E. Gorga, "Review article: Polymer-matrix nanocomposites, processing, manufacturing, and application: An overview," *Journal of Composite Materials*, vol. 40, no. 17, pp. 1511–1575, 2006.
- [34] J. Qiao, M. Guo, L. Wang, D. Liu, X. Zhang, L. Yu, W. Song, and Y. Liu, "Recent advances in polyolefin technology," *Polymer Chemistry*, vol. 2, no. 8, p. 1611, 2011.
- [35] R. Brown, "Editorial," *Polymer Testing*, vol. 70, p. A1, sep 2018.
- [36] A. Akelah, in *Functionalized Polymeric Materials in Agriculture and the Food Industry*. Springer, US, Boston, 2013.
- [37] B. N. . A. M. J. Zhijun Hu, Mingwen Tian, "Regular arrays of highly ordered ferroelectric polymer nanostructures for non-volatile low-voltage memories," *Nature Materials*, 2008.
- [38] A. S. A. et al, "Nanostructured materials for advanced energy conversion and storage devices," *Nature Materials*, 2005.

- [39] N. G. S. M. N. B. Larsen, "Biomimetic polymer nanostructures by injection molding," *Macromol. Mater. Eng.*, 2003.
- [40] B. Wunderlich, *Thermal Analysis of Polymeric Materials*. Springer, 2005.
- [41] J. Heijboer, "Secondary loss peaks in glassy amorphous polymers," *International Journal of Polymeric Materials and Polymeric Biomaterials*, vol. 6, no. 1-2, pp. 11–37, 1977.
- [42] C. Schick, "Differential scanning calorimetry (dsc) of semicrystalline polymers," *Analytical and Bioanalytical Chemistry*, vol. 395, p. 1589, Oct 2009.
- [43] B. Wunderlich, "Thermal analysis of macromolecules," *Journal of thermal analysis*, vol. 46, pp. 643–679, Mar 1996.
- [44] D. V. Suriapparao, D. K. Ojha, T. Ray, and R. Vinu, "Kinetic analysis of co-pyrolysis of cellulose and polypropylene," *Journal of Thermal Analysis and Calorimetry*, vol. 117, pp. 1441–1451, Sep 2014.
- [45] K. P. Menard, *Dynamic Mechanical Analysis: A Practical Introduction*. CRC Press, Boca Raton, 1999.
- [46] Y. A. Olkhov and B. Jurkowski, "On the more informative version of thermomechanical analysis at compression mode," *Journal of Thermal Analysis and Calorimetry*, vol. 81, pp. 489–500, Jul 2005.
- [47] A. Schönhal, *Dielectric Spectroscopy on the Dynamics of Amorphous Polymeric Systems*. Novocontrol, 1998.
- [48] C. Yim, M. Yun, S. Kim, N. Jung, S.-H. Lim, M. Lee, S.-W. Rhee, T. Thundat, and S. Jeon, "Nanomechanical thermal analysis of indium films using silicon microcantilevers," *Japanese Journal of Applied Physics*, vol. 51, p. 08KB07, aug 2012.

- [49] S. Bose, S. Schmid, T. Larsen, S. S. Keller, P. Sommer-Larsen, A. Boisen, and K. Almdal, "Micromechanical string resonators: Analytical tool for thermal characterization of polymers," *ACS Macro Letters*, vol. 3, no. 1, pp. 55–58, 2014.
- [50] J. Fritz, "Cantilever biosensors," *Analyst*, vol. 133, pp. 855–863, 2008.
- [51] C. Rao, "Transition metal oxides¹," *Annu. Rev. Phys. Chem.*, vol. 40, no. 40, pp. 291–326, 1989.
- [52] Z. Shao, X. Cao, H. Luo, and P. Jin, "Recent progress in the phase-transition mechanism and modulation of vanadium dioxide materials," *NPG Asia Materials*, vol. 10, pp. 581–605, jul 2018.
- [53] M. Soltani, M. Chaker, E. Haddad, and R. Kruzelesky, "1 x2 optical switch devices based on semiconductor-to-metallic phase transition characteristics of VO₂ smart coatings," *Measurement Science and Technology*, vol. 17, pp. 1052–1056, apr 2006.
- [54] J. S. Lee, M. Ortolani, U. Schade, Y. J. Chang, and T. W. Noh, "Microspectroscopic detection of local conducting areas generated by electric-pulse-induced phase transition in VO₂ films," *Applied Physics Letters*, vol. 91, p. 133509, sep 2007.
- [55] E. Strelcov, Y. Lilach, and A. Kolmakov, "Gas sensor based on metal insulator transition in vo₂ nanowire thermistor," *Nano Letters*, vol. 9, no. 6, pp. 2322–2326, 2009. PMID: 19507888.
- [56] N. Jung and S. Jeon, "Nanomechanical thermal analysis with silicon cantilevers of the mechanical properties of poly(vinyl acetate) near the glass transition temperature," *Macromolecules*, vol. 41, no. 24, pp. 9819–9822, 2008.

- [57] M. Yun, N. Jung, C. Yim, and S. Jeon, "Nanomechanical thermal analysis of the effects of physical aging on glass transitions in ps/pmma blend and ps-pmma diblock copolymers," *Polymer*, vol. 52, no. 18, pp. 4136 – 4140, 2011.
- [58] S. Bose, S. S. Keller, T. S. Alstrøm, A. Boisen, and K. Almdal, "Process optimization of ultrasonic spray coating of polymer films," *Langmuir*, vol. 29, no. 23, pp. 6911–6919, 2013. PMID: 23631433.
- [59] J. Kim, J. Song, K. Kim, S. Kim, J. Song, N. Kim, M. F. Khan, L. Zhang, J. E. Sader, K. Park, D. Kim, T. Thundat, and J. Lee, "Hollow microtube resonators via silicon self-assembly toward subattogram mass sensing applications," *Nano Letters*, vol. 16, no. 3, pp. 1537–1545, 2016. PMID: 26816114.
- [60] M. Khan, S. Schmid, P. Larsen, Z. Davis, W. Yan, E. Stenby, and A. Boisen, "Online measurement of mass density and viscosity of pl fluid samples with suspended microchannel resonator," *Sensors and Actuators B: Chemical*, vol. 185, pp. 456 – 461, 2013.
- [61] M. Faheem Khan, S. Kim, D. Lee, S. Schmid, A. Boisen, and T. Thundat, "Nanomechanical identification of liquid reagents in a microfluidic channel," *Lab Chip*, vol. 14, pp. 1302–1307, 2014.
- [62] N. Miriyala, M. Khan, and T. Thundat, "Thermomechanical behavior of a bimaterial microchannel cantilever subjected to periodic ir radiation," *Sensors and Actuators B: Chemical*, vol. 235, pp. 273 – 279, 2016.
- [63] R. McGee, A. Goswami, B. Khorshidi, K. McGuire, K. Schofield, and T. Thundat, "Effect of process parameters on phase stability and metal-insulator transition of vanadium dioxide (vo₂) thin films by pulsed laser deposition," *Acta Materialia*, vol. 137, pp. 12 – 21, 2017.

- [64] R. McGee, A. Goswami, R. Abraham, S. Bukhari, and T. Thundat, "Phase transformation induced modulation of the resonance frequency of VO₂/tio₂ coated microcantilevers," *MRS Advances*, vol. 3, no. 6-7, pp. 359–364, 2018.
- [65] L. G. Villanueva, R. B. Karabalin, M. H. Matheny, D. Chi, J. E. Sader, and M. L. Roukes, "Nonlinearity in nanomechanical cantilevers," *Phys. Rev. B*, 2013.
- [66] T. J. Huffman, C. Hendriks, E. J. Walter, J. Yoon, H. Ju, R. Smith, G. L. Carr, H. Krakauer, and M. M. Qazilbash, "Insulating phases of vanadium dioxide are mott-hubbard insulators," *Physical Review B*, vol. 95, feb 2017.
- [67] R. M. Wentzcovitch, W. W. Schulz, and P. B. Allen, "Vo₂: Peierls or mott-hubbard? a view from band theory," *Phys. Rev. Lett.*, 1994.
- [68] B. Wu, A. Zimmers, H. Aubin, R. Ghosh, Y. Liu, and R. Lopez, "Electric-field-driven phase transition in vanadium dioxide," *Physical Review B*, vol. 84, dec 2011.
- [69] A. Pergament, P. Boriskov, A. Velichko, and N. Kuldin, "Switching effect and the metal–insulator transition in electric field," *Journal of Physics and Chemistry of Solids*, vol. 71, no. 6, pp. 874 – 879, 2010.
- [70] A. Pergament, "Metal–insulator transition: the mott criterion and coherence length," *Journal of Physics: Condensed Matter*, vol. 15, pp. 3217–3223, may 2003.
- [71] A. Pergament, A. Velichko, and G. Stefanovich, "Addendum to "switching effect and the metal–insulator transition in electric field" by a.l. pergament et al. [j. phys. chem. solids 71 (2010) 874]," *Journal of Physics and Chemistry of Solids*, vol. 77, pp. 137 – 138, 2015.

- [72] E. Sillero, O. A. Williams, V. Lebedev, V. Cimalla, C.-C. Röhlig, C. E. Nebel, and F. Calle, "Static and dynamic determination of the mechanical properties of nanocrystalline diamond micromachined structures," *Journal of Micromechanics and Microengineering*, vol. 19, p. 115016, oct 2009.
- [73] R. B. Karabalin, L. G. Villanueva, M. H. Matheny, J. E. Sader, and M. L. Roukes, "Stress-induced variations in the stiffness of micro- and nanocantilever beams," *PhysRevLett*.108.236101, 2012.
- [74] N. Sepúlveda, A. Rúa, R. Cabrera, and F. Fernández, "Young's modulus of VO₂ thin films as a function of temperature including insulator-to-metal transition regime," *Applied Physics Letters*, vol. 92, p. 191913, may 2008.
- [75] P. Related and content, "Journal of micromechanics and microengineering," 2019.
- [76] L. Nicu and C. Bergaud, "Experimental and theoretical investigations on nonlinear resonances of composite buckled microbridges," *Journal of Applied Physics*, vol. 86, pp. 5835–5840, nov 1999.
- [77] Mechanical, thermal effects of laser irradiation, and on force microscope cantilevers, "Ultramicroscopy 42-44 (1992) 345-350 y north-holland," 1992.
- [78] R. J. . D. L. Naikun Gao, Dongfang Zhao, "Microcantilever actuation by laser induced photoacoustic waves," *Scientific Reports*, 2016.
- [79] J. Z. Jiang, H. Lindelov, L. Gerward, K. Ståhl, J. M. Recio, P. Morisánchez, S. Carlson, M. Mezouar, E. Dooryhee, A. Fitch, and D. J. Frost, "Compressibility and thermal expansion of cubic silicon nitride," *Physical Review B*, vol. 65, apr 2002.

- [80] M. Khan, S. Schmid, Z. Davis, S. Dohn, and A. Boisen, "Fabrication of resonant micro cantilevers with integrated transparent fluidic channel," *Microelectronic Engineering*, vol. 88, pp. 2300–2303, aug 2011.
- [81] D. Dijkkamp, T. Venkatesan, X. D. Wu, S. A. Shaheen, N. Jisrawi, Y. H. Min-Lee, W. L. McLean, and M. Croft, "Preparation of Y-Ba-Cu oxide superconductor thin films using pulsed laser evaporation from high T_c bulk material," *Appl. Phys. Lett.*, vol. 51, no. 8, pp. 619–621, 1987.
- [82] D. P. Norton, "Pulsed laser deposition of complex materials: Progress toward applications," in *Wiley* (R. Eason, ed.), ch. 1, pp. 3–28, John Wiley & Sons, 2007.
- [83] M. Rahe, "Bücher: Excimer laser technology. by d. basting, g. marowsky," *Laser Technik Journal*, vol. 3, no. 3, pp. 56–56, 2006.
- [84] J. A. Venables, T. Spiller, and M. Hanbucken, "Reports on Progress in Physics Nucleation and growth of thin films," *Rep. Prog. Phys.*, vol. 47, no. 47, pp. 399–399, 1984.
- [85] 1964.
- [86] B. P. Payne, *X-ray Photoelectron Spectroscopy Studies on the Oxidation Processes of Nickel, Chromium and their Alloys*. PhD thesis, The University of Western Ontario, 2011.
- [87] G. Haler, "Polymers for microelectronics," in *Materials today*, 2001.
- [88] J.-P. McGovern, W. Y. Shih, R. Rest, M. Purohit, Y. Pandya, and W.-H. Shih, "Label-free flow-enhanced specific detection of bacillus anthracis using a piezoelectric microcantilever sensor," *The Analyst*, vol. 133, no. 5, p. 649, 2008.
- [89] S. Aldrich, "<https://www.sigmaaldrich.com/catalog>."

- [90] S. Timoshenko, D. H. Young, and W. Weaver Jr., *Vibration Problems in Engineering*. John Wiley & Sons, Inc., fourth ed., 1974.
- [91] D. Liu and C. Zhong, "Modeling of the heat and capacity of polymers and with the variable and connectivity index," in *Polymer Journal*, Vol. 34, No. 12, pp 954—961 (2002), 2002.
- [92] T. Hayashi and K. Fukao, "Segmental and local dynamics of stacked thin films of poly(methyl methacrylate)," *Physical Review E*, vol. 89, feb 2014.
- [93] A. Goswami, A. M. Umarji, and G. Madras, "Thermomechanical and fractographic behavior of poly (HDDA-co-MMA): a study for its application in microcantilever sensors," *Polymers for Advanced Technologies*, vol. 23, pp. 1604–1611, mar 2012.
- [94] M. S. Ardi, W. Dick, and J. Kubát, "Time-domain dielectric relaxation of poly(methyl methacrylate) and nitrile rubber," *Colloid and Polymer Science*, vol. 271, pp. 739–747, Aug 1993.
- [95] G. Andersson, C. Parck, U. Ulfvarson, E. Stenhagen, and B. Thorell, "Studies on Vanadium Oxides. II. The Crystal Structure of Vanadium Dioxide.," *Acta Chem. Scand.*, vol. 10, pp. 623–628, 1956.
- [96] F. J. Morin, "Oxides which show a metal-to-insulator transition at the neel temperature," *Phys. Rev. Lett.*, vol. 3, no. 1, pp. 34–36, 1959.
- [97] N. F. Mott and L. Friedman, "Metal-insulator transitions in VO_2 , Ti_2O_3 and $\text{Ti}_{2-x}\text{V}_x\text{O}_3$," *Philos. Mag.*, vol. 30, no. 2, pp. 389–402, 1974.
- [98] H. W. Verleur, A. S. Barker, and C. N. Berglund, "Optical properties of VO_2 between 0.25 and 5 eV," *Rev. Mod. Phys.*, vol. 40, no. 4, p. 737, 1968.

- [99] B. Wang, J. Lai, H. Li, H. Hu, and S. Chen, "Nanostructured vanadium oxide thin film with high TCR at room temperature for microbolometer," *Infrared Phys. Technol.*, vol. 57, pp. 8–13, 2013.
- [100] H. Jerominek, T. D. Pope, M. Renaud, N. R. Swart, F. Picard, M. Lehoux, S. Savard, G. Bilodeau, D. Audet, P. Linh Ngo, and Q. Chu Nong, "6464, 128128, 240320 pixel uncooled IR bolometric detector arrays," in *Infrared Technology and Applications XXIII, 20-25 April 1997*, 1997.
- [101] R. T. Rajendra, B. Karunagaran, and D. Mangalaraj, "Study of a pulsed laser deposited vanadium oxide based microbolometer," *Smart Mater. Struct.*, vol. 188, pp. 187–192, 2003.
- [102] L. Pellegrino, N. Manca, T. Kanki, H. Tanaka, M. Biasotti, E. Bellingeri, A. S. Siri, and D. Marré, "Multistate memory devices based on free-standing VO₂/TiO₂ microstructures driven by Joule self-heating," *Adv. Mater.*, 2012.
- [103] L. Fan, Y. Chen, Q. Liu, S. Chen, L. Zhu, Q. Meng, B. Wang, Q. Zhang, H. Ren, and C. Zou, "Infrared Response and Optoelectronic Memory Device Fabrication Based on Epitaxial VO₂ Film," *ACS Appl. Mater. Interfaces*, 2016.
- [104] G. Stefanovich, a. Pergament, and D. Stefanovich, "Electrical switching and Mott transition in VO₂," *J. Phys.: Condens. Matter*, vol. 12, no. 41, pp. 8837–8845, 2000.
- [105] M. Rini, Z. Hao, R. W. Schoenlein, C. Giannetti, F. Parmigiani, S. Fourmaux, J. C. Kieffer, A. Fujimori, M. Onoda, S. Wall, and A. Cavalleri, "Optical switching in VO₂ films by below-gap excitation," *Appl. Phys. Lett.*, vol. 92, no. 18, pp. 1–4, 2008.
- [106] A. Gupta, R. Aggarwal, and J. Narayan, "Integration of VO₂ Thin Films

- on Si (100) for Thermal Switching Devices Applications," *Mater. Res. Soc. Symp. Proc.*, vol. 1174, 2009.
- [107] J. Zhou, Y. Gao, Z. Zhang, H. Luo, C. Cao, Z. Chen, L. Dai, and X. Liu, "VO₂ thermochromic smart window for energy savings and generation.," *Sci. Rep.*, vol. 3, p. 3029, 2013.
- [108] Y. Ke, I. Balin, N. Wang, Q. Lu, A. Iing, Y. Tok, T. J. White, S. Magdassi, I. Abdulhalim, and Y. Long, "Two-Dimensional SiO₂/VO₂ Photonic Crystals with Statically Visible and Dynamically Infrared Modulated for Smart Window Deployment," *ACS Appl. Mater. Interfaces*, 2016.
- [109] J. Zhu, Y. Zhou, B. Wang, J. Zheng, S. Ji, H. Yao, H. Luo, and P. Jin, "Vanadium Dioxide Nanoparticle-based Thermochromic Smart Coating: High Luminous Transmittance, Excellent Solar Regulation Efficiency, and Near Room Temperature Phase Transition," *ACS Appl. Mater. Interfaces*, 2015.
- [110] S.-H. Bae, S. Lee, H. Koo, L. Lin, B. Hyun Jo, C. Park, Z. Lin Wang, S.-h. Bae, H. Koo, B. H. Jo C Park, S. Lee, L. Lin, Z. L. Wang, and C. Park, "The Memristive Properties of a Single VO₂ Nanowire with Switching Controlled by Self-Heating," *Adv. Mater.*, 2013.
- [111] B. Hu, Y. Ding, W. Chen, D. Kulkarni, Y. Shen, V. V. Tsukruk, and Z. L. Wang, "External-strain induced insulating phase transition in VO₂ nanobeam and its application as flexible strain sensor," *Adv. Mater.*, vol. 22, no. 45, pp. 5134–5139, 2010.
- [112] K. Kosuge, "The phase diagram and phase transition of the V₂O₅-VO₂ system," *J. Phys. Chem. Solids Pergamon Press*, vol. 28, pp. 1613–1621, 1967.

- [113] M. J. Miller and J. Wang, "Influence of grain size on transition temperature of thermochromic VO₂," *J. Appl. Phys.*, vol. 117, no. 96, 2015.
- [114] Y. Zhao, J. H. Lee, Y. Zhu, M. Nazari, C. Chen, H. Wang, A. Bernussi, M. Holtz, and Z. Fan, "Structural, electrical, and terahertz transmission properties of VO₂ thin films grown on c-, r-, and m-plane sapphire substrates," *J. Appl. Phys.*, vol. 1111, no. 10, 2012.
- [115] R. E. Marvel, R. R. Harl, V. Craciun, B. R. Rogers, and R. F. Haglund, "Influence of deposition process and substrate on the phase transition of vanadium dioxide thin films," *Acta Mater.*, vol. 91, pp. 217–226, 2015.
- [116] L. L. Fan, S. Chen, Z. L. Luo, Q. H. Liu, Y. F. Wu, L. Song, D. X. Ji, P. Wang, W. S. Chu, C. Gao, C. W. Zou, and Z. Y. Wu, "Strain Dynamics of Ultrathin VO₂ Film Grown on TiO₂ (001) and the Associated Phase Transition Modulation," *Nano Lett.*, vol. 14, no. 7, pp. 4036–4043, 2014.
- [117] L. L. Fan, S. Chen, G. M. Liao, Y. L. Chen, H. Ren, and C. W. Zou, "Comprehensive studies of interfacial strain and oxygen vacancy on metal–insulator transition of VO₂ film," *J. Phys.: Condens. Matter*, vol. 28, no. 25, p. 255002, 2016.
- [118] T. Yamin, S. Wissberg, H. Cohen, G. Cohen-Taguri, and A. Sharoni, "Ultrathin Films of VO₂ on r-Cut Sapphire Achieved by Postdeposition Etching," *ACS Appl. Mater. Interfaces*, 2016.
- [119] Y. Li, S. Ji, Y. Gao, H. Luo, and P. Jin, "Modification of Mott Phase Transition Characteristics in VO₂@TiO₂ Core/Shell Nanostructures by Misfit-Strained Heteroepitaxy," *ACS Appl. Mater. Interfaces*, 2013.
- [120] J. Nag, E. A. Payzant, K. L. More, and R. F. Haglund, "Enhanced performance of room-temperature-grown epitaxial thin films of vanadium dioxide," *Appl. Phys. Lett.*, vol. 98, no. 25, pp. 1–4, 2011.

- [121] R. McGee, A. Goswami, S. Pal, K. Schofield, S. A. M. Bukhari, and T. Thundat, "Sharpness and intensity modulation of the metal-insulator transition in ultrathin VO₂ films by interfacial structure manipulation," *Physical Review Materials*, vol. 2, mar 2018.
- [122] T. D. Vu, Z. Chen, X. Zeng, M. Jiang, S. Liu, Y. Gao, and Y. Long, "Physical vapour deposition of vanadium dioxide for thermochromic smart window applications," *J. Mater. Chem. C*, vol. 7, pp. 2121–2145, 2019.
- [123] R. Jaramillo and S. Ramanathan, "Electronic granularity and the work function of transparent conducting ZnO:al thin films," *Advanced Functional Materials*, vol. 21, pp. 4068–4072, aug 2011.
- [124] W. Lu, L.-M. Wong, S. Wang, and K. Zeng, "Local phenomena at grain boundaries: An alternative approach to grasp the role of oxygen vacancies in metallization of VO₂," *Journal of Materiomics*, vol. 4, pp. 360–367, dec 2018.
- [125] W. Melitz, J. Shen, A. C. Kummel, and S. Lee, "Kelvin probe force microscopy and its application," *Surface Science Reports*, vol. 66, no. 1, pp. 1 – 27, 2011.
- [126] R. Hill, J. A. Notte, and L. Scipioni, "Chapter 2 - scanning helium ion microscopy," in *Advances in Imaging and Electron Physics* (P. W. Hawkes, ed.), vol. 170 of *Advances in Imaging and Electron Physics*, pp. 65 – 148, Elsevier, 2012.
- [127] M. van Veenendaal, "Ultrafast photoinduced insulator-to-metal transitions in vanadium dioxide," *Physical Review B*, vol. 87, jun 2013.
- [128] B.-G. Chae, H.-T. Kim, D.-H. Youn, and K.-Y. Kang, "Abrupt metal-insulator transition observed in vo₂ thin films induced by a

switching voltage pulse," *Physica B: Condensed Matter*, vol. 369, no. 1, pp. 76 – 80, 2005.

- [129] M. F. Becker, A. B. Buckman, R. M. Walser, T. Lépine, P. Georges, and A. Brun, "Femtosecond laser excitation of the semiconductor-metal phase transition in VO_2 ," *Applied Physics Letters*, vol. 65, no. 12, pp. 1507–1509, 1994.
- [130] A. Cavalleri, T. Dekorsy, H. H. W. Chong, J. C. Kieffer, and R. W. Schoenlein, "Evidence for a structurally-driven insulator-to-metal transition in VO_2 : A view from the ultrafast timescale," *Physical Review B*, vol. 70, oct 2004.
- [131] A. Cavalleri, M. Rini, H. H. W. Chong, S. Fourmaux, T. E. Glover, P. A. Heimann, J. C. Kieffer, and R. W. Schoenlein, "Band-selective measurements of electron dynamics in VO_2 using femtosecond near-edge x-ray absorption," *Physical Review Letters*, vol. 95, aug 2005.
- [132] A. Rúa, F. E. Fernández, M. A. Hines, and N. Sepúlveda, "Study of the resonant frequencies of silicon microcantilevers coated with vanadium dioxide films during the insulator-to-metal transition," *Journal of Applied Physics*, vol. 107, no. 5, p. 053528, 2010.
- [133] R. Cabrera, E. Merced, N. Sepúlveda, and F. E. Fernández, "Dynamics of photothermally driven VO_2 -coated microcantilevers," *Journal of Applied Physics*, vol. 110, no. 9, p. 094510, 2011.
- [134] R. Cabrera, E. Merced, and N. Sepulveda, "Performance of electrothermally driven VO_2 -based MEMS actuators," *Journal of Microelectromechanical Systems*, vol. 23, pp. 243–251, feb 2014.
- [135] E. Merced, R. Cabrera, N. Dávila, F. E. Fernández, and N. Sepúlveda, "A

- micro-mechanical resonator with programmable frequency capability," *Smart Materials and Structures*, vol. 21, p. 035007, feb 2012.
- [136] Y. Hu, Z. Li, T. Lan, and W. Chen, "Photoactuators for direct optical-to-mechanical energy conversion: From nanocomponent assembly to macroscopic deformation," *Advanced Materials*, vol. 28, no. 47, pp. 10548–10556, 2016.
- [137] G. Stefanovich, A. Pergament, and D. Stefanovich, "Electrical switching and mott transition in VO₂," *Journal of Physics: Condensed Matter*, vol. 12, pp. 8837–8845, sep 2000.
- [138] G. Hamaoui, N. Horny, C. L. Gomez-Heredia, J. A. Ramirez-Rincon, J. Ordonez-Miranda, C. Champeaux, F. Dumas-Bouchiat, J. J. Alvarado-Gil, Y. Ezzahri, K. Joulain, and M. Chirtoc, "Thermophysical characterisation of VO₂ thin films hysteresis and its application in thermal rectification," *Scientific Reports*, vol. 9, jun 2019.
- [139] C. Chen, X. Yi, X. Zhao, and B. Xiong, "Characterizations of vo₂-based uncooled microbolometer linear array," *Sensors and Actuators A: Physical*, vol. 90, no. 3, pp. 212 – 214, 2001.
- [140] T. Larsen, S. Schmid, and A. Boisen, "Micro string resonators as temperature sensors," *AIP Conference Proceedings*, vol. 1552, no. 1, pp. 931–936, 2013.
- [141] N. Manca, L. Pellegrino, T. Kanki, W. Venstra, G. Mattoni, Y. Higuchi, H. Tanaka, A. Caviglia, and D. Marré, "VO₂: A phase change material for micromechanics," *Proceedings*, vol. 1, p. 294, aug 2017.
- [142] Z. Liang, L. Zhao, W. Meng, C. Zhong, S. Wei, B. Dong, Z. Xu, L. Wan, and S. Wang, "Tungsten-doped vanadium dioxide thin films as smart

- windows with self-cleaning and energy-saving functions," *Journal of Alloys and Compounds*, vol. 694, pp. 124 – 131, 2017.
- [143] J. Liang, L. Hou, and J. Li, "Frequency tunable perfect absorber in visible and near-infrared regimes based on VO_2 phase transition using planar layered thin films," *J. Opt. Soc. Am. B*, vol. 33, pp. 1075–1080, Jun 2016.
- [144] M. D. LaHaye, O. Buu, B. Camarota, and K. C. Schwab, "Approaching the quantum limit of a nanomechanical resonator," *Science*, vol. 304, no. 5667, pp. 74–77, 2004.
- [145] S. Kolkowitz, A. C. Bleszynski Jayich, Q. P. Unterreithmeier, S. D. Bennett, P. Rabl, J. G. E. Harris, and M. D. Lukin, "Coherent sensing of a mechanical resonator with a single-spin qubit," *Science*, vol. 335, no. 6076, pp. 1603–1606, 2012.
- [146] L. Li, "Recent development of micromachined biosensors," *IEEE Sensors Journal*, vol. 11, pp. 305–311, feb 2011.
- [147] H. G. Craighead, "Nanoelectromechanical systems," *Science*, vol. 290, no. 5496, pp. 1532–1535, 2000.
- [148] K. S. Hwang, S.-M. Lee, S. K. Kim, J. H. Lee, and T. S. Kim, "Micro- and nanocantilever devices and systems for biomolecule detection," *Annual Review of Analytical Chemistry*, vol. 2, no. 1, pp. 77–98, 2009. PMID: 20636054.
- [149] G. D. Cole, I. Wilson-Rae, K. Werbach, M. R. Vanner, and M. Aspelmeyer, "Phonon-tunnelling dissipation in mechanical resonators," *Nature Communications*, vol. 2, mar 2011.
- [150] J.-J. Li and K.-D. Zhu, "All-optical mass sensing with coupled mechanical resonator systems," *Physics Reports*, vol. 525, no. 3, pp. 223 – 254,

2013. All-optical Mass Sensing with Coupled Mechanical Resonator Systems.

- [151] J. Chaste, A. Eichler, J. Moser, G. Ceballos, R. Rurali, and A. Bachtold, "A nanomechanical mass sensor with yoctogram resolution," *Nature Nanotechnology*, 2012.
- [152] T. Remtema and L. Lin, "Active frequency tuning for micro resonators by localized thermal stressing effects," *Sensors and Actuators A: Physical*, vol. 91, no. 3, pp. 326 – 332, 2001. Proceedings of the Technical Digest of the 2000 Solid-State Sensors and Actuators Workshop.
- [153] I. Kozinsky, H. W. C. Postma, I. Bargatin, and M. L. Roukes, "Tuning nonlinearity, dynamic range, and frequency of nanomechanical resonators," *Applied Physics Letters*, vol. 88, no. 25, p. 253101, 2006.
- [154] S. C. Jun, X. M. H. Huang, M. Manolidis, C. A. Zorman, M. Mehregany, and J. Hone, "Electrothermal tuning of al-SiC nanomechanical resonators," *Nanotechnology*, vol. 17, pp. 1506–1511, feb 2006.
- [155] R. He, X. L. Feng, M. L. Roukes, and P. Yang, "Self-transducing silicon nanowire electromechanical systems at room temperature," *Nano Letters*, vol. 8, no. 6, pp. 1756–1761, 2008. PMID: 18481896.
- [156] E. Caruthers and L. Kleinman, "Energy Bands of Semiconducting VO₂," *Phys. Rev. B*, vol. 7, no. 8, pp. 3760–3766, 1973.
- [157] J. M. Wu and W. E. Chang, "Ultrahigh Responsivity and External Quantum Efficiency of an Ultraviolet-Light Photodetector Based on a Single VO₂ Microwire," *ACS Appl. Mater. Interfaces*, 2014.
- [158] X. Chen and S. S. Mao, "Titanium dioxide nanomaterials: synthesis, properties, modifications, and applications," *Chem. Rev.*, vol. 107, no. 7, pp. 2891–959, 2007.

- [159] Y. Cao, D. Torres, T. Wang, X. Tan, and N. Sepúlveda, "Enabling tunable micromechanical bandpass filters through phase-change materials," *Smart Materials and Structures*, vol. 26, p. 085032, jul 2017.
- [160] S. Wang, L. Kang, and D. H. Werner, "Hybrid resonators and highly tunable terahertz metamaterials enabled by vanadium dioxide (VO₂)," *Scientific Reports*, vol. 7, jun 2017.
- [161] N. Sepulveda, A. Rua, and F. E. Fernandez, "Resonant frequency behavior of silicon cantilevers coated with nanostructured and microcrystalline VO₂ films," *IEEE Transactions on Nanotechnology*, vol. 9, pp. 330–334, may 2010.
- [162] S. Rathi, J.-H. Park, I. yeal Lee, J. M. Baik, K. S. Yi, and G.-H. Kim, "Unravelling the switching mechanisms in electric field induced insulator–metal transitions in VO₂nanobeams," *Journal of Physics D: Applied Physics*, vol. 47, p. 295101, jun 2014.
- [163] R. McGee, A. Goswami, S. A. M. Bukhari, L. Zhou, K. Shankar, and T. Thundat, "Fabrication of phase change microstring resonators via top down lithographic techniques: Incorporation of vo₂/tio₂ into conventional processes," *IEEE JMEMS*, 2019.
- [164] D. H. Kim, E. J. Lee, M. R. Cho, C. S. Kim, Y. D. Park, and T. Kouh, "Photothermal effect and heat dissipation in a micromechanical resonator," *Applied Physics Express*, vol. 5, p. 075201, jun 2012.
- [165] W.-M. Zhang, K.-M. Hu, Z.-K. Peng, and G. Meng, "Tunable micro- and nanomechanical resonators," *Sensors (Basel, Switzerland)*, vol. 15, pp. 26478–26566, Oct. 2015.
- [166] T.-C. Chang, X. Cao, S.-H. Bao, S.-D. Ji, H.-J. Luo, and P. Jin, "Review on thermochromic vanadium dioxide based smart coatings: from lab

to commercial application," *Advances in Manufacturing*, vol. 6, pp. 1–19, Mar 2018.

- [167] A. Rúa, R. Cabrera, H. Coy, E. Merced, N. Sepúlveda, and F. E. Fernández, "Phase transition behavior in microcantilevers coated with M₁-phase VO₂ and M₂-phase VO₂:Cr thin films," *J. Appl. Phys.*, vol. 111, no. 10, p. 104502, 2012.
- [168] T. Wang, D. Torres, F. E. Fernández, C. Wang, and N. Sepúlveda, "Maximizing the performance of photothermal actuators by combining smart materials with supplementary advantages," *Science Advances*, vol. 3, no. 4, 2017.
- [169] K. Appavoo, B. Wang, N. F. Brady, M. Seo, J. Nag, R. P. Prasankumar, D. J. Hilton, S. T. Pantelides, and R. F. Haglund, "Ultrafast phase transition via catastrophic phonon collapse driven by plasmonic hot-electron injection," *Nano Lett.*, vol. 14, pp. 1127–1133, Mar. 2014.
- [170] A. Joushaghani, J. Jeong, S. Paradis, D. Alain, J. Stewart Aitchison, and J. K. S. Poon, "Voltage-controlled switching and thermal effects in vo₂ nano-gap junctions," *Applied Physics Letters*, vol. 104, no. 22, p. 221904, 2014.
- [171] E. Mastropaolo, G. S. Wood, I. Gual, P. Parmiter, and R. Cheung, "Electrothermally actuated silicon carbide tunable mems resonators," *Journal of Microelectromechanical Systems*, vol. 21, no. 4, pp. 811–821, 2012.
- [172] L. Jiang, R. Cheung, J. Hedley, M. Hassan, A. Harris, J. Burdess, M. Mehregany, and C. Zorman, "Sic cantilever resonators with electrothermal actuation," *Sensors and Actuators A: Physical*, vol. 128, no. 2, pp. 376 – 386, 2006.
- [173] R. R. A. Syms, "Electrothermal frequency tuning of folded and coupled

vibrating micromechanical resonators," *Journal of Microelectromechanical Systems*, vol. 7, no. 2, pp. 164–171, 1998.

- [174] S. Lee, K. Hippalgaonkar, F. Yang, J. Hong, C. Ko, J. Suh, K. Liu, K. Wang, J. J. Urban, X. Zhang, C. Dames, S. A. Hartnoll, O. Delaire, and J. Wu, "Anomalously low electronic thermal conductivity in metallic vanadium dioxide," *Science*, vol. 355, no. 6323, pp. 371–374, 2017.